ELECTRO-OPTICALLY TUNABLE MICRORING RESONATORS FOR NON-LINEAR FREQUENCY MODULATED WAVEFORM GENERATION

A Dissertation

by

WILLIAM TIMOTHY SNIDER

Submitted to the Office of Graduate Studies of
Texas A&M University
in partial fulfillment of the requirements for the degree of

DOCTOR OF PHILOSOPHY

August 2012

Major Subject: Electrical Engineering

ELECTRO-OPTICALLY TUNABLE MICRORING RESONATORS FOR NON-LINEAR FREQUENCY MODULATED WAVEFORM GENERATION

A Dissertation

by

WILLIAM TIMOTHY SNIDER

Submitted to the Office of Graduate Studies of
Texas A&M University
in partial fulfillment of the requirements for the degree of

DOCTOR OF PHILOSOPHY

Approved by:

Chair of Committee,	Christi K. Madsen
Committee Members,	Ohannes Eknoyan
	Henry Pfister
	Shaima Nasiri
Head of Department,	Costas Georghiades

August 2012

Major Subject: Electrical Engineering

ABSTRACT

Electro-optically Tunable Microring Resonators for Non-Linear Frequency Modulated Waveform Generation. (August 2012)

William Timothy Snider, B.S., Texas A&M University

Chair of Advisory Committee: Dr. Christi K. Madsen

Microring resonators are a fundamental building block for integrated optical filters, and have both modulation and waveform generation applications. A hybrid chalcogenide (As_2S_3) on titanium diffused ($Ti:LiNbO_3$) waveguide platform has been developed to realize tunable microring resonators on a lithium niobate ($LiNbO_3$) substrate. The use of a $LiNbO_3$ substrate allows for electro-optic tuning, which is demonstrated for the first time on an As_2S_3 guided optical mode. While optical modes confined in diffused waveguides are commonly electro-optically tuned, the use of a rib waveguide external to the substrate poses new design challenges. Simulation work to determine the optimum electrode design was carried out, while also taking into account the limitations of working with a low melting temperature chalcogenide material.

The tuning of this hybrid As_2S_3 on $Ti:LiNbO_3$ device structure is demonstrated with fabricated Mach-Zehnder interferometers and ring resonators. Electro-optic tuning of the TM polarization utilizing the r_{13} $LiNbO_3$ tuning coefficient is shown, yielding results that show an improvement over previous tunable $LiNbO_3$ microring resonators.

Simulations are also carried out to show the waveform generating capabilities of this hybrid device platform.

DEDICATION

To my family.

ACKNOWLEDGEMENTS

I would like to thank my committee chair, Dr. Madsen, for introducing me to optics during my senior year and providing wonderful support throughout the course of this research. I would also like to thank my other committee members, Dr. Eknoyan, Dr. Pfister, and Dr. Nasiri for their guidance and feedback.

Thanks to the ISSE staff for keeping the fabrication lab running so that my work could proceed without too many difficulties; R. Atkins, J. Gardner, D. Spears, T. James, B. Isbell, and J. Phillips. Many thanks are also extended to my friends and research group members for their support.

A special thanks to Mr. Christopher Hollar who allowed me to play in the Hullabaloo Band through the course of my graduate study.

I would like to acknowledge use of the TAMU Materials Characterization Facility, namely the XPS and SEM instruments, and would like to thank to Dr. Bisrat for her training and guidance on the SEM.

I would also like to extend my gratitude to the Department of Homeland Security (DHS) and Oak Ridge Institute for Science and Education (ORISE), which gave me the fellowship under which I obtained this degree. The fellowship, along with the summer internship that was a part of the program, helped lay a great foundation for my professional career.

Finally, thanks to my mother, father, brother, and other relatives for their encouragement while I pursued this degree.

This research was performed under an appointment to the Department of Homeland Security (DHS) Scholarship and Fellowship Program, administered by the Oak Ridge Institute for Science and Education (ORISE) through an interagency agreement between the U.S. Department of Energy (DOE) and DHS. ORISE is managed by Oak Ridge Associated Universities (ORAU) under DOE contract number DE-AC05-06OR23100. All opinions expressed in this paper are the author's and do not necessarily reflect the policies and views of DHS, DOE, or ORAU/ORISE.

NOMENCLATURE

AC	Alternating current
ACPS	Asymmetric coplanar strip (electrodes)
Al	Aluminum
As_2S_3	Arsenic trisulfide
CPS	Coplanar strip (electrodes)
DC	Direct current
FSR	Free spectral range
$LiNbO_3$	Lithium niobate
MZI	Mach-Zehnder interferometer
OPD	Optical path length difference
OPL	Optical path length
OVA	Optical vector analyzer
RF	Radio frequency
SEM	Scanning electron microscopy
SiO_2	Silicon dioxide
Si_3N_4	Silicon nitride
Ti	Titanium
Ti:$LiNbO_3$	Titanium indiffused waveguide ($LiNbO_3$ substrate)
XPS	X-ray photoelectron spectroscopy

TABLE OF CONTENTS

CHAPTER Page

LIST OF FIGURES

FIGURE Page

FIGURE Page

FIGURE Page

LIST OF TABLES

CHAPTER I

INTRODUCTION

In today's technologically advanced society, we take for granted the optical systems that allow us to instantly access a wealth of information. The internet, once just the simple ARPANET connecting four universities together with copper cables having a data rate of 50 *kb/s*, now is an everyday part of our life due to the vast optical fiber network that connects every continent except Antarctica. With the invention of low loss optical fiber in the 1970s, soon followed by optical amplifiers, long distance optical communication was demonstrated with the first transatlantic optical cable in 1988 [1]. Wavelength division multiplexing, or using different wavelengths of light to transmit multiple channels of information over a single fiber, has further increased the transmission capacity of optical fiber. With transmission rates of 40 *Gb/s*, bandwidths on the order of *Tb/s* can be obtained on a single fiber [2]. The bandwidth potential of optical fiber is so large that a single pound of fiber can replace more than two tons of copper cable [3].

When it comes to external data storage, it was not that long ago that we were limited to 1.5 *MB* floppy disks. Moving from magnetic storage to optical storage saw CDs capable of holding 700 *MB* of information, and more recently Blue-ray disc that can hold over 50 *GB*. Computer hard disk drives are also making the transition from magnetic heads to solid-state disk drives.

This dissertation follows the style of *IEEE Journal of Lightwave Technology*.

As these two examples show, optical technology and the integrated circuit are helping push technology forward. These two fields have also been combined with integrated optics, or photonic integrated circuits. Just as with long distance optical communication, integrated optics research started in the telecommunications industry. With the invention of a semiconductor laser in 1962, it only followed that there was a possibility to guide and manipulate the optical beam. In addition to working with waveguides, the researchers also looked at adding electrodes to control the index of refraction. When researchers at Bell Laboratories invented the electro-optic modulator on lithium niobate ($LiNbO_3$) substrate [4], little did they know that they had developed the high speed modulator that has become a mainstay in optical fiber communication [5]. The $LiNbO_3$ modulator is still desired for its high speed performance, and there are a wide range of commercial devices available capable of 40 *GHz* modulation rates.

Integrated photonics is not limited to $LiNbO_3$ substrates. Another substrate of interest is silicon (Si), where the goal is to make devices that are CMOS compatible [6]. However, because there is not strong electro-optic tuning in Si, current injection and thermal tuning must be used which limits the modulation rates to approximately 16 *GHz*. In the push for faster systems capable of carrying more information, this modulation rate is an important design parameter.

Integrated systems also have the advantage of providing a reduction in system size, weight, and power. These design considerations are of great interest in military and aerospace applications. Integrated optics also provide more functionality than simple bulk components, allowing for multiple active and passive components to be located on

the same chip. Hence, just as optics has pushed technology forward, integrated photonics has the capability to continue the trend and realize the next generation of cutting edge devices.

A. Motivation

As previously mentioned, external $LiNbO_3$ optical modulators are key components for high bit rate optical communication systems [5]. They are desired for their broad spectrum response that covers both the C band (1530 – 1565 *nm*) and L band (1565 – 1625 *nm*), high modulation bandwidths of 40 *GHz*, low insertion losses, and low frequency chirp [7]. These commercially available modulators have an interferometer design based on titanium-indiffused ($Ti:LiNbO_3$) waveguides, with phase shifting occurring in the branches of the interferometer by electro-optic tuning. The industry leading drive voltage from Thorlabs modulators is 5.5 *V*, with the voltage length products for commercial devices on the order of 12 – 15 *V-cm*. For $LiNbO_3$ devices it is possible to get tuning voltages down in the 5 *V-cm* range [8], and devices with tuning voltages of 5.35 *V-cm* have been demonstrated but at the expense of a much lower tuning bandwidth [9].

Interferometers are only feed-forward devices, and more advanced functionality can be introduced with a feedback path. Ring resonators provide this feedback, and an optical modulator can be realized by putting the phase shifter in the ring path [10]. Since compact devices are desired, bending radii for ring resonators are desired to be on the order of micrometers. However, difficulties arise in using $LiNbO_3$ for microring

resonators since standard Ti:$LiNbO_3$ [11] and proton exchange [12],[13] waveguides do not support tight bend radii due to their limited mode confinement.

Silicon-based devices do not have these mode confinement concerns. Resonant cavities with 100 μm radii are commonly fabricated on silicon [14], with ultrasmall resonators having 5 – 10 μm radii possible [15]. The issue with silicon-based modulators arises in the ability to tune them. There is a weak electro-optic effect in silicon that has been demonstrated [16], but most of the fast modulators are based on free-carrier concentration [10] or thermal tuning [17]. Thermal tuning is slow, on the order of milliseconds, but is commonly used by research groups such as those in [15]. Using faster carrier-depletion, small tuning voltages of 3.3 V-cm at 10 *GHz* have been observed on tunable interferometers [18] with tuning voltages as low as 1.5 *V-cm* on devices operating at lower frequencies [10]. Maximum modulation rates have been demonstrated around 16 *GHz*, with limitations arising due to tunneling and thermoionic emissions [10]. While these tuning voltages are smaller than with $LiNbO_3$ devices, there is a significant sacrifice in modulation bandwidth.

For ring resonators, electro-optic tuning is heavily desired due to its bandwidth capabilities, and the integration of nonlinear properties would also be desired to introduce more advanced device functionality [19]. Lithium niobate is an established technology for 40 *GHz* modulation, but as mentioned standard waveguide fabrication techniques do not support the tight bend radii desired for compact microring resonators. Turning away from standard waveguide fabrication techniques, the first 100 μm radius microring resonator on $LiNbO_3$ was realized in 2007 [19]. Crystal-ion-slicing was

utilized to slice out a rib waveguide from $LiNbO_3$, which was then buried in a polymer material to increase mode confinement. This is a rather complicated process, and ion-slicing causes a 50% reduction in the electro-optic tuning strength. Sticking with standard Ti:$LiNbO_3$ waveguides, other groups have turned to substrate etching to make the diffused waveguide into a rib waveguide with a larger index contrast due to air cladding [20]. While not as complex as crystal-ion-slicing, there is still a substrate etching process that places a greater emphasis on subsequent later alignment. While these techniques increase the mode confinement, as seen in Table 1, their tuning voltages are significantly larger than what is capable with $LiNbO_3$ substrate.

Table 1. Electro-optically tunable $LiNbO_3$ devices.

Device Description	Year	V_π	$V_\pi L$	Comments	Reference
Thorlabs, 10 GHz $LiNbO_3$	2012	5 V	--	zero-chirp	current product
Thorlabs, 40 GHz $LiNbO_3$	2012	5.5 V	12 – 15 V-cm	industry leading drive voltage	current product
Ti:$LiNbO_3$ Interferometer, TM	2009	2.14 V	5.35 V-cm	tested at 1 kHz	[9]
Ti:$LiNbO_3$ Ring, TM	2007	453 V	35.8 V-cm	r_{33}	[20]
Ti:$LiNbO_3$ Ring, TE	2007	983 V	77.7 V-cm	r_{13}	[20]
Sliced $LiNbO_3$, TM	2007	908 V	50 V-cm	bonded $LiNbO_3$ thin film	[19]

Previous work in our research group has focused on the development of a hybrid As_2S_3 on Ti:$LiNbO_3$ device platform [21]. There are numerous advantages to taking this hybrid material approach, especially when it comes to microring resonators. The As_2S_3 chalcogenide glass has a large refractive index and non-linear properties. In terms of mode confinement, which is directly proportional to the refractive index difference between the waveguide and the substrate, as seen in Table 2 mode confinement is significantly increased when using As_2S_3 waveguides.

Table 2. Index difference for waveguides.

Waveguide Materials	Δn
Ti:$LiNbO_3$	0.003
APE	0.01
As_2S_3	0.2

With a hybrid material approach, through the use of a higher index chalcogenide rib waveguide (As_2S_3) there is not a need for substrate etching or crystal-ion-slicing in order to obtain a tight bend radii as in [20],[19]. Bending radii on the order of 400 μm are possible without large bending losses. While blanket films of chalcogenide glasses have been used on $LiNbO_3$ substrate previously [22], this hybrid device platform is the first use of As_2S_3 bent rib waveguides on $LiNbO_3$ substrate [23]. Another added benefit of this approach is that the non-linear properties of As_2S_3 have the potential to add additional device functionality. The ultimate goal of this hybrid device platform is to realize tunable filter structures that can be used both as a modulator and for complex

waveform generation. While interferometric modulators are designed to be low chirp, the chirp of the ring resonator can be taken advantage of to generate frequency modulated waveforms.

While the As_2S_3 rib waveguide alleviates the bending radii issue, it introduces a challenge to electro-optic tuning. Since titanium diffused and proton exchange waveguides are incorporated into the $LiNbO_3$ substrate, they can easily take advantage of the substrate electro-optic tuning properties. However, As_2S_3 does not exhibit electro-optic tuning properties, so there are extra challenges to tuning optical modes guided by a chalcogenide waveguide. This work looks into these challenges, ways to alleviate them, the tradeoffs involved, and finally demonstrates electro-optic tuning of an As_2S_3 guided optical mode.

B. Organization of Dissertation

This dissertation is on the continued development of a hybrid As_2S_3 on $Ti:LiNbO_3$ device platform, namely the development of electro-optic tuning capabilities. While the main focus of work was on the development of electrodes for tuning, extensive work was also performed on fabrication process development and materials characterization for the entire hybrid device structure.

Chapter I is the introduction, and covers the motivation for the research presented in this dissertation. Chapter II follows upon this, and gives the theoretical review for this hybrid device structure. The theory behind As_2S_3 on $Ti:LiNbO_3$ waveguides is given, along with electro-optic tuning theory. During the discussion of this theory, the

challenges of working with As_2S_3 rib waveguides are introduced as necessary. Waveform generation capabilities with a ring resonator are also introduced in this chapter.

Chapter III covers the fabrication process developments for this device structure. While this device platform has been worked on in our research group for several years, improvements were made in the fabrication process that had a direct impact on overall device performance. A new DC/RF magnetron sputtering system was obtained by our group, which after much work greatly improved our fabrication capability. Extensive SEM imaging was also utilized to further optimize our fabrication process.

Chapter IV covers the electro-optic tuning results obtained. Results are given for both interferometer and ring resonator devices. Electro-optic tuning results are presented for both the As_2S_3 path length and the coupling region between the $Ti:LiNbO_3$ and As_2S_3 waveguides.

Chapter V is the conclusion, and gives a summary of the results obtained. Areas to look at for improvements are also noted in this chapter, which also leads into future work on this hybrid device platform.

CHAPTER II

THEORETICAL REVIEW

This chapter covers the theory behind As_2S_3 on Ti:$LiNbO_3$ waveguide devices. Starting with the foundation of electromagnetics, Maxwell's equations, the wave equation is derived and applied to find waveguide solutions. After the basic waveguide device theory is introduced, the theory behind electro-optic tuning is explained. It is then shown how electro-optic tuning can be utilized to realize waveform generation.

A. Waveguide Theory and Scalar Wave Equation

Since light is an electromagnetic wave, it follows that Maxwell's equations will govern the behavior of the optical wave. Maxwell's equations can be expressed as two curl equations and two divergence equations [24]

$$\nabla \times \boldsymbol{E} = -\frac{\partial \boldsymbol{B}}{\partial t} \tag{1}$$

$$\nabla \times \boldsymbol{H} = \frac{\partial \boldsymbol{D}}{\partial t} + \boldsymbol{J} \tag{2}$$

$$\nabla \cdot \boldsymbol{D} = \rho_v \tag{3}$$

$$\nabla \cdot \boldsymbol{B} = 0 \tag{4}$$

where E is the electric field, D is the electric flux density, ε is the dielectric permittivity, H is the magnetic field, B is the magnetic flux density, μ is the magnetic permeability, J is the free current density, and ρ_v is the free charge density. Note that for a source free

medium, an assumption that is typically made is $\boldsymbol{J} = 0$ and $\rho_v = 0$. Before Maxwell's equations can be applied, the relationship between *D* and *E*, along with *H* and *B*, need to be understood. The relationships between these field quantities are given by the constitutive relations [25]

$$\boldsymbol{D} = \varepsilon_o \boldsymbol{E} + \boldsymbol{P} = \varepsilon_o \left[1 + \chi_e\right] \boldsymbol{E} \tag{5}$$

$$\boldsymbol{B} = \mu_o \boldsymbol{H} + \boldsymbol{M} = \mu_o \left[1 + \chi_m\right] \boldsymbol{H} \tag{6}$$

where *P* is the polarization field, *M* is the magnetization field, χ_e is the electric susceptibility, χ_m is the magnetic susceptibility, and ε_o and μ_o are the free-space vacuum quantities of the permittivity and permeability. If the assumption is made for linear and isotropic media with a weak field, then (5)-(6) can be reduced to

$$\boldsymbol{D} = \varepsilon \boldsymbol{E} \tag{7}$$

$$\boldsymbol{B} = \mu \boldsymbol{H} \ . \tag{8}$$

Note that in the case of isotropic media, both the permittivity and permeability are scalar values.

With this relationship in place, the wave equation can be derived from Maxwell's equations. Start by taking the curl of (1), i.e. Faraday's law:

$$\nabla \times \left(\nabla \times \boldsymbol{E}\right) = \nabla \times \left(-\frac{\partial \boldsymbol{B}}{\partial t}\right). \tag{9}$$

Next utilize the fact that the curl is a spatial variable derivative, allowing for the partial derivatives to be computed. Then by using the constitutive relations in (7)-(8) and Ampere's law in (2):

$$\begin{aligned}\nabla\times\left(\nabla\times\boldsymbol{E}\right) &= -\frac{\partial}{\partial t}\left(\nabla\times\boldsymbol{B}\right) = -\mu\frac{\partial}{\partial t}\left(\nabla\times\boldsymbol{H}\right)\\ &= -\mu\frac{\partial}{\partial t}\left(\frac{\partial\boldsymbol{D}}{dt}\right) = -\mu\frac{\partial}{\partial t}\left(\varepsilon\frac{\partial\boldsymbol{E}}{dt}\right)\\ &= -\mu\varepsilon\frac{\partial^2\boldsymbol{E}}{\partial t^2}\ .\end{aligned} \tag{10}$$

The materials involved in this work are non-magnetic dielectric media, so the permeability $\mu = \mu_o$. The dielectric permittivity on the other hand is material dependent, and is given by $\varepsilon = \varepsilon_o\varepsilon_r$ where ε_r is the relative permittivity of the material. In optics it is common to work with the refractive index of the material, which is related to the relative permittivity by $n = \sqrt{\varepsilon_r}$. Expressing (10) in terms of the refractive index and free-space permittivity and permeability gives

$$\nabla\times\left(\nabla\times\boldsymbol{E}\right) = -\mu_o\varepsilon_o n^2\frac{\partial^2\boldsymbol{E}}{\partial t^2} = -\frac{n^2}{c_o^2}\frac{\partial^2\boldsymbol{E}}{\partial t^2} \tag{11}$$

where $c_o = \dfrac{1}{\sqrt{\varepsilon_o\mu_o}}$ is the free-space vacuum speed of light given by

$$c_o = \frac{1}{\sqrt{\varepsilon_o\mu_o}} = 2.998\times10^8\ {}^{m}\!/_{\sec}\ . \tag{12}$$

Further manipulating (11) by taking advantage of vector identities and Gauss' law in (3)

$$\nabla\times\left(\nabla\times\boldsymbol{E}\right) = \nabla\left(\nabla\cdot\boldsymbol{E}\right) - \nabla^2\boldsymbol{E} = -\nabla^2\boldsymbol{E} = -\frac{n^2}{c_o^2}\frac{\partial^2\boldsymbol{E}}{\partial t^2} \tag{13}$$

the wave equation becomes

$$\nabla^2\boldsymbol{E} - \frac{n^2}{c_o^2}\frac{\partial^2\boldsymbol{E}}{\partial t^2} = 0\ . \tag{14}$$

Equation (14) is known as the Helmholtz equation. Following the same procedure as in (9)-(14), except starting with Ampere's law, the Helmholtz equation can also be derived in terms of H

$$\nabla^2 \boldsymbol{H} - \frac{n^2}{c_o^2}\frac{\partial^2 \boldsymbol{H}}{\partial t^2} = 0\,. \tag{15}$$

Returning focus to the electric field Helmholtz equation, consider a single frequency harmonic time variation for the electric field

$$\boldsymbol{E}(\boldsymbol{r},t) = \boldsymbol{E}(\boldsymbol{r})e^{jwt}\,. \tag{16}$$

Then it follows that (14) becomes

$$\frac{\partial^2 \boldsymbol{E}}{\partial t^2} = -\omega^2 \boldsymbol{E}\left(\boldsymbol{r}\right) \tag{17}$$

$$\nabla^2 \boldsymbol{E} + \frac{\omega^2 n^2}{c_o^2}\boldsymbol{E} = \nabla^2 \boldsymbol{E} + k_o^2 n^2 \boldsymbol{E} = 0 \tag{18}$$

where $k_o = \dfrac{w}{c_o} = \dfrac{2\pi}{\lambda}$. For propagation along an axis, with propagation constant β, we then have the scalar wave equation

$$\nabla^2 \boldsymbol{E} + \left(k_o{}^2 n^2 - \beta^2\right)\boldsymbol{E} = 0\,. \tag{19}$$

With the field components known, the time average power for any propagating wave is given by

$$P = \frac{1}{2}\mathrm{Re}\iint \boldsymbol{E}\times\boldsymbol{H}^*\cdot dS \tag{20}$$

where dS is in the direction of propagation.

B. Anisotropic Media

The assumption was made above for isotropic medium, where the permittivity is a scalar value. However, $LiNbO_3$ is not an isotropic material; rather it is an anisotropic material where the electric permittivity is given by a tensor ($LiNbO_3$ is still isotropic magnetically). This gives a 3 x 3 matrix for the dielectric permittivity

$$\boldsymbol{\varepsilon} = \begin{bmatrix} \varepsilon_{11} & \varepsilon_{12} & \varepsilon_{13} \\ \varepsilon_{21} & \varepsilon_{22} & \varepsilon_{23} \\ \varepsilon_{31} & \varepsilon_{32} & \varepsilon_{33} \end{bmatrix}. \tag{21}$$

To simplify analysis, a principle coordinate system can be used that matches the crystal principal axes, reducing all off-diagonal tensor elements to zero and giving

$$\boldsymbol{\varepsilon} = \begin{bmatrix} \varepsilon_{11} & 0 & 0 \\ 0 & \varepsilon_{22} & 0 \\ 0 & 0 & \varepsilon_{33} \end{bmatrix} \tag{22}$$

where ε_{11}, ε_{22}, and ε_{33} are now known as the principle permittivities. In terms of a principal crystal axis, we can regard these as ε_x, ε_y, and ε_z which will yield refractive indices n_x, n_y, and n_z where $n_i = \sqrt{\frac{\varepsilon_i}{\varepsilon_o}}$.

Consider the energy density of the propagating wave, given by

$$U_e = \frac{1}{2}\boldsymbol{D}\cdot\boldsymbol{E} \tag{23}$$

which in the isotropic case gives

$$U_e = \frac{1}{2}\varepsilon\boldsymbol{E}^2 = \frac{1}{2}\frac{\boldsymbol{D}^2}{\varepsilon}. \tag{24}$$

In the anisotropic case for a diagonalized system, combining (22) and (23) gives

$$U_e = \frac{1}{2}\left[\frac{D_x^2}{\varepsilon_{11}} + \frac{D_y^2}{\varepsilon_{22}} + \frac{D_z^2}{\varepsilon_{33}}\right] = \frac{1}{2}\left[\frac{X}{\varepsilon_{r11}} + \frac{Y}{\varepsilon_{r22}} + \frac{Z}{\varepsilon_{r33}}\right] \tag{25}$$

where $X = D_x \Big/ \sqrt{2\varepsilon_o U_e}$, $Y = D_y \Big/ \sqrt{2\varepsilon_o U_e}$, $Z = D_z \Big/ \sqrt{2\varepsilon_o U_e}$, and $\varepsilon_{rii} = \varepsilon_{ii} \Big/ \varepsilon_o$. The quantities X, Y, and Z are units measured along the three principle axes, giving an ellipse defined by

$$1 = \frac{X^2}{\varepsilon_{r11}} + \frac{Y^2}{\varepsilon_{r22}} + \frac{Z^2}{\varepsilon_{r33}} = \frac{X^2}{n_x^2} + \frac{Y^2}{n_y^2} + \frac{Z^2}{n_z^2} \tag{26}$$

which is also known as the index ellipsoid. The index ellipsoid can be seen in Fig. 1, and the shape of the ellipsoid depends on the material crystalline properties.

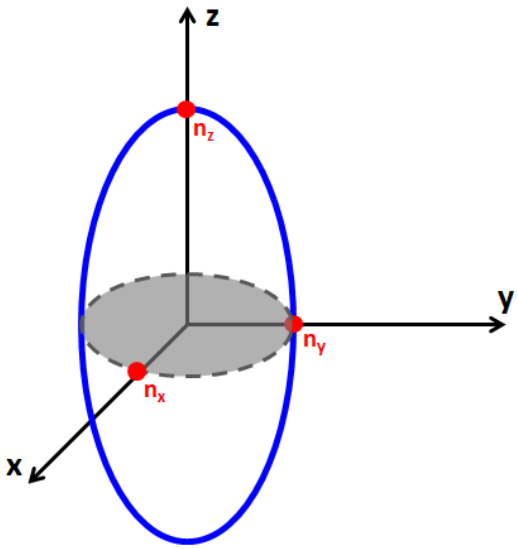

Fig. 1. Index ellipsoid.

Lithium niobate is a uniaxial material, meaning that there is symmetry about one axis, or the optical axis. As a result, for the refractive indices $n_x = n_y \neq n_z$. This means that there are two different values for the refractive indices, which are referred to as the ordinary refractive index, $n_o = n_x = n_y$, and the extraordinary refractive index, $n_e = n_z$. Due to this symmetry, the cross section of the index ellipsoid, as seen in Fig. 1, would be a circle. The ordinary and extraordinary refractive indices are wavelength dependent and are given by the Sellmeier equations

$$n_o = \sqrt{1 + \frac{2.6734\lambda^2}{\lambda^2 - 0.01764} + \frac{1.2290\lambda^2}{\lambda^2 - 0.05914} + \frac{12.614\lambda^2}{\lambda^2 - 474.60}} \tag{27}$$

$$n_e = \sqrt{1 + \frac{2.9804\lambda^2}{\lambda^2 - 0.02047} + \frac{0.5981\lambda^2}{\lambda^2 - 0.06660} + \frac{8.9543\lambda^2}{\lambda^2 - 416.08}} \tag{28}$$

where λ is the wavelength of light in μm and the substrate is at room temperature [26],[27]. For operation at 1531 nm, (27)-(28) give refractive indices of $n_o = 2.2118$ and $n_e = 2.1381$.

Since the refractive index is dependent on the crystal axis, $LiNbO_3$ wafers are typically diced along a principal axis. This gives x-cut, y-cut, and z-cut $LiNbO_3$ substrate, where the cut describes the principal axis that is normal to the substrate. Consider the case of x-cut $LiNbO_3$ shown below in Fig. 2. For an optical mode propagating along the y-axis, a TM polarized mode will experience $n_x = n_o$, and a TE polarized mode will experience $n_z = n_e$.

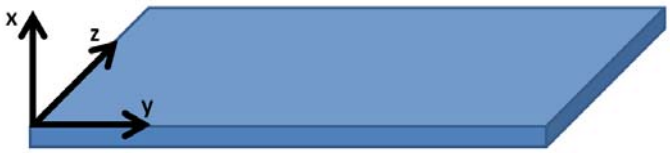

Fig. 2. Axes of x-cut $LiNbO_3$ substrate.

The equations for isotropic materials can still be used when dealing with anisotropic materials, but the anisotropic nature of the substrate must be taken into account when choosing the correct refractive index for the optical polarization.

C. Optical Waveguides

For a substrate to support the propagation of an optical mode, there must be a waveguiding region of higher refractive index. The simplest waveguide is a planar waveguide, as shown in Fig. 3.

Fig. 3. Planar optical waveguide structure.

For the planar waveguide there is no boundary on the y direction, so the field components are independent of y. In order to have a waveguide in region 1, it is required that $n_1 > n_3 \geq n_2$. For a plane wave propagating along the z-axis, the electromagnetic fields vary as

$$\boldsymbol{E} = E(x)e^{j(\omega t-\beta z)} \tag{29}$$

$$\boldsymbol{H} = H(x)e^{j(\omega t-\beta z)}. \tag{30}$$

The wave equation and Maxwell's equations give two different modes with orthogonal polarizations; the transverse electric (TE) mode and transverse magnetic (TM) mode. Solving (19), the TE mode has the wave equation

$$\frac{\partial^2 E_y}{\partial x^2} + \left(k_o^2 n^2 - \beta^2\right) E_y = 0 \tag{31}$$

with field components

$$H_x = -\frac{\beta}{\omega\mu_o} E_y \tag{32}$$

$$H_z = -\frac{1}{j\omega\mu_o}\frac{\partial E_y}{\partial x} \tag{33}$$

while the TM mode has the wave equation

$$\frac{\partial^2 H_y}{\partial x^2} + \left(k_o^2 n^2 - \beta^2\right) H_y = 0 \tag{34}$$

with field components

$$E_x = \frac{\beta}{\omega\varepsilon_o n^2} H_y \tag{35}$$

$$E_z = \frac{1}{j\omega\varepsilon_o n^2}\frac{\partial H_y}{\partial x}. \tag{36}$$

For a guided mode, there is a requirement on the propagation constant β that

$$k_o n_2 \le k_o n_3 < \beta < k_o n_1 . \tag{37}$$

which allows for quantities q, h, and p to be defined as

$$q = \sqrt{\beta^2 - k_o^2 n_2^2} \tag{38}$$

$$h = \sqrt{k_o^2 n_1^2 - \beta^2} \tag{39}$$

$$p = \sqrt{\beta^2 - k_o^2 n_3^2} \ . \tag{40}$$

For the TE mode, the electric field solutions for (31) in each region of Fig. 3 are of the form

$$E_y = \begin{cases} Ae^{-qx} & x > 0 \\ B\cos(hx) + C\sin(hx) & -t < x < 0 \\ De^{p(x+t)} & x < -t \ . \end{cases} \tag{41}$$

where A, B, C, and D are coefficients that can be found by applying the boundary condition that the field components be continuous. From this the characteristic equation, or eigenvalue equation for the TE mode is obtained

$$\tan(ht) = \frac{q+p}{h - \frac{qp}{h}} . \tag{42}$$

It follows that for the TM mode the eigenvalue equation is

$$\tan(ht) = \frac{\left(\frac{n_1}{n_3}\right)^2 p + \left(\frac{n_1}{n_2}\right)^2 q}{h - \left(\frac{n_1^2}{n_2 n_3}\right)^2 \frac{qp}{h}} . \tag{43}$$

The solution to the eigenvalue equation is easily seen graphically. Plotting both sides of the equation against h allows for the crossing points to be observed, as seen in Fig. 4.

For the parameters used in Fig. 4, this particular waveguide would support three optical modes, given by the three intersection points. With the *h* value of the intersection points known, the effective index n_{eff} of the optical mode can then be calculated from (39) since the propagation constant $\beta = k_o n_{eff}$.

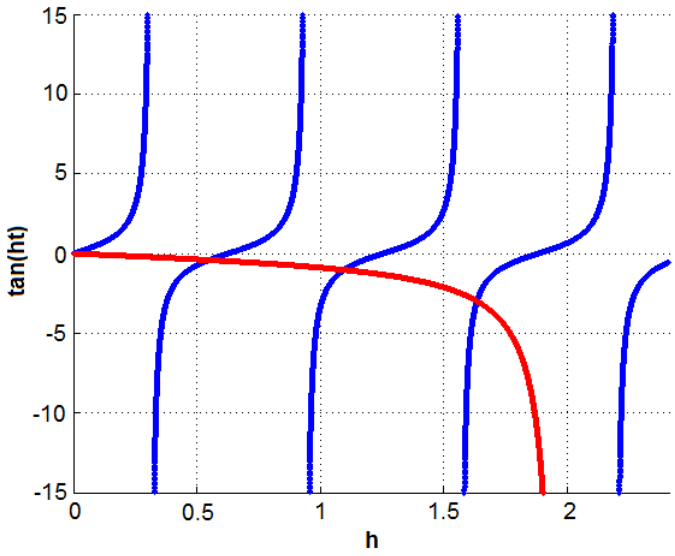

Fig. 4. Eigenvalue equation for TE mode plotted. Parameter values n_1=1.5, n_2=1.4, n_3=1.45, t=5 μm, and λ=1 μm.

C.1. Rectangular Waveguide

Recall that in the previous example there was only constraint on the waveguide in one dimension. Rectangular waveguides have mode confinement on all boundaries, as shown in Fig. 5. For calculations it is generally assumed that the propagation distance is infinite, giving a two dimensional waveguide structure to solve.

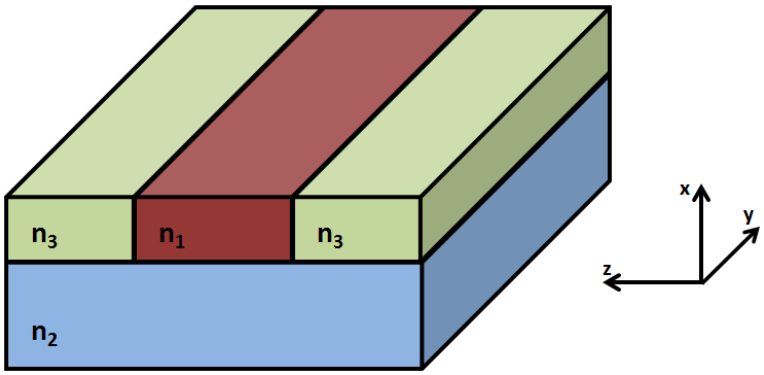

Fig. 5. Rectangular waveguide structure.

This waveguide structure reflects that of the As_2S_3 rib waveguides that are used on our devices. After etching the thin film, what remains is a rectangular/rib As_2S_3 waveguide on the $LiNbO_3$ surface. The As_2S_3 can either be left with an air cladding $(n_3 = 1)$, or in our case a protective cladding/buffer layer of SiO_2 $(n_3 \approx 1.5)$ is deposited.

There is still a step index profile since As_2S_3 is an isotropic media with a constant refractive index. Just as with $LiNbO_3$, there is a wavelength dependence to the refractive index of As_2S_3 given by a Sellmeier equation [28]

$$n = \sqrt{1 + \frac{1.8984\lambda^2}{\lambda^2 - 0.0225} + \frac{1.9223\lambda^2}{\lambda^2 - 0.0625} + \frac{0.8765\lambda^2}{\lambda^2 - 0.1225} + \frac{0.1189\lambda^2}{\lambda^2 - 0.2025} + \frac{0.9570\lambda^2}{\lambda^2 - 750}} \quad (44)$$

where λ is the wavelength in μm and the temperature is 25°C.

The calculation of mode solutions and the effective mode index is slightly more complicated that with the planar waveguide. Methods have been developed for obtaining the mode solutions in rectangular optical waveguides, such as Marcatili's method [29] and the effective index method [30].

Marcatili's approximation assumes that the mode is well confined, and solves the scalar wave equation in each region of the generalized cross section seen in Fig. 6. Boundary conditions are then applied as before to ensure field components are continuous.

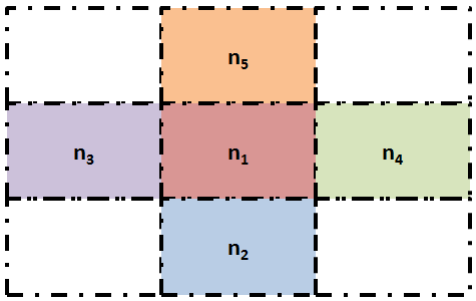

Fig. 6. Generalized cross section of the Marcatili method.

Note that the corners of the cross section are ignored by Marcatili's method, due to the assumption of a well confined mode. This introduces errors in the calculation which result in inaccurate calculations for modes that are not well confined. The effective index method is a way to overcome this limitation, and gives a much more accurate way to calculate the effective mode index.

For the effective index method, the waveguide is looked at in two separate instances, along each axis. The waveguide is first looked at in the narrower dimension that limits propagation. When the effective index of each of these portions is found, the device is then looked at along the other axis using these effective index values. Hence, the rectangular waveguide is treated and solved as two planar/slab waveguides.

Today there are numerous software packages available that will calculate mode solutions, and in our research group we take advantage of FimmWave Optical Mode Solver and FimmProp Optical Propagation Tool, both by Photon Design. This allows for the rapid calculation of mode profiles. The simulations in this work were carried out using the FMM Solver in FimmWave, which is a vectorial solver based on the film mode matching method [31]. While FimmWave comes with six built in mode solvers, the FMM Solver is designed to give the best performance for rectangular geometry waveguides and thin film layers [32], both of which describe our devices. The waveguiding structure is broken up into a series of vertical slices which are then solved for. Table 3 shows a summary of the simulation parameters that were used in this work.

Table 3. FimmWave simulation parameters.

Parameter	Value
Solver	FMM Solver (real)
Solver – Coordinate System	Gen WG
Mode Profile Resolution	250 x 160
Solver Parameters – (1d) nmode	80
Solver Parameters – Type	Semivec TM
Waveguide Window Size	50 x 25
Substrate Size	50 x 20
Diffused Waveguide Region	30 x 18

As with any calculation, there are limitations in the simulation capabilities of the software package. When working with these software packages, it is very important to

know the refractive indices of the materials you are working with. Simulations will give mode solutions that look good, except for the fact that the refractive index is too small.

C.2. Diffused Waveguide

Extending from the rectangular waveguide, a logical extension is to move from a step index profile to a gradient index profile. This gradient index profile is commonly seen in $LiNbO_3$ devices with titanium diffused waveguides ($Ti:LiNbO_3$) [11] and annealed proton exchange (APE) waveguides [12]. The effective index method can be expanded to consider diffused waveguide profiles [33]. Another way to look at diffused waveguides is to consider the scalar wave equation given in (19). It can be used to relate an optical mode profile to its refractive index profile.

The scalar wave equation can be used to calculate the refractive index profile from an observed fundamental mode pattern [34]. Consider the case of a separable transverse electric field,

$$E(x,y) = E_x(x)E_y(y). \tag{45}$$

Taking the scalar wave equation from (19) and rearranging it gives

$$n^2(x,y) = \left(\frac{\beta}{k_o}\right)^2 - \frac{1}{k_o^2}\frac{\nabla_T^2 E(x,y)}{E(x,y)} = n_{eff}{}^2 - \frac{1}{k_o^2}\frac{\nabla_T^2 E(x,y)}{E(x,y)}. \tag{46}$$

Assuming the second term in (46) is small, which is a valid assumption for diffused waveguides, the square root can be approximated as a Taylor Series where

$$\sqrt{N^2 + d} = N + \frac{d}{2N} - \frac{d^2}{8N^3} + \frac{d^3}{16N^5} - \cdots \tag{47}$$

which gives

$$n(x,y) \approx n_{eff} - \frac{1}{k_o^2 n_{eff}} \left(\frac{\nabla^2 E(x,y)}{E(x,y)} \right). \tag{48}$$

This varies slightly from the derivation of this equation in other references [35]. It is believed that [35] uses the substrate refractive index instead of the effective index in the denominator term since n_{sub} is a known value. However, the effective index can be easily estimated, and is already used elsewhere in the equation for k_o.

Viewing the third and fourth terms of the Taylor expansion as an error term, using the maximum expected values for E'' / E gives a maximum relative error of 0.44% when neglecting these terms.

In the case of (45), then (48) can be expressed as

$$n(x,y) \approx n_{eff} - \frac{1}{2 n_{eff} k_o^2} \left[\frac{1}{E_x} \frac{\partial^2 E_x}{\partial x^2} + \frac{1}{E_y} \frac{\partial^2 E_y}{\partial y^2} \right]. \tag{49}$$

Hence, the refractive index profile reconstruction becomes a matter of adding/subtracting small values to the effective index. Thus, the second derivative determines whether the Δn term is a positive or negative value. Since the optical mode can generally be approximated by a Gaussian profile, the second derivative of a Gaussian will be looked at. This method does not provide accurate reconstructions at the surface of the waveguide, and that is due to this Gaussian behavior. The tail end of a Gaussian will always have a negative second derivative, even when the index distribution is such that it should be adding to n_{eff}.

FimmWave simulated diffused optical mode profiles were used to obtain 2D intensity images that were then carried through (49) to obtain the refractive index profile. Since this is a simulated mode intensity, the refractive index profile that was simulated is known and can be used for comparison. The simulated mode intensity profile used is seen in Fig. 7.

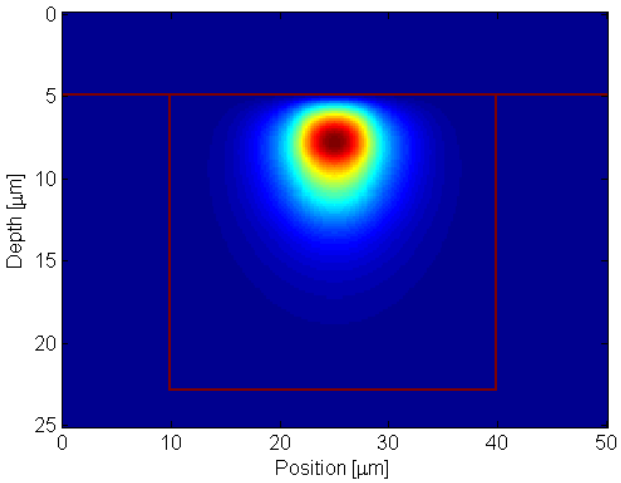

Fig. 7. FimmWave simulated mode profile showing waveguide simulation boundaries.

Even though this is simulated data, smoothing must still be applied to the data in order to obtain a valid second derivative. A rectangular smoothing algorithm, also known as a weighted average over a large window, gives a large loss in signal amplitude along with broadening of amplitude peaks [36]. Another method, Savitzky-Golay filtering [37], gives the same smoothing performance without a large loss in signal amplitude and deviation in signal peak widths. Carrying out (49) on both the raw and smoothed data gives the depth refractive index profile seen in Fig. 8.

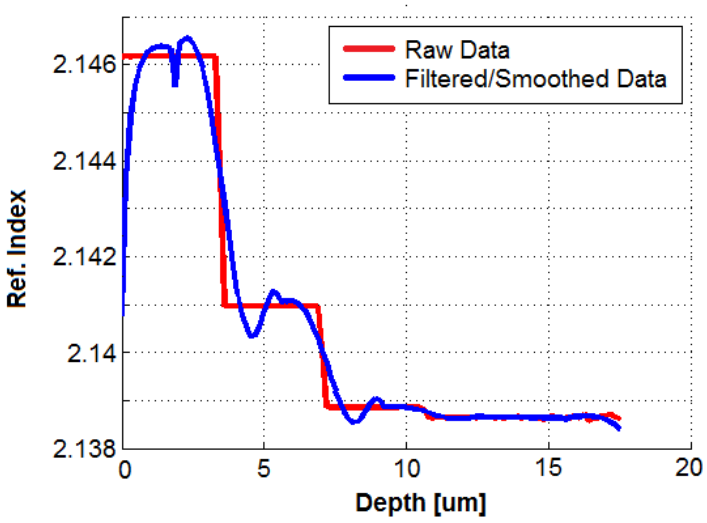

Fig. 8. Calculated refractive index along center depth profile.

The refractive index profile is expected to behave as a decaying half-Gaussian, and there are two main reasons for the errors in this calculated refractive index profile. The large index discontinuity at the air-$LiNbO_3$ interface cannot be accurately represented by the scalar wave equation [38]. Away from the optical mode, or rather deep in the substrate, the weak light intensities give a large uncertainty to the measured index values [34]. Since these two issues are on the edges of the calculated refractive index profile, curve fitting can be performed on the middle portion, as seen in Fig. 9. It can be seen that the curve fitted refractive index profile matches that of the simulation. The refractive index distribution is that of an annealed proton exchange waveguide, and as expected is a gradient profile.

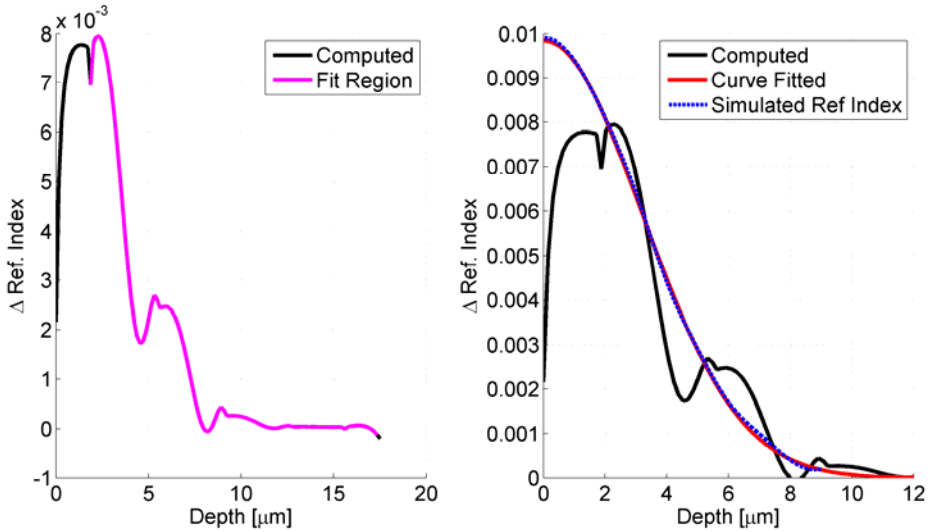

Fig. 9. Calculated refractive index profile from mode intensity.

When noise is added on top of the mode intensity profile, as would be the case in a real world measurement, the ability to accurately determine the refractive index distribution is reduced. Simulations and calculations show that when noise is added to the mode intensity profile, a minimum of 10% – 15% error can be expected.

With these two waveguide structures, rectangular and diffused waveguides, the As_2S_3 and Ti:$LiNbO_3$ waveguides used in our devices can be represented. With the optical waveguide background completed, it is now time to look at how multiple waveguides can be used to make functional devices.

C.3. Interferometers

An optical interferometer is a device that is designed to exploit the constructive/destructive coherent interference of light that results from optical path

length differences [39]. Recall that the speed of light is dependent on the refractive index

$$c = \frac{c_o}{n} \tag{50}$$

where c_o is the free-space vacuum speed of light given in (12) and n is the refractive index. Because of this varying speed of light, the optical path length (OPL) is used to describe waveguide distances. The OPL is the product of the physical length of the waveguide and the effective index of the optical mode

$$OPL = \ell \cdot n_{eff} . \tag{51}$$

Given a two path device, it follows from (51) that an optical path length difference (OPD) between two paths can be introduced, given by

$$OPD = OPL_1 - OPL_2 = \ell_1 n_{eff\,1} - \ell_2 n_{eff\,2} . \tag{52}$$

To achieve interference, an interferometer splits an initial beam into two (or more) beams that travel different optical paths, as seen in Fig. 10. These optical paths can either be different lengths of the same material, or lengths of materials with different refractive indices; anything to give an OPD when the paths are recombined. Recall that light is still an electromagnetic wave with a wavelength and a frequency, so the OPD can also be viewed as a delay, or phase shift, between the two paths. This delay can clearly be seen in a time domain response of an interferometer, as in Fig. 11, where each of the optical paths is represented by a peak. The difference in the peak amplitudes is due to the coupling between the two optical paths.

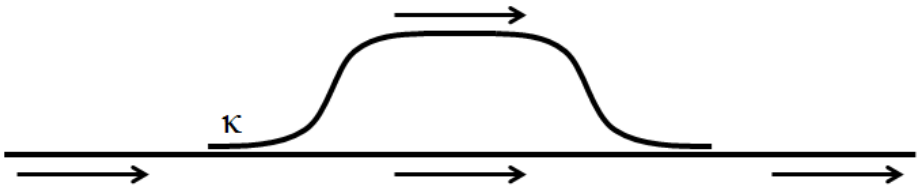

Fig. 10. Mach-Zehnder interferometer.

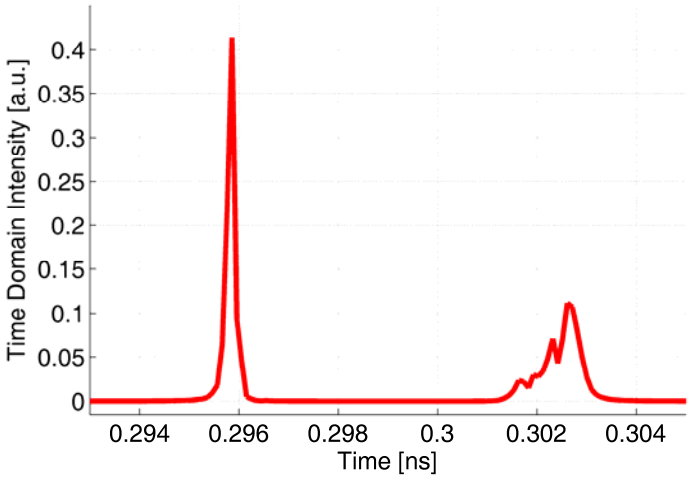

Fig. 11. Mach-Zehnder interferometer time domain response.

This time delay can also be thought of as a phase shift, which is given by

$$\Delta\varphi = \left(\frac{2\pi}{\lambda}\right) OPD \tag{53}$$

where $\Delta\varphi$ is the phase shift at wavelength free space wavelength λ. Along with the immediate observation in (53) that there is a wavelength dependence to the phase shift, there will also be a wavelength dependence to the optical path length difference related to the Sellmeier equations given in (27), (28), and (44). This gives a periodic ripple to the spectral response. The period of this ripple is the free spectral range (FSR) of the

device. The FSR is wavelength dependent due to the wavelength dependence of the refractive index, which will cause slight variations in the period. However, the main driving force behind the FSR is the optical path length difference, which follows an inverse relationship; the longer the optical path length difference, the smaller the spectral width of the FSR.

Interferometers can also be looked at in a digital filter approach [40],[41]. Consider the Fourier series

$$H(f) = \sum_{n=0}^{N} c_n e^{-j(2\pi fn - \phi_n)} \tag{54}$$

where *H(f)* is the frequency response of the filter, *N* is the filter order, and $c_n e^{j\varphi_n}$ is the complex weighting term. This can be viewed as splitting a signal into multiple parts (sinusoids) that are individually weighted before being recombined at the output. The optical analog of this is the interferometer. For our Mach-Zehnder interferometer, $N = 2$ and the weighting terms are adjusted by the coupling between the two paths and the path length losses. There is a finite delay because the device is only feed-forward, so the interferometer is viewed as a MA or FIR filter.

Interferometers are basic optical devices that take advantage of splitting optical modes and phase shifts. However, as is common in electronics and filters, feedback paths are often desired for more advanced device functionality which the interferometer lacks.

C.4. Ring Resonators

Keeping the two path device, but introducing a feedback path, turns the interferometer into an optical ring resonator. In terms of digital filters, this device now acts as an IIR filter. As will be shown later, this introduces more advanced device functionality. A ring resonator, as seen in Fig. 12, is assumed to act ideally as an allpass filter in the lossless case.

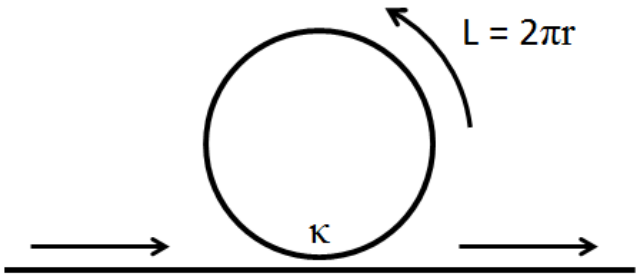

Fig. 12. Ring resonator, showing the feedback path.

The transfer function response for an all-pass ring resonator is given by

$$H(z) = \frac{c - \gamma z^{-1}}{1 - c\gamma z^{-1}} \tag{55}$$

where $c = \sqrt{1-\kappa}$, $z^{-1} = e^{-j\beta L}$, $\gamma = 10^{-\alpha L/20}$, β is the waveguide propagation constant, αL is the ring round-trip loss in dB, and κ is the power coupling ratio [42],[41]. The ring resonator is characterized by its free spectral range (FSR), which is determined by the path length of the ring. The FSR of a ring resonator is given by

$$FSR = \frac{c_o}{n_g L} \tag{56}$$

where n_g is the group index of the ring optical mode and L is the path length of the ring. Using Matlab to simulate this response, the amplitude and phase response of a 5 GHz ring resonator with a 50% coupling ratio is seen in Fig. 13. In order to see where the allpass filter terminology comes from, both the 0 dB/roundtrip and 2 dB/roundtrip loss cases are shown. Note that the 0 dB/roundtrip case has a constant magnitude response, while the phase response is similar between the two cases.

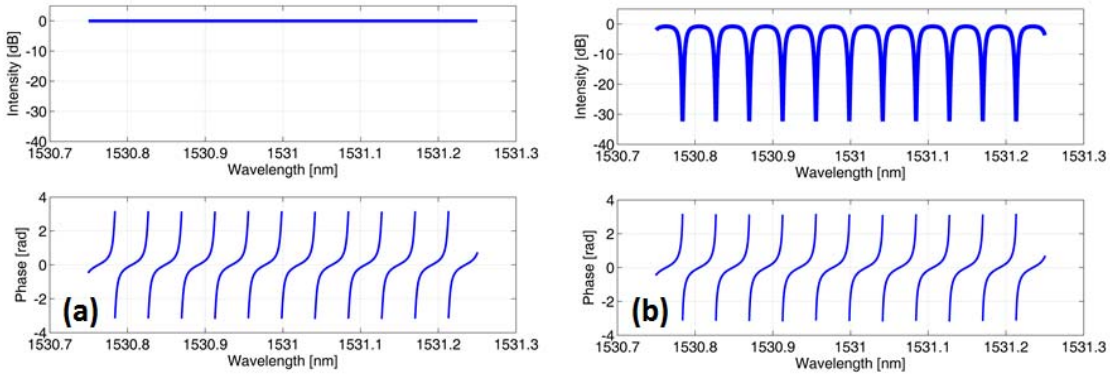

Fig. 13. Ring response, magnitude and phase, for a 5 GHz ring with 50% coupling. Round trip ring losses are (a) 0 dB and (b) 2 dB.

Because lasers operate at one fixed wavelength, we are generally interested in one period, or FSR, of this response. However, we would like to take advantage of the phase response across an entire FSR. As will be shown later, electro-optic tuning allows for taking advantage of the entire response across the FSR.

C.5. Coupled Mode Theory

In order to realize the interferometer and ring resonator devices with our hybrid device platform (Ti:$LiNbO_3$ and As_2S_3), it is important to be able to transfer the mode between waveguides. This is where coupled mode theory is important for our devices.

Simple directional couplers are formed by two parallel, closely spaced channel waveguides [43]. The coupling coefficient κ is set by the waveguide dimensions and the gap between the waveguides. As long as the waveguides are in close proximity, the power will oscillate between the two waveguides; hence the length of the coupling region is very crucial.

While this simple directional coupler structure would work great for two Ti:$LiNbO_3$ diffused waveguides, our device is two different waveguide structures. An adiabatic taper structure is used to transition the mode from the Ti:$LiNbO_3$ diffused waveguide to the As_2S_3 rib waveguide [23]. Adiabatic taper couplers are preferred to resonant couplers due to their tolerance for fabrication variations [44]. It is important for the slope of the taper to be gradual, especially with the significantly larger refractive index of the As_2S_3 material, so that there is not coupling into higher order modes and excess radiation losses [45]. As the taper width increases, the optical mode slowly transitions to the As_2S_3 waveguide, as seen in Fig. 14.

For our fabricated devices, we taper the As_2S_3 waveguide from 0.8 μm to 1.6 μm in the coupling region. After reaching a 1.6 μm width, the As_2S_3 waveguide is slowly bent away from the Ti:$LiNbO_3$ waveguide while further increasing to the 3.5 μm wide width used in the interferometers and ring resonators.

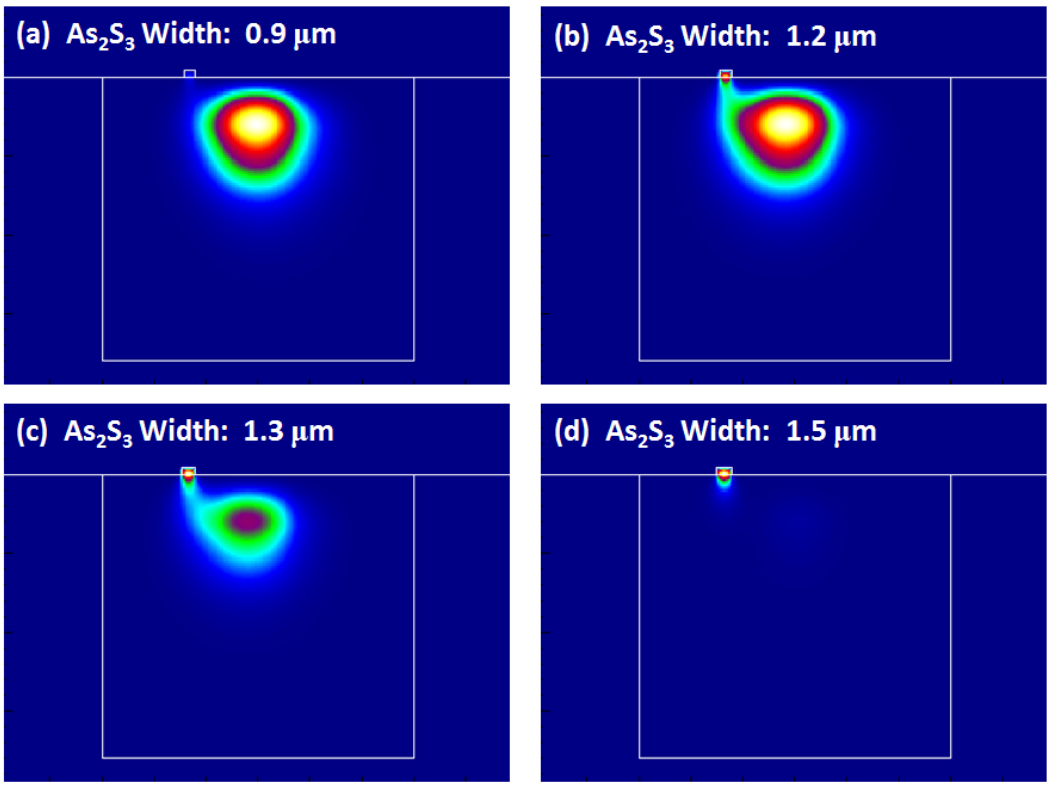

Fig. 14. Simulation of tapered coupling between Ti:$LiNbO_3$ and As_2S_3 waveguide. Mode profile for (a) 0.9 µm, (b) 1.2 µm, (c) 1.3 µm, and (d) 1.5 µm As_2S_3 waveguide width.

Once the As_2S_3 waveguide reaches the width at which it can support an optical mode, the higher index of the As_2S_3 waveguide makes it the dominant waveguiding structure [46]. Getting the As_2S_3 waveguide away from the Ti:$LiNbO_3$ waveguide once it is the dominant waveguiding structure reduces mode beating, but simulations and experimental results show that there is still some slight mode beating, as seen in Fig. 15.

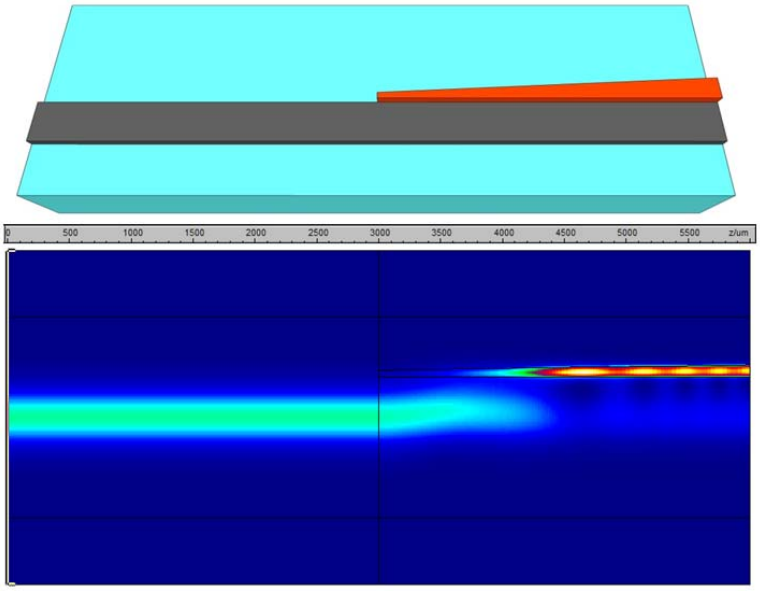

Fig. 15. Simulation showing tapered As_2S_3 (0.8 μm – 1.6 μm) mode coupling and slight mode beating.

The As_2S_3 tapers are placed beside the Ti:$LiNbO_3$ diffused waveguide due to the surface bump after diffusion and waveguide surface roughness, both of which increase optical losses. Another design parameter that is critical for performance is the taper starting tip width. Simulation results on taper tip widths and lengths can be seen in Table 4, where the values given are the power coupling percentages for a single 0.47 μm thick As_2S_3 up taper side coupled to a 7 μm wide Ti:$LiNbO_3$ diffused waveguide. The values given are the power coupling percentages from Ti:$LiNbO_3$ to As_2S_3 (1:1) and from Ti:$LiNbO_3$ to the next higher order mode (1:2) at 1531 *nm* wavelength.

Table 4. FimmProp simulations for single As_2S_3 up taper side coupled to 7 μm Ti:$LiNbO_3$.

	1000 μm length	2000 μm length	3000 μm length	5000 μm length
1.0 – 1.9 μm taper	1:1 – 33.15% 1:2 – 66.33%	1:1 – 57.86% 1:2 – 41.62%	1:1 – 61.73% 1:2 – 37.75%	1:1 – 84.66% 1:2 – 14.82%
1.3 – 1.9 μm taper	1:1 – 26.80% 1:2 – 71.92%	1:1 – 52.63% 1:2 – 46.09%	1:1 – 74.35% 1:2 – 24.83%	1:1 – 97.32% 1:2 – 1.41%
1.5 – 1.9 μm taper	1:1 – 5.65% 1:2 – 94.03%	1:1 – 6.24% 1:2 – 93.44%	1:1 – 6.89% 1:2 – 92.79%	1:1 – 7.06% 1:2 – 92.62%

The trends in Table 4 confirm the expected adiabatic taper behavior. Shorter taper lengths, which result in a larger slope, have larger higher order mode losses. While simulations show that a larger taper tip gives better performance in some instances, this behavior has not been observed with fabricated devices. It is shown that if the taper tip is too large, coupling is not supported. Further simulations with variations in the length of the taper to get the same slope with different starting tip widths shows that the starting tip width is more critical than the slope.

Experimental results confirm the increase in power coupling percentage with taper length, as shown in Fig. 16. There is a wavelength dependence to the coupling, which is expected due to the large index contrast between the two materials [21].

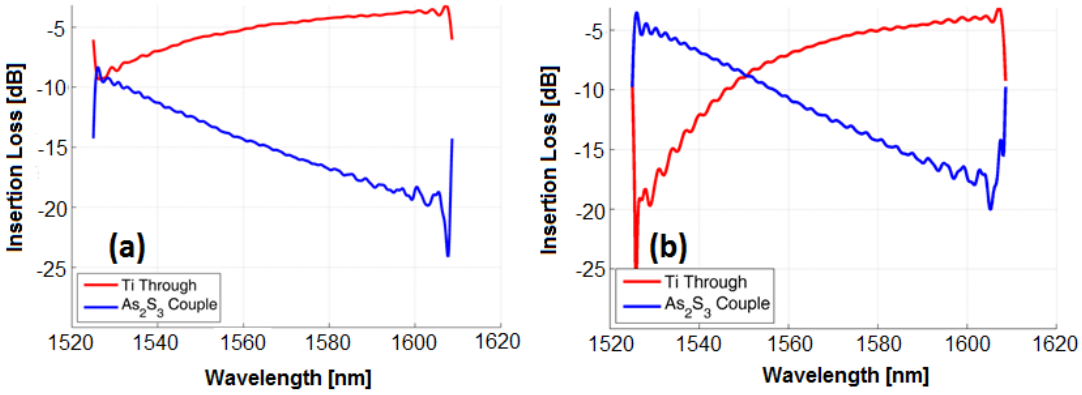

Fig. 16. Coupling between Ti:$LiNbO_3$ and As_2S_3 waveguides with (a) 2000 µm and (b) 4000 µm long tapers.

With interferometers, the largest extinction ratio is expected to occur when there is 50/50 coupling between the two path lengths. It follows that the intersection points in Fig. 16 are going to be where the path lengths have equal powers, and Fig. 17 shows that this is indeed when the largest extinction ratio is observed.

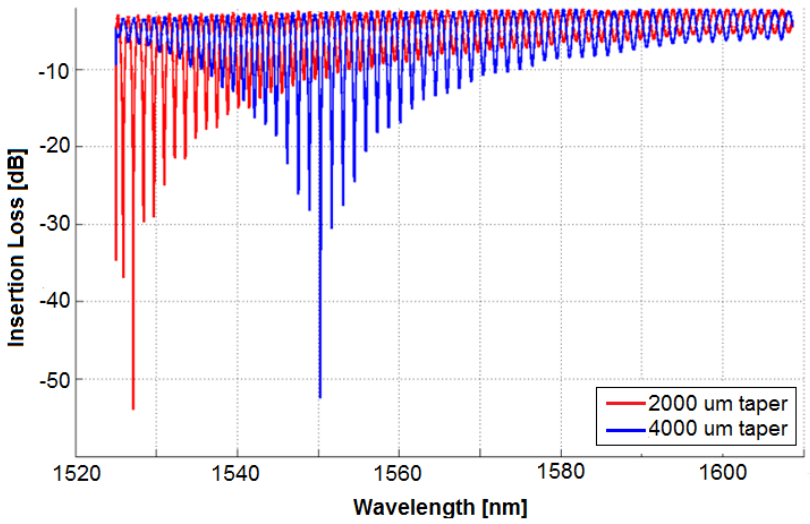

Fig. 17. Comparing extinction ratios for different MZI devices.

With the ability to transfer and propagate modes in different materials, it can be seen how complex optical devices can be made that take advantage of different material properties. However, the $LiNbO_3$ substrate that is being used has a very significant material property; the refractive index can be electro-optically tuned.

D. Electro-Optic Tuning

The electro-optic effect is a phenomenon where a refractive index change is induced by the application of an electric field. This is one of the fastest tuning options with inherently low loss, as thermooptic tuning which is commonly used in silicon devices is an order of magnitude slower [43].

Recall the index ellipsoid for an anisotropic crystal given in (26). A general way to look at the linear electro-optic effect is that it will change the shape of the index ellipsoid. There are two ways to change the shape of the index ellipsoid, either by elongating the axes or by rotating the index ellipsoid. Rotation of the index ellipsoid changes the principal axes, which can also be viewed as a polarization conversion. For our ring resonator device polarization conversion is not desired, so we are looking for electro-optic tuning without axial rotation.

D.1. Pockel's Effect

Instead of the index ellipsoid equation, it is more convenient to express the electro-optic effect in terms of impermeability, where

$$B \equiv \frac{1}{\varepsilon_r} = \frac{1}{n^2}. \tag{57}$$

Using the notation introduced in (57) then (26) can be expressed as

$$B_1 X^2 + B_2 Y^2 + B_3 Z^2 + 2B_4 YZ + 2B_5 XZ + 2B_6 YZ = 1. \tag{58}$$

This more closely resembles the equation in (26) if the system is diagonalized and the principal axes coincide with the coordinate system, in which case the mixed terms $B_4 = B_5 = B_6 = 0$. When an electric field is applied, thus causing the index ellipsoid to change due to the electro-optic effect, (58) becomes

$$B_1' X^2 + B_2' Y^2 + B_3' Z^2 + 2B_4' YZ + 2B_5' XZ + 2B_6' YZ = 1. \tag{59}$$

The electro-optic effect in $LiNbO_3$ follows the linear Pockel's effect [43]. This means that the relationship of the impermeability before and after the application of the electric field is given by

$$\Delta B_i = B_i' - B_i \equiv \Delta\left(\frac{1}{n_i^2}\right) = \sum_{j=1,2,3} r_{ij} E_j \qquad \text{for i=1,2...6} \tag{60}$$

where r_{ij} is the electro-optic tensor element. Expressing (60) as a matrix equation gives

$$\begin{bmatrix} \Delta B_1 \\ \Delta B_2 \\ \Delta B_3 \\ \Delta B_4 \\ \Delta B_5 \\ \Delta B_6 \end{bmatrix} = \begin{bmatrix} r_{11} & r_{12} & r_{13} \\ r_{21} & r_{22} & r_{23} \\ r_{31} & r_{32} & r_{33} \\ r_{41} & r_{42} & r_{43} \\ r_{51} & r_{52} & r_{53} \\ r_{61} & r_{62} & r_{63} \end{bmatrix} \begin{bmatrix} E_x \\ E_y \\ E_z \end{bmatrix}. \tag{61}$$

For $LiNbO_3$, the electro-optic coefficient tensor is given by [43]

$$r_{ij} = \begin{bmatrix} 0 & -3.4 & 8.6 \\ 0 & 3.4 & 8.6 \\ 0 & 0 & 30.8 \\ 0 & 28 & 0 \\ 28 & 0 & 0 \\ -3.4 & 0 & 0 \end{bmatrix} \quad pm/V . \tag{62}$$

Consider the application of an arbitrary electric field E^e along a principal axis, with optical field polarization E^w propagating along a principal axis of $LiNbO_3$ substrate. The resulting refractive index change can be calculated using (60). Recall that axial rotation is not desired, meaning a solution is sought without mixed terms. The possibilities for electro-optic tuning, with the applicable tuning coefficients, are summarized in Table 5 where $r_{22} = 3.4\ pm/V$, $r_{13} = 8.6\ pm/V$, and $r_{33} = 30.8\ pm/V$.

Table 5. Electro-optic tuning of $LiNbO_3$ without axial rotation.

	$\boldsymbol{E}_x^e$	$\boldsymbol{E}_y^e$	$\boldsymbol{E}_z^e$
$\boldsymbol{E}_x^w$	--	r_{22}	r_{13}
$\boldsymbol{E}_y^w$	--	r_{22}	r_{13}
$\boldsymbol{E}_z^w$	--	--	r_{33}

It naturally follows that r_{33} is the desired tensor coefficient, since it gives the strongest tuning capability. This tuning coefficient can only be taken advantage of with an optical field polarization along the z-axis, and an electric field along the z-axis.

D.2. Mode Confinement and Field Overlap

The field distribution of the optical polarization mode in the dielectric waveguide is known as the confinement factor, or filling factor. The confinement factor gives a measure of the amount of optical power present in the waveguide core. For the case of an As_2S_3 rib waveguide, it would be the measure of the amount of power confined in the As_2S_3 material. If the total optical power is considered to be the sum of the power in the core (P_{n1} = As_2S_3), the substrate (P_{n2} = $LiNbO_3$), and the cladding (P_{n3} = air or SiO_2) where the power is determined by (20), then the confinement factor Γ is defined as

$$\Gamma = \frac{P_{n1}}{P_{n1} + P_{n2} + P_{n3}} \tag{63}$$

The confinement factor is important when it comes to considering electro-optic tuning of an optical mode propagating in an As_2S_3 rib waveguide. Recall that the $LiNbO_3$ substrate is electro-optically tunable, not the As_2S_3 waveguide. However, if the confinement factor of the As_2S_3 mode is < 100% then that means there is optical mode power present in the $LiNbO_3$ substrate, allowing for electro-optic tuning. Through the As_2S_3 waveguide dimensions, we are able to keep a portion of the mode in the substrate. However, a SiO_2 cladding on top of the As_2S_3 waveguide increases the confinement factor, reducing the tuning efficiency.

Simulations were carried out on As_2S_3 modes with varying SiO_2 buffer layer thicknesses. The dimensions of the As_2S_3 waveguides have already been optimized for TM mode coupling and low loss propagation [47]. The bending radii of the ring resonator, along with the associated bending losses, limit the minimum thickness of the

As_2S_3 film that can be used. The mode confinement for a 0.47 μm thick As_2S_3 film, which is the thickness used to support TM mode propagation, was simulated for varying waveguide widths and SiO_2 buffer layer thicknesses, with the results seen in Fig. 18.

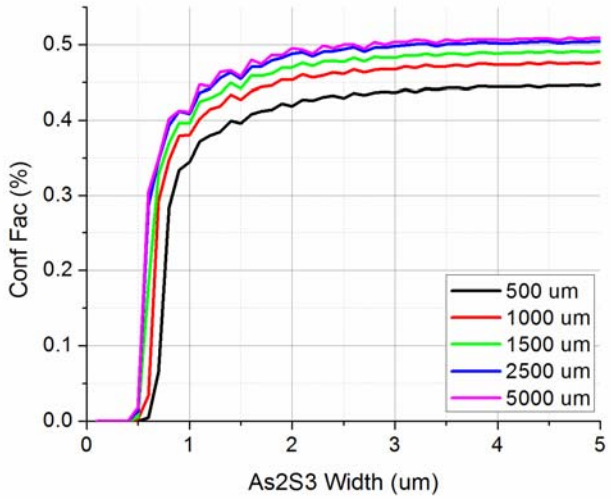

Fig. 18. Mode confinement for 0.47 um As_2S_3 with SiO_2 cladding.

As can be seen in Fig. 18, the confinement factor in the As_2S_3 waveguide increases as the SiO_2 buffer layer thickness is increased. This increase in mode confinement has a noticeable effect on the electro-optic tuning strength, which will be discussed in the following sections.

D.3. Coplanar Strip Electrodes

Recall that due to the anisotropic nature of $LiNbO_3$ the substrate is available in different crystal cuts, where the cut describes the principal axis that is normal to the

substrate (see Fig. 2). As seen in Table 5, r_{33} can only be taken advantage of with both an optical field polarization and electric field along the z-axis. This means that the substrate crystal cut is a very important design parameter when wanting to utilize electro-optic tuning.

A coplanar strip electrode structure (CPS) consists of two parallel striplines with a gap between them, as seen in Fig. 19. With a gap between the two electrode strips, an electric field is created along the shown electric field lines. It can be seen that this allows for two possibilities for the electric field direction, a horizontal and a vertical electric field. While a true vertical electric field could be created by placing the ground electrode on the bottom of the substrate, the substrate thickness (0.5 – 1 mm) would result in a weak electric field.

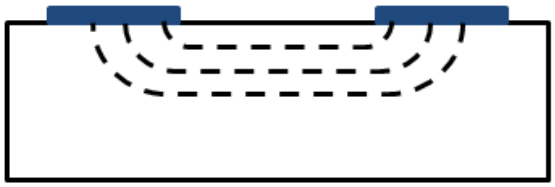

Fig. 19. Coplanar strip electrodes with electric field lines shown.

For propagation along a waveguide, there are two possible optical field polarizations, the TE and TM modes. The optical field polarizations are shown in Fig. 20.

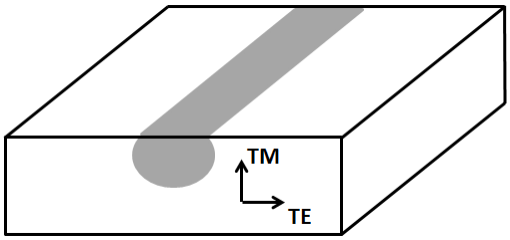

Fig. 20. Optical field polarizations for mode propagating along waveguide.

When seen graphically, as in Fig. 19 and Fig. 20, it is easy to see how the limitations imposed for electro-optic tuning with r_{33} and no axial rotation apply. For the TE polarization, where the optical field polarization is needed along the z-axis, a horizontal electric field is also used. In this orientation, the waveguide can be fabricated in the gap between the electrodes. Tuning of the TE polarization with r_{33} requires either x-cut, y-propagating substrate or y-cut, x-propagating substrate.

For the TM polarization, while the optical field polarization is still needed along the z-axis, the use of a vertical electric field is necessitated. This necessitates an overlap between the waveguide and the electrodes. Tuning of the TM polarization with r_{33} requires z-cut substrate [48]. These two tuning cases for TE and TM polarizations are demonstrated in Fig. 21.

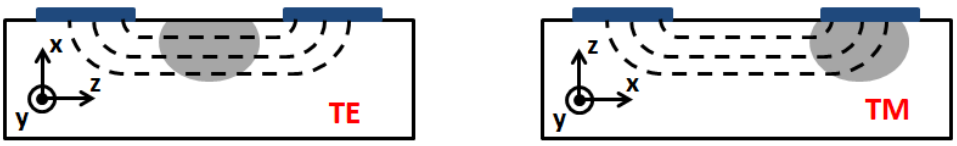

Fig. 21. Electrode orientation and substrate crystal cut for TE and TM polarization tuning with r_{33}.

A literature search reveals that much work has gone into the design of CPS electrode structures, and how to best optimize the tuning achievable with them. One way to improve the bandwidth is with asymmetric coplanar strip (ACPS) electrodes, where the ground plane is much wider that the other electrode [49]. The only design consideration that can be found on the ground electrode is that it be "significantly larger" than the signal electrode [50], so for this work an order of magnitude was considered significant.

Theoretically, an infinite bandwidth is possible when there is perfect velocity matching, meaning that the microwave signal is traveling at the same phase velocity as the light. One way to improve velocity matching with coplanar strip electrodes is to etch the backside of the substrate, creating a backside slot under the waveguiding region [51]. Changing the thickness of the substrate reduces the microwave index, and also has the added benefit of increasing the electric field.

Thick electrode and buffer layers are also beneficial in obtaining velocity matching [52]. However, even under perfect velocity matching conditions, the bandwidth is limited by the electrode loss. Because of this limitation, impedance matching becomes an important design consideration. Neglecting buffer layer thickness, metal thickness, and mode overlap, a 50Ω impedance can be achieved with a gap/width ratio of 0.65 for the CPS case [49] and 1.7 for the ACPS case [53]. However, the impedance is also dependent on the electrode buffer and metal thicknesses. The impedance will decrease as the metal thickness is increased, and will increase as the buffer thickness is increased. In looking at plots of the characteristic impedance as a

function of buffer and electrode thickness [50],[54], it can be seen that major fluctuations in the impedance are observed when film thicknesses are greater than 1 μm. While these thick films are desired to minimize the electrical static resistances and for velocity matching, it has already been seen that due to As_2S_3 mode confinement concerns that thin films less than 1 μm in thickness are desired, especially for the oxide cladding/buffer layer. Hence, for this work the ACPS gap/width ratio of 1.7 was utilized.

Taking into account the mode confinement considerations mentioned previously, and shown in Fig. 18, the tuning strength for electro-optic tuning of a 0.47 μm thick As_2S_3 waveguide was calculated and is shown in Fig. 22. An ACPS electrode structure with 500 nm thick Al electrodes having a 7 μm wide gap and 4 μm wide signal electrode was used for this simulation. Oxide cladding/buffer layer thicknesses of 150 *nm* and 300 *nm* were used for this simulation.

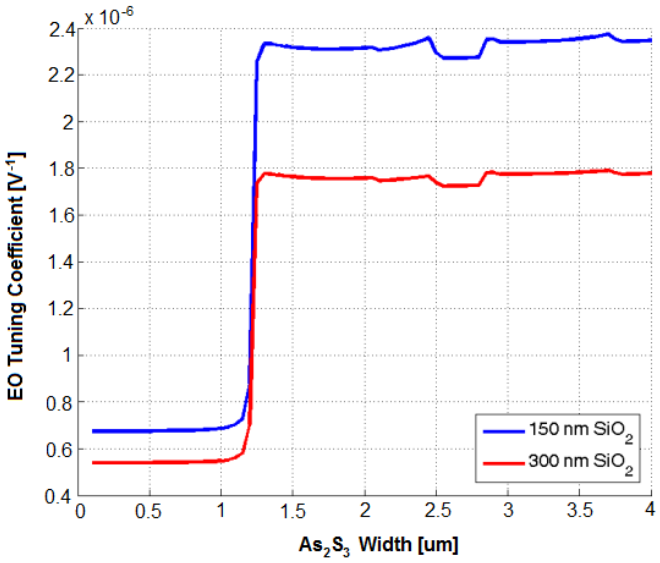

Fig. 22. Electro-optic tuning coefficient for varying As_2S_3 waveguide width and SiO_2 buffer layer thickness.

The sudden increase in the tuning coefficient at 1.25 μm is expected, as that is when the As_2S_3 waveguide begins to support the optical mode (recall Fig. 14) and pulls the mode to the surface. Prior to this width, the tuning coefficient is just for tuning with r_{13} in the Ti:$LiNbO_3$ indiffused waveguide. Once the As_2S_3 waveguide supports the optical mode, there does not seem to be a significant dependence on the waveguide width. However, there is a significant decrease in the tuning strength when the buffer layer thickness is increased from 150 *nm* to 300 *nm*; a 24% reduction in tuning strength.

Metals are strong absorbers of optical modes, thus in order to place an electrode over the waveguide, as seen in Fig. 21, would require the use of a thick buffer layer. However, as seen in Fig. 22 thick buffer layer would be detrimental to electro-optic

tuning of an As_2S_3 confined mode. These tradeoffs necessitate the placement of the electrodes along either side of the waveguide.

D.4. Phase Shifting

It has already been shown that electro-optic tuning changes the refractive index of the substrate. As a result, this will also change the effective index of the optical mode. In terms of electro-optic tuning and modulators, it does not take a significant refractive index change to introduce large phase shifts. Consider a π phase shift at a wavelength of 1531 *nm*. From (53) it can be calculated that

$$OPD = \frac{\Delta\varphi \cdot \lambda}{2\pi} \tag{64}$$

and an optical path length difference of 0.7655 μm is necessary at 1531 *nm*. This change in optical path length will be caused by a refractive index change; the physical length of the device will not change. Then the necessary refractive index change is given by

$$\Delta n = \frac{OPD}{\ell_t} = \frac{0.7655um}{\ell_t} \tag{65}$$

where ℓ_t is the length of the tuning path. Consider a 1 *cm* long tuning path, then a π phase shift at 1531 *nm* only requires $\Delta n = 7.655 \times 10^{-5}$. While at first glance it appears that this suggests the tuning path should be made as long as possible, keep in mind that the bandwidth scales as $1/\ell_t$ [53]. However, in an interferometer setup one can take

advantage of the two paths and tune each branch of the interferometer, reducing the necessary index change while not increasing the electrode length.

The necessary tuning voltage to achieve this index change can be determined by (60). Consider the coplanar strip electrode structure demonstrated in Fig. 21. On an x-cut $LiNbO_3$ substrate with y-propagation, the TE polarization will observe refractive index n_e. From electro-optic tuning, the new refractive index n_e' will be

$$n_e' = n_e + \Delta n_e = n_e + \frac{1}{2} n_e^3 r_{33} E_z^e . \tag{66}$$

Combining this result with (53) gives

$$\Delta\varphi = \left(\frac{2\pi}{\lambda}\right)\left[\frac{1}{2} n_e^3 r_{33} E_z^e\right] \ell_t = \frac{\pi n_e^3 r_{33} E_z^e}{\lambda} \ell_t \tag{67}$$

where the electric field E_z^e is determined by the voltage applied to the electrodes, along with the gap between the electrodes. The induced refractive index change is also determined by the overlap between the optical polarization field and the electric field [43]. The overlap integral between these two fields is expressed as Γ_o, the reduction factor of the applied electric field which is a different quantity than the Γ in (63), and is always less than unity. Then (67) is expressed as

$$\Delta\varphi = \left(\frac{\pi n_e^3 r_{33}}{\lambda}\right)\left(E_z^e \Gamma_o\right) \ell_t \approx \left(\frac{\pi n_e^3 r_{33}}{\lambda}\right)\left(\frac{V}{g} \Gamma_o\right) \ell_t \tag{68}$$

where V is the voltage applied to the ACPS electrodes and g is the gap between the electrode striplines. For Ti:$LiNbO_3$ waveguides this reduction factor is roughly around $\Gamma = 0.85$ [9],[55].

A figure of merit for modulator performance is the V_π voltage, or the voltage required to obtain a π phase shift. However, because of the dependence on tuning path length, the voltage-length product is a useful figure of merit for modulator/switch devices [8]. For Ti:$LiNbO_3$ devices utilizing r_{33}, this number is desired to be around 5 *V-cm* for E band (1360 – 1460 nm) devices [9],[8] and is expected to be similar for C band (1530 – 1565 nm) devices.

D.5. Coupling Tuning

In coupling regions, multiple modes interact with different relative phases. For a taper coupler, supermode theory can be used to analyze the coupling between the waveguides [56]. The supermodes are the two modes supported in the taper region, and the goal of taper coupling is to transfer the energy of a supermode from one waveguide to the other.

In terms of ring resonators, it follows from the transfer function in (55) that coupling tuning, or a change in the power coupling ratio, will cause a change in the extinction ratio as seen in Fig. 23.

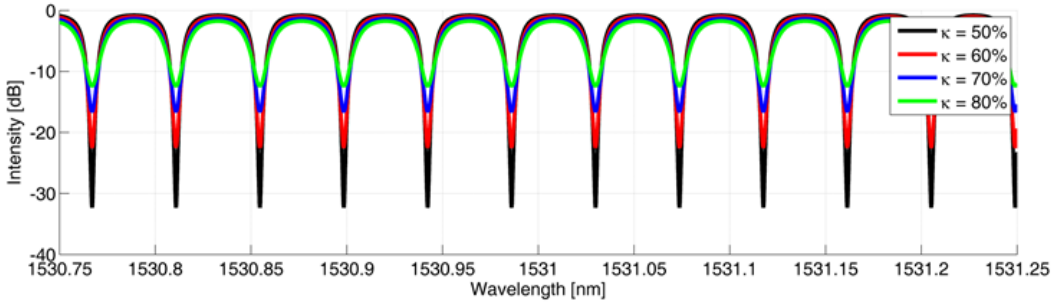

Fig. 23. Change in ring resonator coupling percentage seen as a change in extinction ratio.

However, the transfer function in (55) is for an ideal resonator with an identical phase between the pole and zero. Real world fabricated devices step away from this ideality, and can be modeled by treating the coupling region as asymmetric Mach-Zehnder interferometer [42] which is seen in Fig. 24. Each coupling region, which is an As_2S_3 taper side coupled to the Ti:$LiNbO_3$ waveguide, has a power coupling ratio κ_i. The two branches of the Mach-Zehnder interferometer represent the two supermodes that are supported in the coupling region, and each branch/supermode has a loss represented by the transmission coefficient γ_i. These parameters are set during the fabrication process and cannot be changed.

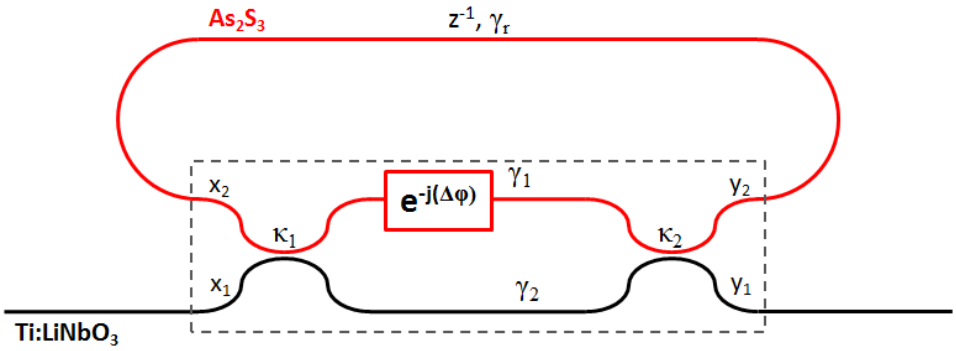

Fig. 24. Ring resonator, with coupling region treated as an asymmetric Mach-Zehnder interferometer.

In the region between the two As_2S_3 tapers, we have connected the tapers with an 0.8 μm wide As_2S_3 strip, which is the same as the starting width of the taper. The electrodes for electro-optic tuning run the length of this region, as seen in Fig. 25. This As_2S_3 strip allows for two modes, or supermodes, to be supported in this region. These supermodes have different mode profiles and effective indices, causing them to react differently to electro-optic tuning. Simulations on the electro-optic tuning strength for different As_2S_3 waveguide widths can be seen in Fig. 26.

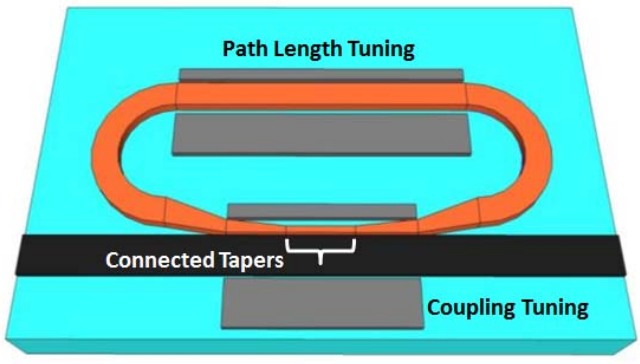

Fig. 25. Overall device structure of electro-optically tunable ring resonator.

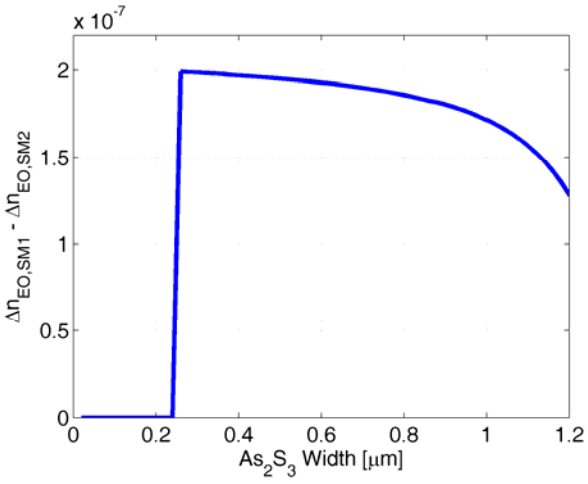

Fig. 26. Electro-optic tuning strength on supermodes for different As_2S_3 waveguide widths.

As seen in Fig. 26, the width of the As_2S_3 waveguide side coupled to the Ti:$LiNbO_3$ waveguide affects the electro-optic tuning difference between the supermodes. Above a width of 1.2 μm, the mode is supported in the As_2S_3 rib waveguide. Due to the use of contact lithography, a 0.8 μm As_2S_3 strip is the smallest width that can be fabricated, and also happens to be the same as the starting width of the taper. Electrodes placed in the coupling region will electro-optically tune both supermodes, so a phase shift will be caused by the difference in the index change difference between the two supermodes. It can be seen in Fig. 27 that for everything else held constant (coupling ratios and losses), a change in the phase shift in the coupling region affects the extinction ratio. Recall from Fig. 23 that a change in the extinction ratio is also evident of a change in the coupling percentage.

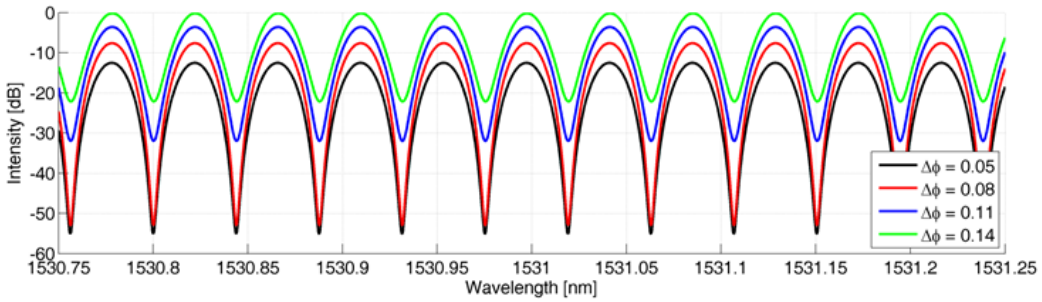

Fig. 27. Simulated ring response with difference in coupling region phase delay. Simulated for κ_1=0.4, κ_2=0.6, γ_1=γ_2=0.1, and αL = 2 dB.

There is also a frequency dependence in the coupling region which will cause the round trip loss and coupling percentage to vary with wavelength, which was not simulated. This frequency dependence is also set during the fabrication process.

E. Waveform Generation

With tuning capabilities for a ring resonator, it is possible to perform complex waveform generation. Specifically, non-linear frequency chirps can be obtained relatively easy with a ring resonator [57].

Recall the ring resonator transfer function given in (55) and magnitude/phase response shown in Fig. 13. Changing the power coupling ratio κ of the ring will change the amplitude and phase response. Since the end goal is to have an all-pass filter with a constant magnitude response, the focus will be on the phase response. The relationship between the power coupling ratio and phase can be seen in Fig. 28.

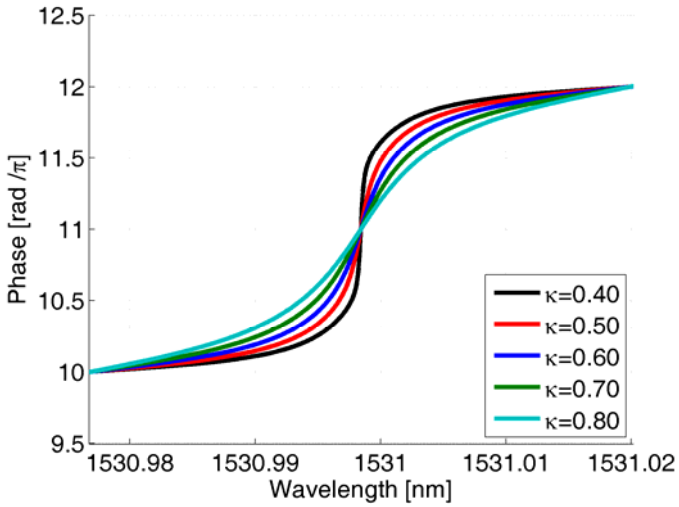

Fig. 28. Relationship between power coupling ratio and phase response.

While the shape of the phase response can be changed by adjusting the power coupling ratio, it still does not allow for a fixed wavelength to traverse the response. Applying a phase shift to the ring via electro-optic tuning, as given in (68), allows for traversing the phase response. A phase shift, or change in the optical path length of the ring resonator, will shift the amplitude and phase response curves. The ring response with a change in the optical path length of the ring resonator is shown in Fig. 29. Note that only a $\pm\frac{\pi}{2}$ phase shift is shown for graphical purposes.

Following from the linear Pockel's effect, the phase change is linear with the refractive index change. The shift to lower or higher wavelengths is determined by either a decrease or increase in the refractive index respectively, which is simply determined by the direction of the electric field between the ACPS electrodes.

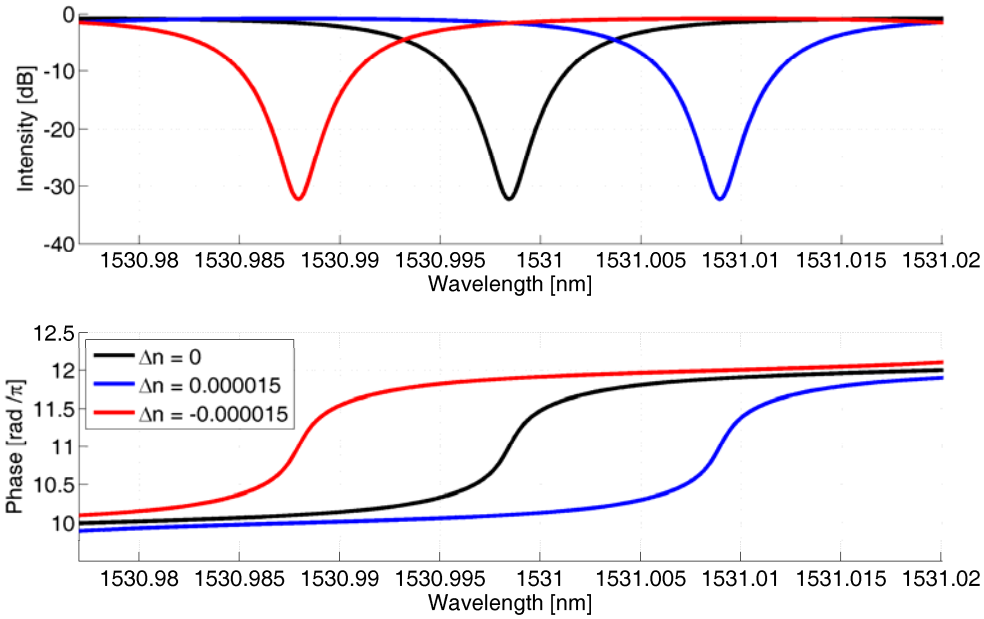

Fig. 29. Ring response with a change in path length refractive index.

It follows that if a time varying voltage is applied to the electrodes there will also be a time varying phase response. The simulated phase response over time for a 5 GHz ring resonator with 50% power coupling ratio modulated at 100 MHz with the necessary voltage to give a $\pm\pi$ phase shift is shown in Fig. 30.

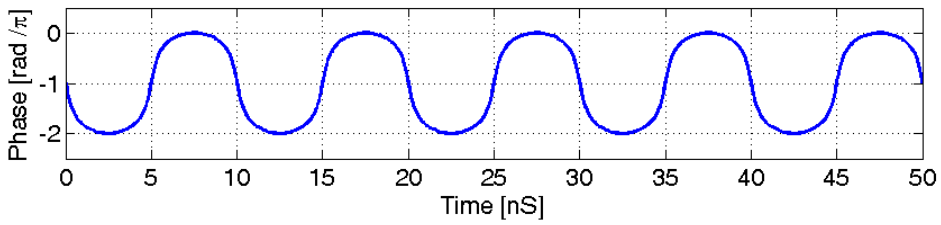

Fig. 30. Phase response with 100 MHz modulation on ring refractive index.

The instantaneous frequency, which is what we are interested in when considering frequency chirps, is related to the phase; it is the rate of change of the instantaneous phase. Hence, the instantaneous frequency can be found by taking the derivative of Fig. 30. The chirps with different power coupling ratios can be seen in Fig. 31.

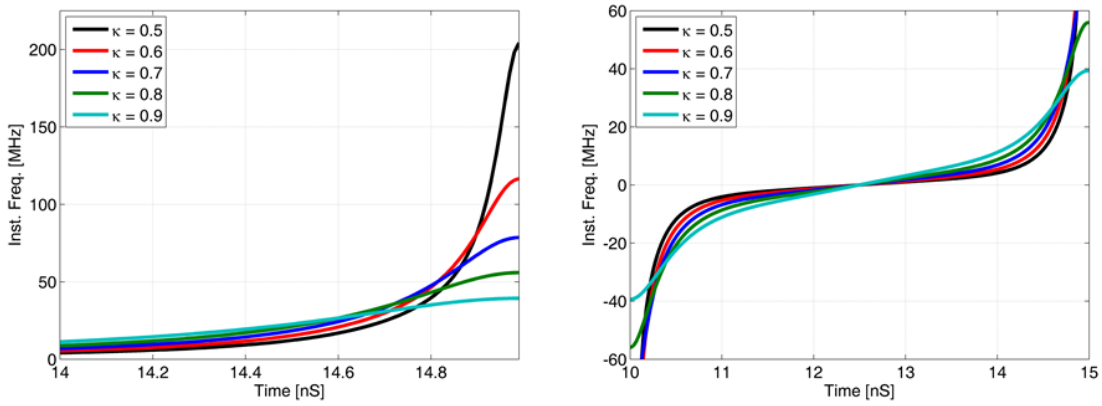

Fig. 31. Chirp with 100 MHz modulation and varying ring κ.

Note that in the cases of a smaller power coupling ratios, the chirp has instantaneous frequencies much larger than the modulation frequency. However, that comes at the expense of a fairly linear chirp in the middle portion of the curve. For an equal comparison of their non-linear shape, all chirps were normalized by their maximum frequency and compared to a hyperbolic tangent function, as seen in Fig. 32. The hyperbolic tangent function is a chirp signal of interest for some applications [58]. Note that a simple sinusoidal drive on the electrodes gives this non-linear chirp ability.

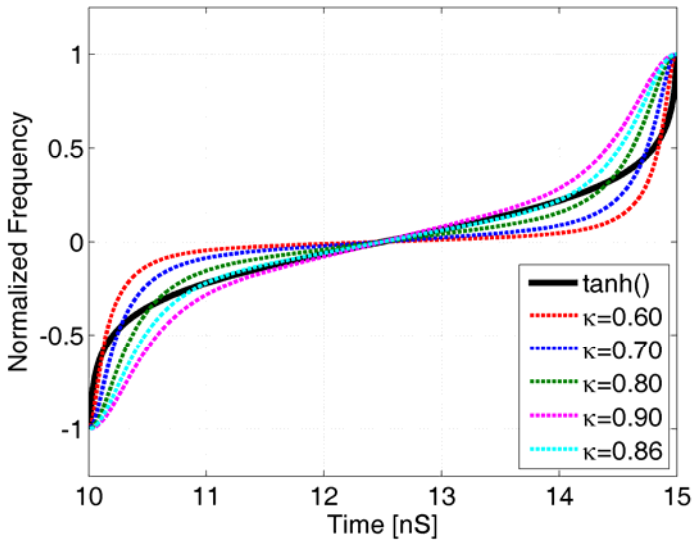

Fig. 32. Chirp comparison to a tanh() function.

Based on this the optimum power coupling coefficient for the ring is 86%. However, it can be seen that with one ring it is difficult to get an exact hyperbolic tangent chirp function. Multiple rings could be cascaded to come closer to the desired response [59].

For a given power coupling ratio, an increase in the round trip loss of the ring resonator reduces the non-linearity of the response, having almost the same effect as a decrease in the power coupling ratio. Hence, it is desired to have both a high power coupling ratio and low round trip losses in the ring resonator.

F. Device Measurement

In order to see all of the above theory at work, it is necessary to optically test the fabricated devices to determine their properties. For this work two main setups were

used, one for DC electrode measurements and the other for modulated electrode measurements. Both setups will be described below, with the results from these setups found in Chapter IV.

F.1. DC Electrode Test Setup

The first setup is for measuring DC electrode performance, and it takes advantage of a LUNA Technologies optical vector analyzer (OVA). The OVA is a benchtop system that provides comprehensive characterization of our waveguide devices. An internal laser has a swept wavelength range from 1525 – 1610 *nm* with a 1.6 *pm* resolution. A device under test (DUT) is placed in the fiber path between the source output and detector input of the OVA, as seen in Fig. 33. For coupling into the DUT the optical fiber is stripped of its polymer jacket, cleaved to 90°, and butt coupled to the polished facet edge of the DUT [60]. Three axis staging is used for precise alignment, with an optical power meter monitored real-time during alignment. Index matching gel is used on the cleaved fiber to reduce coupling losses.

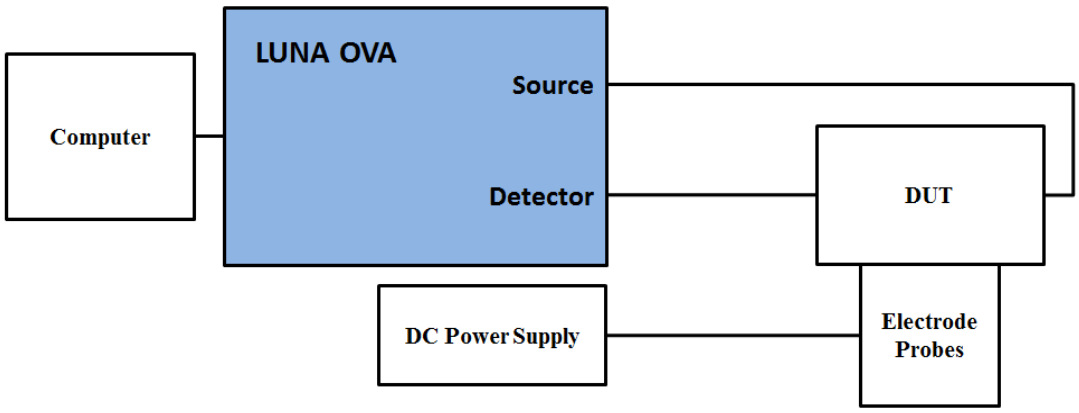

Fig. 33. DC electrode test setup, utilizing LUNA OVA.

The LUNA OVA calculates a Jones matrix element for the DUT at each wavelength measurement and computer software displays the measured response as a function of wavelength. Matlab code has been developed in our research group that takes the Jones matrix elements from the OVA and further processes them. The OVA has a calibration process that only relies on polarization paddles placed in the DUT path. Our Matlab code uses OVA measurements made with a fiber-to-fiber measurement and a wire grid polarizer to further calibrate the device.

Utilization of Jones matrix elements requires the use of Jones calculus, which was developed by R. Clark Jones to give a convenient matrix description of polarization [39]. Two-element column vectors represent light in various modes of polarization and a 2 x 2 matrix can be used to represent the overall effects of a device. For a 2 x 2 Jones matrix

$$\boldsymbol{M} = \begin{bmatrix} a & b \\ c & d \end{bmatrix} \tag{69}$$

a, *b*, *c*, and *d* describe the manner in which the device modifies the polarization of the light that passes through it. When measuring our device under test, we use an optical vector analyzer (OVA) from LUNA Technologies that has a tunable laser source. As the wavelength is swept, a Jones matrix element $\boldsymbol{M}_i$ is measured at every wavelength across the spectrum. From these measurements, the insertion loss (IL) and average group delay (GD) can be calculated for each wavelength as

$$IL_i = 10\log\left(\frac{|a_i|^2 + |b_i|^2 + |c_i|^2 + |d_i|^2}{2}\right) \tag{70}$$

$$GD_i = \left(\frac{a_i^* a_{i+1} + b_i^* b_{i+1} + c_i^* c_{i+1} + d_i^* d_{i+1}}{\Delta\omega}\right) \tag{71}$$

where $\Delta\omega$ is the frequency difference between consecutive measurements. Our algorithm allows for the polarization specific group delay for each matrix element to be calibrated. Recall that for our ring resonators we are interested in both the magnitude and phase information. The insertion loss provides a magnitude measurement, while the group delay provides a phase measurement. The group delay, with a negative sign, is the differentiation of the phase response, with respect to frequency.

Since the OVA makes measurements across a wavelength sweep, it can only be used to measure DC electrode voltages where the tuning response is at steady state during the wavelength sweep. The spectral response of the applied DC voltage is observed, and electro-optic tuning calculations carried out on the spectral information. Plots showing this spectral response can be found in Chapter IV.

F.2. Electrode Modulation Test Setup

The second setup is built up on an optical table to provide modulated electrode voltage measurements, and the block diagram can be seen in Fig. 34. A tunable laser source is used, but is operated at a fixed wavelength while carrying out measurements. The tunability of the laser is used to avoid having a DC bias on the electrode voltage. A high speed photodetector is placed on the output to measure the response.

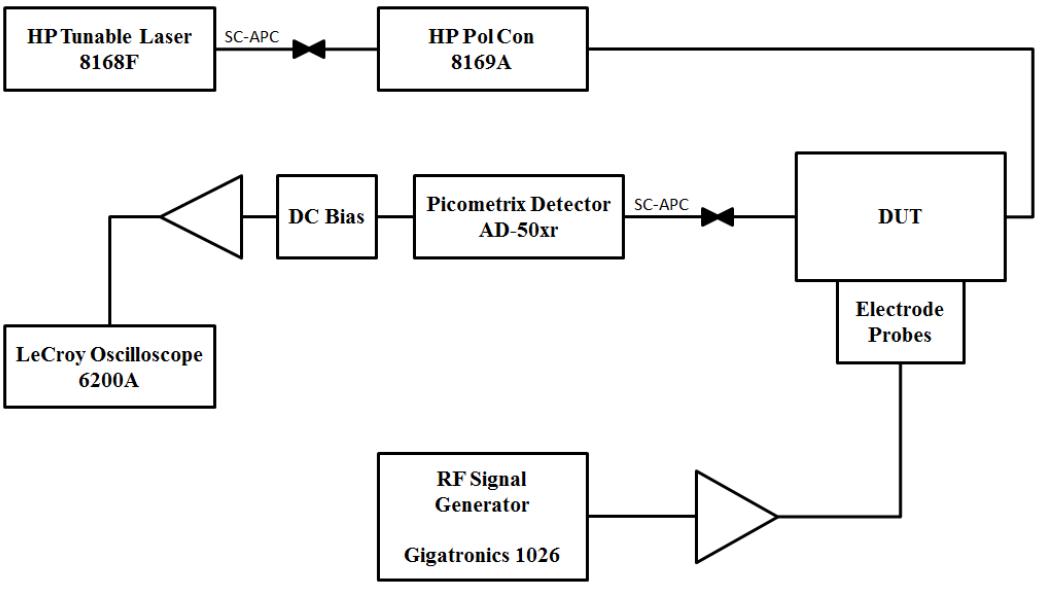

Fig. 34. Electrode modulation test platform.

Because of the use of r_{13} instead of r_{33} for electro-optic tuning in this work, the tuning voltages for these devices is larger than would be desired. Hence, the RF amplifier used to drive the electrode probes becomes a significant component of this setup. For this setup a high power RF amplifier from Mini-Circuits was utilized that has 50 *dB* of gain with a -3 *dBm* maximum input. While a high power amplifier is needed to get the necessary voltage levels, it comes at the expense of a limited frequency range. The amplifier we found has a frequency range of 20 *MHz* – 1 *GHz*.

Considering a V_π voltage of 25 V and a $50\,\Omega$ electrode impedance, this gives an RF power of

$$P(W) = \frac{\left(\frac{V_{pk}}{\sqrt{2}}\right)^2}{R} = \frac{\left(\frac{25\ V}{\sqrt{2}}\right)^2}{50\ \Omega} = 6.25\ W \tag{72}$$

which when converted to *dBm* gives

$$P(dBm) = 10\log\left[\frac{P(W)}{1\ mW}\right] = 30 + 10\log\left[P(W)\right] = 37.95\ dBm\,. \tag{73}$$

Since the high power amplifier being used on this setup has a maximum output of 47 *dBm*, this voltage swing is achievable. Use of this high power amplifier also has the added benefit of being able to run the RF function generator at low power levels, where it can automatically level the output as the frequency is changed.

CHAPTER III

FABRICATION PROCESS DEVELOPMENT

A lot of work has gone into the development of the fabrication processes necessary for device fabrication. While previous work has developed a basic fabrication process [21], new processes and process improvements are necessary due to the push for lower losses and increased device functionality along with the acquisition of new equipment. As seen in Chapter II, small changes in the refractive index can have a large impact on the overall device performance. Hence, film thicknesses and waveguide dimensions have small tolerance. This chapter will focus on the developments made in improving the fabrication process. For a step-by-step procedure of the entire device fabrication process, please see Chapter IV and Appendix A.

Device tolerances can easily be observed by looking at the results from two samples that were processed side by side, seen in Fig. 35. Take two 21 x 42 *mm* substrates diced from the same 3" $LiNbO_3$ wafer, titanium thin film deposition done together in one deposition run with the samples side by side on the substrate holder, photolithography performed at the same time with identical exposure and developing parameters, etching performed with an identical recipe, and diffusion done together with the samples side by side on the substrate holder. To the best of our ability, these samples are identical, yet their Ti:$LiNbO_3$ waveguides have different responses. The TE mode is single mode in one device, while it is multi-moded in the other device.

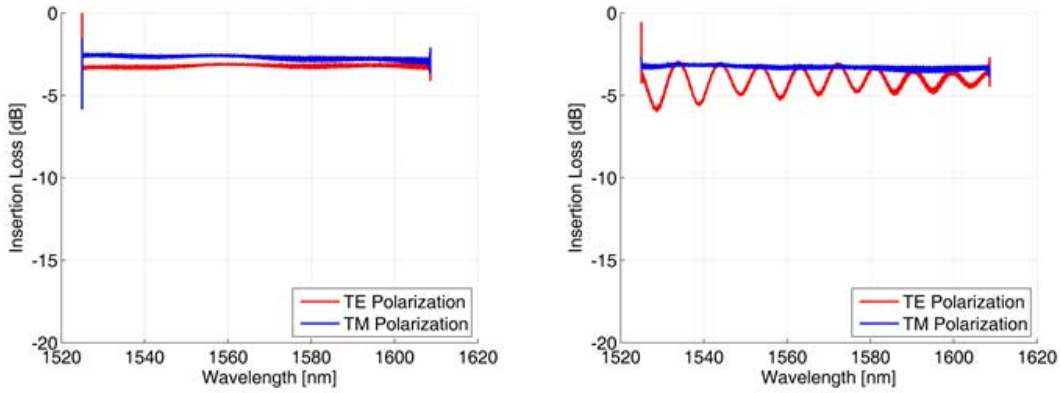

Fig. 35. Ti:$LiNbO_3$ waveguide response for "identically" processed samples.

There may be a slight variation in film coverage during deposition. Lithography and etching may have produced slightly difference waveguide profiles. The diffusion furnace may have a slight temperature gradient. As a result, two samples that were intended to be identical can have two different responses. This is why it is important to understand and optimize every step of the fabrication process, and aim to get repeatable results that give devices the best chance of working as expected from simulations.

A. Thin Film Deposition

One of the biggest improvements in our fabrication process came with the acquisition of a new DC/RF magnetron sputtering system from AJA International, Inc (referred to as the AJA system, or AJA, from this point forward). Previously we were using sputtering systems that had been built in-house and did not provide uniform film coverage, a one target DC/RF magnetron sputtering system (1T Mag) and a three target DC/RF magnetron sputtering system (3T Mag). Through the use of a rotating substrate

holder, along with angled sputtering guns, the AJA system allows for very uniform film coverage. It also has five sputtering guns and a load-lock, which minimizes the number of times the main chamber needs to be opened and allows for rapid throughput. Operating instructions for the AJA system can be found in Appendix B. Since this is a magnetron sputtering system, the sputtering guns have magnets imbedded in them as seen in Fig. 36 to create a magnetic field. The 2" diameter sputtering target is clamped over the cathode. The effects of these magnets will be mentioned later in this chapter.

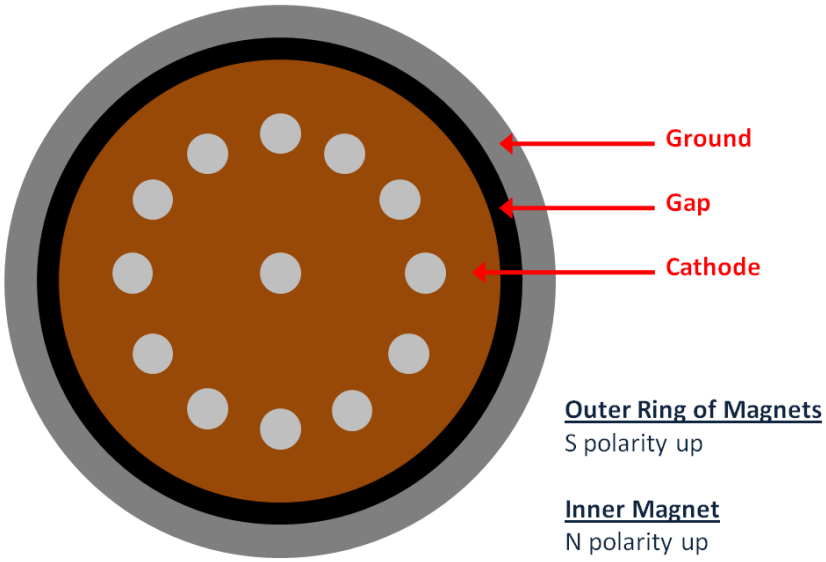

Fig. 36. Diagram of sputtering gun for AJA system.

One thing that our AJA system lacks is in-situ thickness monitoring, such as a crystal monitor. With multiple sputtering targets and a rotating substrate holder, there is no place in the chamber to place a monitor without causing shadowing on the substrate.

However, with computer control of flow rates, pressures, and power levels the deposition rates track very consistently between runs.

To compare the AJA system with our previous systems, an As_2S_3 thin film deposition on a 4" Si wafer was carried out in all three systems. The chalcogenide glass is measurable by spectral reflectance, and was measured using a Filmetrics F20 system. The thin film coverage can be seen in Fig. 37.

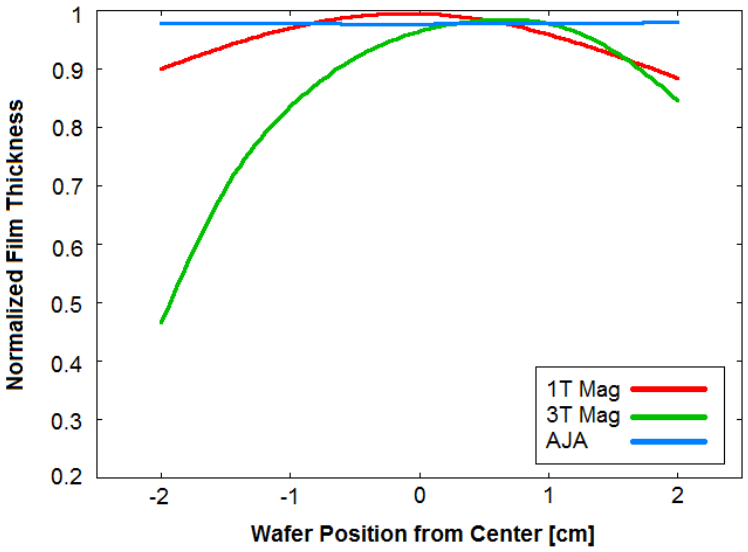

Fig. 37. Film uniformity measurement comparison for different DC/RF magnetron sputtering systems.

Since film deposition recipes are very much deposition system dependent, all recipes had to be redeveloped. Previous knowledge of materials that we had experience with and literature reviews for sputtering targets that were new to us gave a starting point for recipe development. In bringing up the AJA system, all film deposition recipes were optimized to < 2% thickness variation across a 4" substrate. Since the typical sample

size is 21 x 43 *mm* or smaller, the thickness variation should be even less across our substrate.

A.1. Titanium Thin Films

Titanium diffused waveguides on $LiNbO_3$ substrate are common in integrated optics. Due to the low coupling loss between Ti:$LiNbO_3$ diffused waveguides and single mode fiber , they provide an excellent way to couple laser light to/from the chip. Since Ti:$LiNbO_3$ waveguides are crucial to device operation, it is important to get quality film depositions. In addition to titanium film deposition, work was also done with previous Ph.D. candidates to achieve smooth waveguide surfaces after diffusion [21], which the quality of the deposition does have an impact on.

Because titanium is a metal, the film thickness cannot be measured by spectral reflectance. Hence, a surface profilometer is used to make thickness measurements, specifically a Dektak / IIa stylus profilometer. In order to make a measurement, there must be an actual step height to measure. In the interest of time it would nice to be able to make this measurement without having to perform lithography.

The first thought is to either use Kapton tape or another piece of substrate to cover a region of the sample. There are problems with these approaches in that they do not produce a clean edge; there will either be shadowing or peeling of the film when the tape is removed. Another possibility is to use a Sharpie® to mark a portion of the sample prior to the deposition, and then similar to lift-off remove it in acetone after the deposition. This method has actually proven to work extremely well. If the film does

not immediately come off while soaking in acetone, it is better to place the sample in a sonicator instead of rubbing the surface with a q-tip. Even a light touch with the q-tip where you do not think you are applying enough pressure to remove any film will give a noticeable reduction in measured film thickness. Table 6 shows the comparison between thin film measurements made with actual lithography and different Sharpie® techniques, where all samples were deposited in the same AJA run. While the measured thicknesses were similar, the ultra fine point Sharpie® showed better step profiles on the Dektak than the fine point Sharpie® and was also easier to remove during lift-off.

Table 6. Comparison of different Ti film measurement techniques.

	Lithography (lift-off)	Ultra Fine Point Sharpie® w/ q-tip	Ultra Fine Point Sharpie® w/ sonicator	Fine Point Sharpie®
Dektak	980 Å	952 Å	976 Å	973 Å

In developing the titanium deposition recipe, it was noted that the DC power level was crucial to getting a quality thin film. From previous deposition systems, it was already observed that a blue plasma was preferred to the purple plasma seen at lower power levels. Wet etching in diluted HF was also used as a quick gauge of the film quality. Even when the plasma was blue, if the power level was too low there was rippled etching under HF as seen in Fig. 38. It is believed this is due to grain boundaries of the deposited film, and a further increase in DC power alleviated this issue.

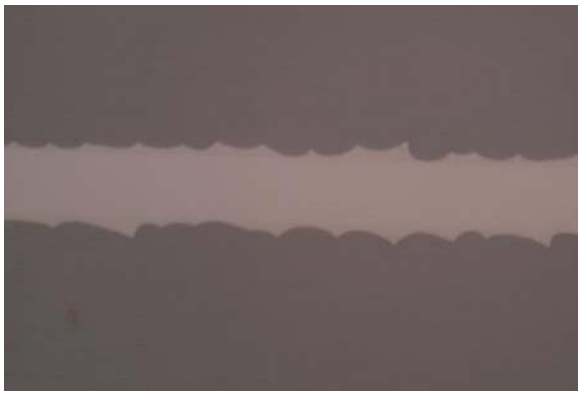

Fig. 38. Wet etching of titanium in diluted HF.

As the sputtering target is depleted there will be changes in its behavior, mainly observed through a decrease in the deposition rate for constant power as seen in Fig. 39. This decrease in deposition rate is expected. As the target is depleted, there is an increase in current due to there being a stronger magnetic field and a higher argon ion density [61]. It follows that for constant power, as the current is increased, there will be a corresponding decrease in the voltage. The deposition rate follows the trend of the voltage, which is fairly linear with sputtering time. There is roughly a 1:1 relationship (in terms of % change) between the current and the deposition rate.

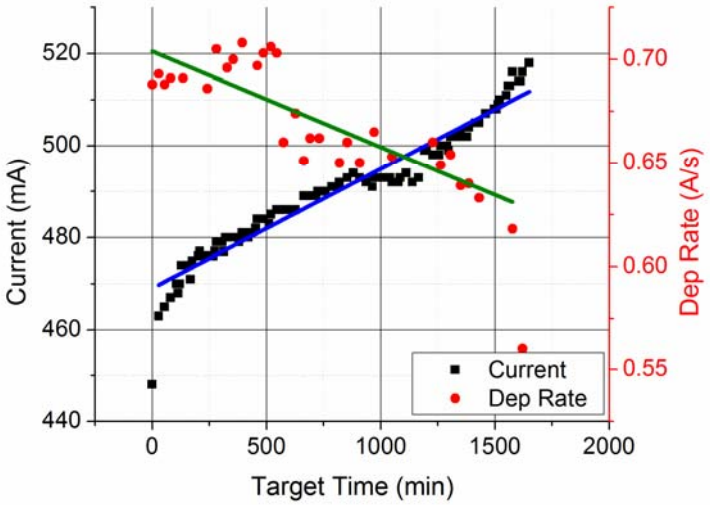

Fig. 39. Deposition parameter trend for Ti via DC magnetron sputtering.

It is also interesting to note that a race track indentation develops as the target is depleted as seen in Fig. 40, with the indentation forming where a majority of the plasma collisions are located due to the magnetic field from the magnetron gun [61]. Recall from Fig. 36 that there are magnets under the target, located in the sputtering gun cathode. As seen in Fig. 41, the magnetic field lines correspond to this target profile.

Fig. 40. Racetrack indentation on depleted metal target. Note that this is an Al target, but Ti targets show same behavior.

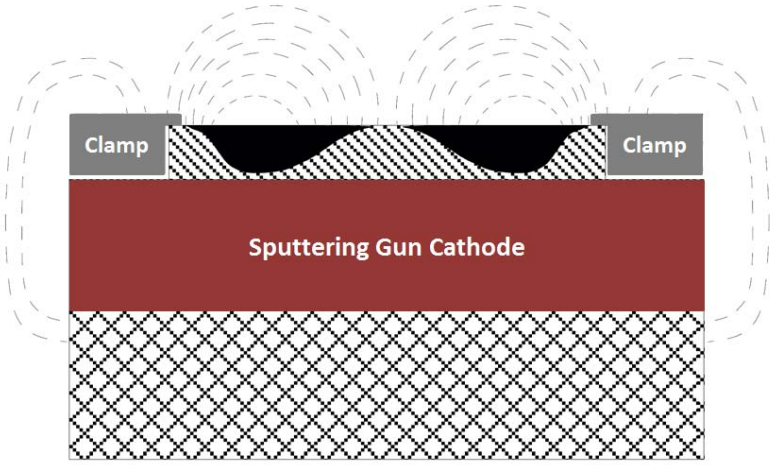

Fig. 41. Sputtering gun diagram, with magnetic field lines. Taken from [62].

After deposition of the titanium thin film, diffusion is carried out to drive the Ti into the $LiNbO_3$ substrate and form the waveguiding region. It was found that the surface gets smoother over the course of diffusion, and a wet diffusion atmosphere creates the lowest loss waveguides with smooth surfaces as seen in Fig. 42.

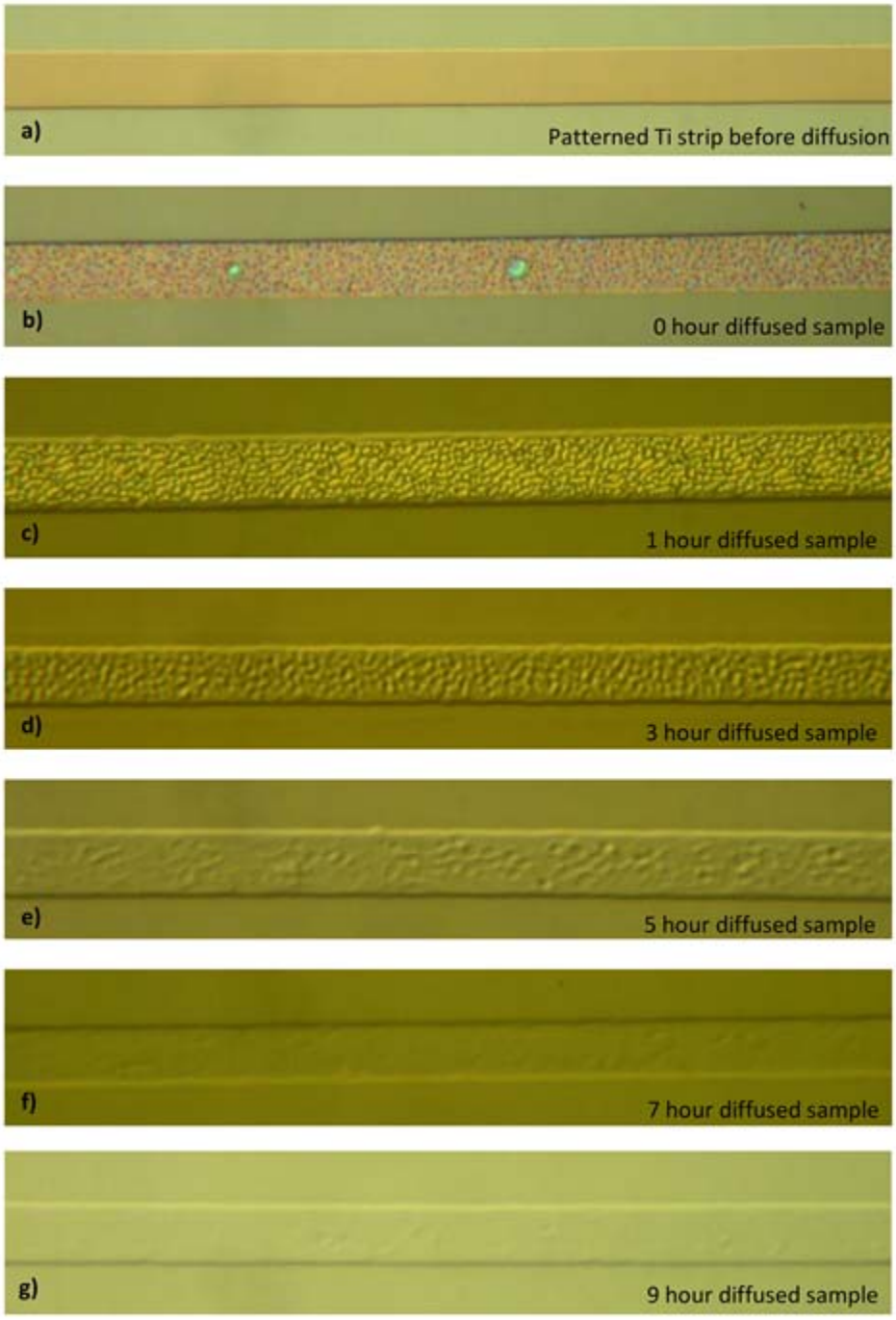

Fig. 42. Ti:$LiNbO_3$ diffused waveguide progression. Optical microscope shows (a) deposition through (b) furnace temperature ramp up, (c) 1 hr of diffusion at 1025°C, (d) 3 hr of diffusion, (e) 5 hr of diffusion, (f) 7 hr of diffusion, and (g) 9 hr of diffusion in a wet diffusion atmosphere. Taken from [21].

Flowing breathing air through a water bubbler is not enough to create a wet diffusion atmosphere. If the water is at room temperature it will still act as a dry diffusion. The water must be heated, not necessarily boiling, to introduce water vapor to the breathing air as it flows through the bubbler. We have used water temperatures around 70°C. The vapor content of the breathing air flowing into the furnace is a factor of both the water temperature and breathing air flow rate.

We did not measure the vapor content of the breathing air flowing into the furnace, but rather found that the gas inlet at the rear of the furnace provides a good measure of the vapor content. As seen in Fig. 43 it was found that a slight amount of condensation indicated the vapor content was adequate, and resulted in smooth waveguide surfaces. No condensation indicates the atmosphere is too dry, and large pooling of water indicates the atmosphere is too wet. The inlet tube was angled down slightly, so that gravity pulled the condensation away from the rear of the furnace.

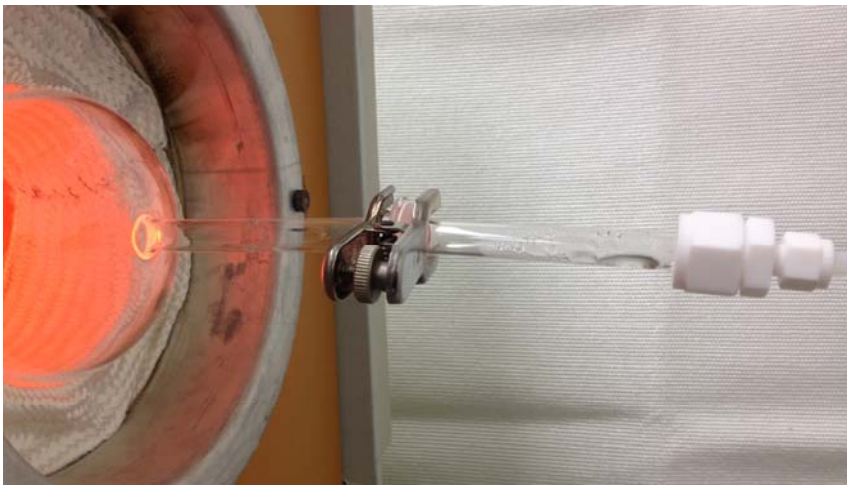

Fig. 43. Diffusion furnace air inlet, with visible condensation.

A.2. Silicon Dioxide Thin Films

Silicon dioxide (SiO_2) thin films are important both as a protective layer for our As_2S_3 films during lithography and as a cladding and buffer layer. Unlike metal targets which are conductive and can utilize DC magnetron sputtering, SiO_2 is an insulator and RF magnetron sputtering must be used to avoid charge buildup and arcing. In addition to flowing Ar gas into the deposition chamber to support the plasma, O_2 gas must also be introduced to the chamber for oxide films. Without any oxygen introduced during the deposition, the refractive index is significantly lower than bulk. As the percentage of oxygen in the gas mixture is increased the refractive index also increase, but at the expense of the deposition rate. It was found that a 5% oxygen flow (by flow rate) gives the best compromise between deposition rate and refractive index as seen in Table 7.

Table 7. SiO_2 deposition rate and refractive index for varying sputtering gas mixtures.

RF Power	Pressure	Ar Flow	O_2 Flow	Deposition Rate	Refractive Index @ 640 nm
175 W	3 mT	30 sccm	0 sccm	0.31 Å/s	1.44
200 W	3 mT	30 sccm	3 sccm	0.16 Å/s	1.46
200 W	3 mT	30 sccm	2 sccm	0.20 Å/s	1.48
200 W	3 mT	30 sccm	1.5 sccm	0.23 Å/s	1.48

Once again, as the sputtering target is depleted there will be changes in its behavior, mainly observed through a change in the deposition rate for constant power as seen in Fig. 44. However, the RF sputtering deposition rate trend is different than that for DC sputtering as it is immediately seen that the trend is not linear and follows a

quadratic trend line. Target depletion is also different and is more of a flat profile, as there is no formation of the race track indentation as seen with conductive metal targets. This is believed to be due to the fact that since the target is an insulator, the magnets in the sputtering gun do not magnetize the target.

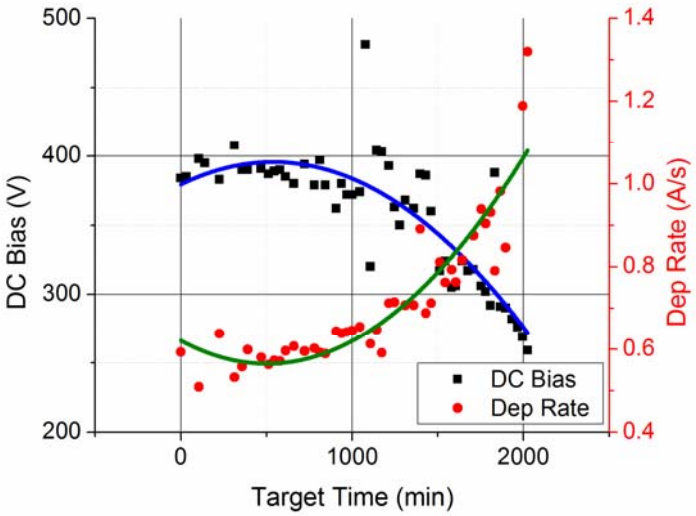

Fig. 44. Deposition parameter trend for SiO_2 via RF magnetron sputtering.

Recall that for AC one must look at RMS power, so constant power mode will be a constant RMS power. This is where the quadratic shape of the curve comes from. As seen with metal targets, as the deposition rate increases, the potential (voltage) also increases. The DC bias is a parameter of the power supply, and is the DC offset of the power supply. As the voltage (peak-to-peak amplitude) increases, the DC offset must decrease in order to maintain constant power, $P = V^2/R$. Unlike in the case of metal

targets with DC sputtering, the deposition rate for RF sputtering increases as the target is depleted. However, the deposition rate still tracks with the voltage as in the DC case.

Silicon dioxide thin films are typically annealed at high temperatures to further improve the film quality, giving an increase in the sheet resistance when measured with a four point probe. However, due to the temperature limitations of the As_2S_3 film, standard high temperature thermal annealing is not an option. Low temperature annealing was carried out at 130°C, but did not show a significant change in the sheet resistance of the SiO_2 film.

A.3. Arsenic Trisulfide Thin Films

One of the more difficult films to work with proved to be arsenic trisulfide (As_2S_3). Due to vapor pressure differences between arsenic and sulfur, it is hard to achieve exact As_2S_3 stoichiometry by thermal evaporation. Magnetron sputtering uses a high energy plasma to eject atoms from a sputtering target, and a magnetic field directs the ejected atoms towards the substrate. Using a bulk glass As_2S_3 target from Amorphous Materials Inc. we are able to deposit thin films with refractive indices very close to the bulk glass.

This chalcogenide glass has a low phase transition temperature of 180°C, which limits its upper use temperature to around 150°C. Due to this low temperature tolerance, deposition of As_2S_3 via RF magnetron sputtering requires special considerations. It is claimed that 75% of the power ends up heating the sputtering gun's cooling water, which means all that heat must first transfer through the target [63]. It immediately follows

that a low power plasma should be used, but a certain amount of power is required just to sustain a plasma. Additionally, if the deposition rate is too slow there is crystallization of the As_2S_3 film observed on the substrate surface. When an adequate deposition rate of 0.3 *Å/sec* was found to avoid crystallization, x-ray photoelectron spectroscopy (XPS) was used to confirm the thin film quality. The binding energy of the deposited As_2S_3 thin film matched the expected binding energy [64] and the qualification report also showed the expected mass concentrations.

However, with the 1/8" As_2S_3 target clamped to the backing plate with thermal paste between the target and the gun, the sputtering target was cracking within 15 minutes of deposition time due to thermal heat buildup. Due to this cracking, the power could not be increased to get a deposition rate faster than 0.3 *Å /s*. The cracking issue was alleviated by bonding the target to a molybdenum (Mo) backing plate. Target bonding has allowed for doubling the sputtering gun power, increasing the deposition rate to a more reasonable 0.5 – 0.8 *Å/s*. There is still gradual heat buildup over the course of a deposition run so the As_2S_3 target cannot be run for longer than 2 hours continuously without melting, still a drastic improvement over performance prior to target bonding.

Another concern is that As_2S_3 reacts with $(CH_3)_4NOH$ based developer solutions which are commonly used in photolithography. A protective layer of SiO_2 and Ti is deposited on top of the As_2S_3 to act as a buffer layer during the chalcogenide layer lithography. After etching the protective layer is removed by diluted HF acid, which As_2S_3 does not react with.

Just as with Ti and SiO_2, there is a change in the As_2S_3 sputtering target deposition rate as the target is depleted. However, because of the low power RF sputtering the trend is linear as seen in Fig. 45. Due to the low power, there is also no DC bias on the power supply. With the bonded targets, there is consistency observed between targets.

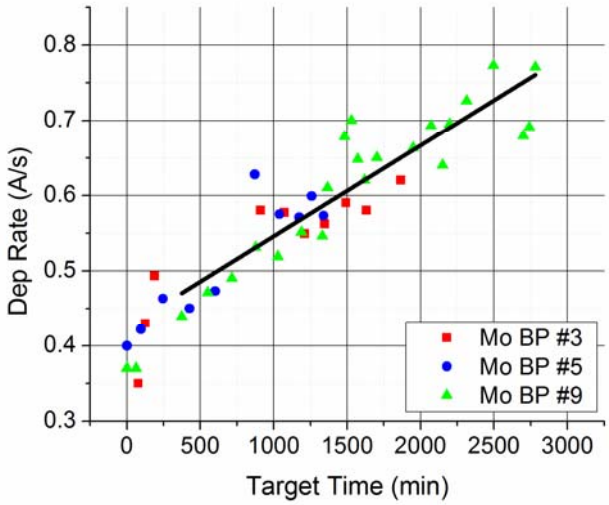

Fig. 45. Deposition parameter trend for As_2S_3 via RF magnetron sputtering.

Instead of going through and detailing the recipe development for every thin film that is used by our research group, the three main films that give an understanding of the system and had the most pressing issues were presented above.

After depositing blanket thin films on substrate, it is still necessary to pattern the desired features. Along with the ability to control the quality and thickness of the deposited film, the fabricated waveguide dimensions are also crucial device parameters.

B. Chalcogenide Fabrication

Recall from the previous chapter, mainly Table 4, that the As_2S_3 taper tip with is very crucial for mode coupling. Our fabricating capabilities are limited to contact lithography which has a resolution limit of approximately 1 μm; very close to the desired taper tip widths. Since mode coupling is required for device performance, the fabrication of 1 μm wide taper tip widths was a huge focal point. Extensive use of scanning electron microscopy (SEM) was used to image the taper tips, as the zoom ability under SEM is up to 1,000,000x, much larger than that of optical microscopes.

A JEOL JSM-7500F was utilized to obtain SEM images. SEM images a sample by emitting a beam of electrons from a cold cathode electrode gun, focusing the beam through a series of lenses and apertures, and then detecting the scattered signal off of the sample. Because of the use of an electron beam, a conductive sample is required. Unfortunately, $LiNbO_3$ substrate is not conductive. While there is a "gentle beam" mode that is aimed at reducing sample charging, my experience with it did not provide quality images.

It was found that the best way to image $LiNbO_3$ substrate samples was to place a grounding strip of Cu tape from the top edge of the sample to the sample holder as illustrated in Fig. 46, and on top of that sputter coat 3 – 4 *nm* of Pt/Pd. This provides a conductive path for the electrons, without covering up device features. The SEI detector was used with a 9 *kV* acceleration voltage for most imaging applications. Charge buildup was still noticed if high zoom was used in one location for a prolonged period of

time, but there is adequate time to find the feature of interest, focus the image, and take multiple pictures.

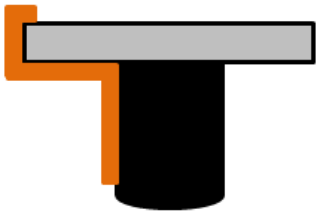

Fig. 46. Copper tape grounding strip for $LiNbO_3$ sample on SEM sample holder.

Since the SEM relies on electron scattering to obtain an image, the image it produces is different than an optical image. Titanium diffused waveguides, which are clearly visible under optical microscope, are difficult to see under SEM when they have a smooth surface (which we have optimized our fabrication processes for). On the other hand, As_2S_3 waveguides are clearly visible under SEM.

There are two aspects to consider with As_2S_3 waveguides, the waveguide width and the sidewall profile. The plasma etching recipe will determine the sidewall profile [65], and SEM imaging was used to analyze this profile. An angled sidewall will cause polarization conversion, while rough sidewalls can cause scattering losses. When tilting the substrate to obtain a picture of the sidewall etch profile, the acceleration voltage was increased to 15 *kV* and the LEI detector was utilized. We can see in Fig. 47 that the sidewall profile is smooth and measures 89.4°, which is close to the desired 90°.

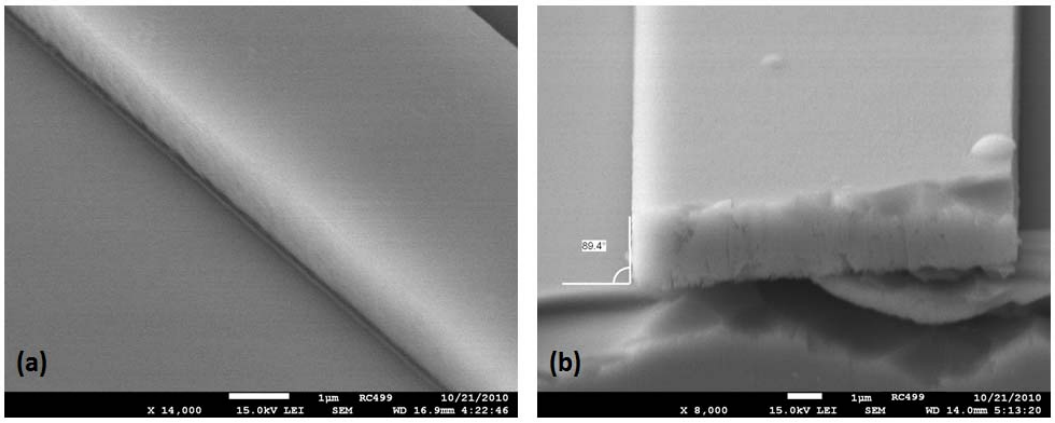

Fig. 47. SEM imaging showing As_2S_3 (a) sidewall roughness and (b) etching profile.

The As_2S_3 plasma etching gas flow for our Oxford RIE system is 5 *sccm* of Ar and 25 *sccm* of CHF_3 at 10 *mT* chamber pressure. While the Ar is only a small portion of this gas flow, the effects of it can be clearly seen when looking at etch profiles under SEM. As seen in Fig. 48, the sidewall is significantly rougher when only CHF_3 is used during plasma etching.

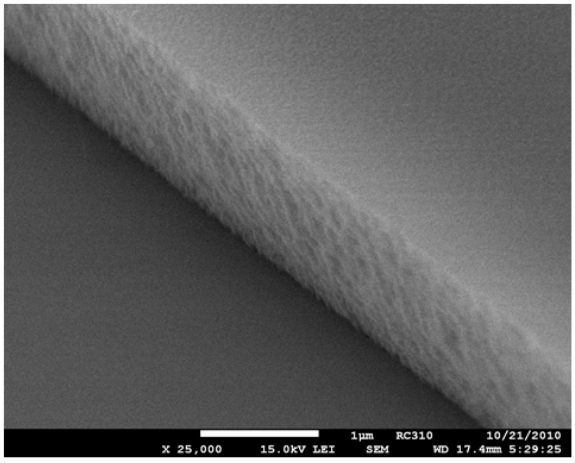

Fig. 48. As_2S_3 waveguide sidewall with CHF_3 only during plasma etching.

In addition to the sidewall profile, SEM imaging was also used to analyze taper tip widths. We were having issues fabricating 1 μm wide taper tips, and had been sending samples out to get processed off-site with a stepper lithography system. After asking AZ Electronic Materials for information on their 5214-EIR photoresist and MF-312 photoresist developer and looking through it [66], while we were meeting the minimum exposure dose it appeared that feature resolution may be improved with even higher exposure doses. A lithography experiment was carried out, and the SEM was utilized to analyze the samples. The SEM images for varying exposure doses can be seen in Fig. 49. Note that on the lithography mask the taper tip width is 0.8 μm.

It can be seen in Fig. 49 that as the exposure dose is increased, the claw shaped taper tip becomes more rounded and the width gets narrower. The dose of 95 mJ/cm^2 gives the ideal taper tip that we desire. We expect slight swelling in width due to photoresist reflow during the hard bake process. With implementation of the improved fabrication procedure and an exposure dose of 95 mJ/cm^2 during lithography, samples were fabricated with excellent coupling tapers as seen in Fig. 50.

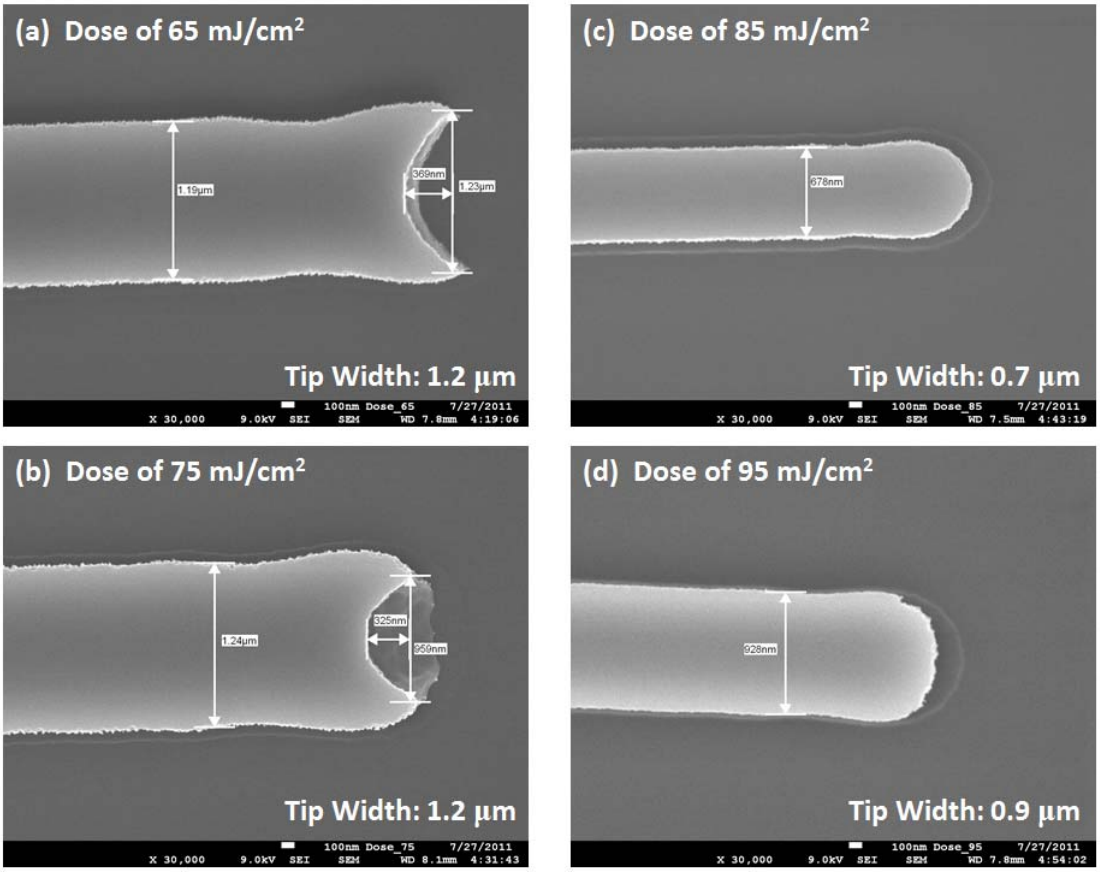

Fig. 49. Effect of lithography dose on As_2S_3 taper tip width for (a) 65, (b) 75, (c) 85, and (d) 95 mJ/cm^2.

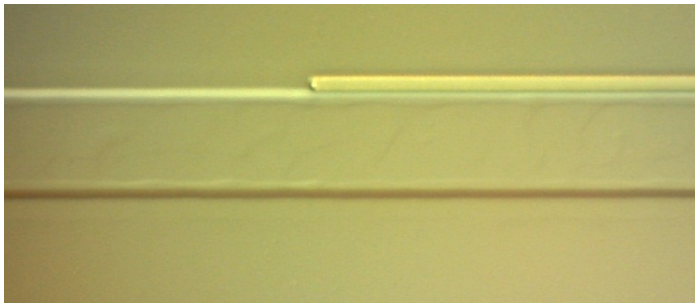

Fig. 50. Coupling region taper on fabricated sample.

Since we are using contact lithography, where the mask is in direct contact with the sample, mask cleanliness also becomes a major issue. Once again, while the waveguides may look good under optical microscope, the defects caused by a dirty mask are clearly visible under SEM and can be seen in Fig. 51.

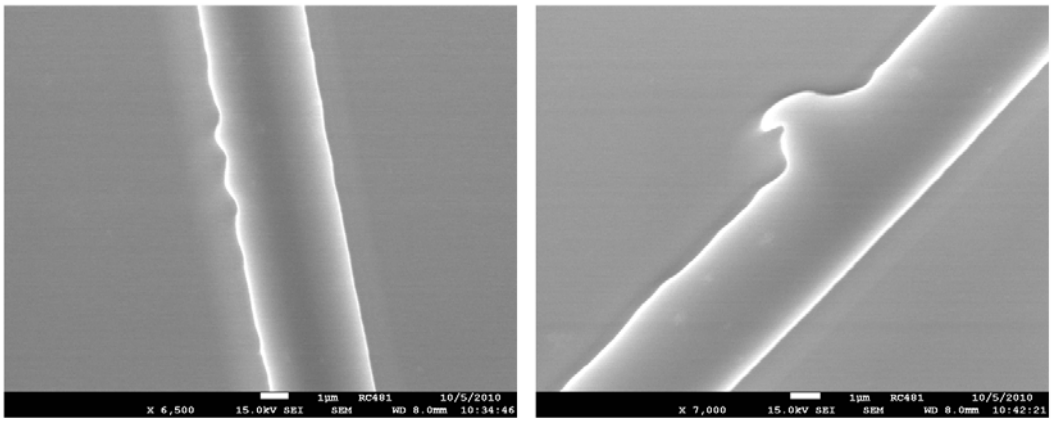

Fig. 51. Waveguide defects due to a dirty mask observed under SEM.

It was found that the best way to keep the lithography mask clean was to place it in heated photoresist stripper after every use. For older mask that already had extensive photoresist buildup on them, it was harder to remove the old photoresist. We place our 6" x 6" lithography mask in an 8" x 8" Pyrex dish, chrome side down. A 1" x 1" piece of $\frac{1}{8}$" thick Teflon is placed under one corner of the mask to keep it elevated and off of the bottom of the dish. At first a piece of Teflon was placed under each corner of the mask, but the pieces began to move around when the photoresist stripper was heated up and it was feared that they would scratch the chrome pattern. The dish is filled with AZ-300T photoresist stripper until the mask is covered and placed on a hot plate. A

thermometer is used to measure the photoresist temperature, and it is heated to 90°C. This temperature is held for 15 minutes, then the dish is removed from heat and allowed to cool down to room temperature for several hours. The mask is then rinsed well under DI water and blown dry with a N_2 gun. After implementing this procedure, especially from the onset with new lithography masks, a reduction in waveguide defects was observed.

C. Electrode Fabrication

In order to test electrode fabrication procedures, polarization converters were first fabricated on Ti:$LiNbO_3$ diffused waveguides since they are simple to fabricate and do not require an As_2S_3 waveguide to easily observe their performance. Since it was known that As_2S_3 would eventually be used, the processing temperature limit for As_2S_3 was kept in mind. The choice of material for a cladding/buffer layer is not limited to SiO_2. Silicon nitride (Si_3N_4) is also used as a common cladding/buffer material and it was also experimented with.

As a first test, the electrode performance was compared between SiO_2 and Si_3N_4 thin films deposited with and without substrate heating (120°C) during cladding/buffer layer deposition. The films were not annealed after deposition. In both cases the ambient deposition showed lower conversion voltages, with the SiO_2 conversion voltage half of the Si_3N_4 conversion voltage. This voltage difference is expected since the dielectric constant for Si_3N_4 is roughly twice that of SiO_2, and the electric field magnitude is inversely proportional to the permittivity of the dielectric buffer. The

Si_3N_4 film showed issues with internal film stresses, and despite much manipulation of the deposition recipe there was peeling of the Si_3N_4 film when placed in solvent. Solvent cleaning is a common process in device fabrication, and loss of adhesion of the cladding/buffer layer also results in the electrodes fabricated on top of it to be removed from the sample as seen in Fig. 52. As a result of these experiments, SiO_2 was chosen as the cladding/buffer layer material.

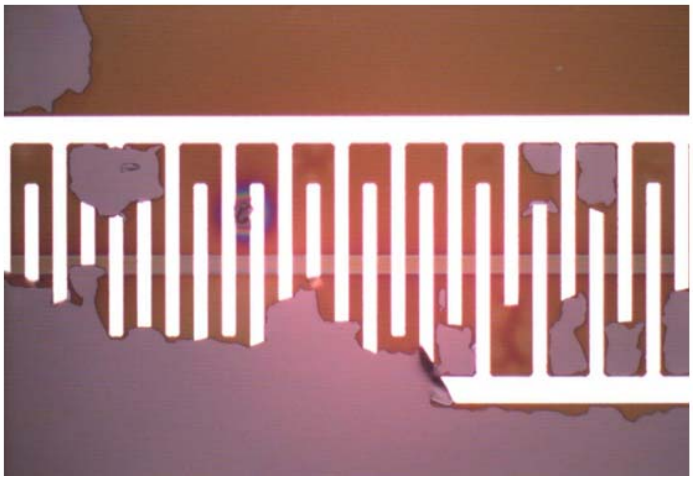

Fig. 52. Peeling of Si_3N_4 layer, resulting in loss of electrodes.

As a second test, a pico-ammeter was used in the electrode path to measure the leakage current. The polarization converter electrodes are electrically isolated with a 5 μm gap. With 20 V applied to the electrodes, a 5 – 10 nA leakage current was observed on a SiO_2 film deposited at ambient temperature with no annealing after deposition. Testing of a high temperature annealed SiO_2 film did not give a measurable leakage current, though this annealing step would cause issues with an As_2S_3 film. While the

SiO_2 film quality could be improved with a high temperature anneal, the small leakage current suggest we can achieve adequate performance from an un-annealed film and a larger electrode gap.

Recall from the previous section that a protective layer is deposited on top of the As_2S_3 thin film to protect it from $(CH_3)_4NOH$ based developer solutions during photolithography. Just as the As_2S_3 film needs to be protected during lithography to pattern those features, it also needs to be protected afterwards during lithography of the electrodes. While a thick SiO_2 buffer layer is required if there is going to be overlap between the waveguides and electrodes, there is no need for a buffer layer if the waveguide will be between the electrodes. However, Al by itself did not provide adequate protection for the As_2S_3 features during electrode lithography as seen in Fig. 53. This necessitates the use of a SiO_2 cladding/buffer layer to provide protection for the As_2S_3 features.

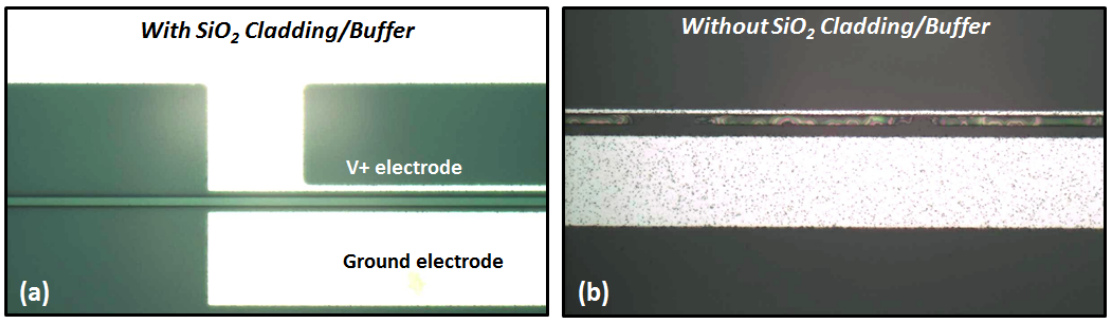

Fig. 53. Protection of As_2S_3 features during electrode lithography (a) with and (b) without the use of a SiO_2 cladding/buffer layer.

With the use of a buffer layer necessitated by the As_2S_3 material, the mode confinement and tuning strength concerns mentioned in the last chapter come into consideration when choosing a film thickness. A 100 *nm* thick SiO_2 layer provided hit and miss performance as a protective layer. Increasing the layer thickness to ~150 *nm* provided better protection, while still giving good As_2S_3 waveguide measurements.

Taking all of the above into consideration, an electro-optically tunable As_2S_3 on Ti:$LiNbO_3$ device was successfully fabricated and tested. Device fabrication details and results from testing can be found in the following chapter.

CHAPTER IV

ELECTRO-OPTIC TUNING RESULTS AND ANALYSIS

This chapter will look at the final realization of electro-optically tunable As_2S_3 on Ti:$LiNbO_3$ interferometers and ring resonators. The electro-optic tuning will be looked at on both a DC and AC level, with the DC performance used to find electro-optic tuning parameters and the AC performance used to find the maximum modulation frequency.

A. Device Fabrication

All samples are fabricated on x-cut y-propagating $LiNbO_3$ substrate. We purchase 3" $LiNbO_3$ wafers from Crystal Technology LLC, and then use a dicing saw to get multiple samples from each wafer. After dicing the samples are cleaned with soapy water and solvents. The solvent rinse order is acetone, methanol, and then a final rinse with isopropyl alcohol (IPA).

Having a clean substrate, the samples are loaded into the AJA where a 95 *nm* thick Ti film is deposited on the substrate and patterned into 7 μm wide Ti strips for bus waveguides utilizing contact photolithography with positive photoresist and plasma etching in an Ar/CHF_3 atmosphere. Heated photoresist stripper is then used to remove the photoresist, and the strips are diffused into the $LiNbO_3$ substrate for 10 hours at 1035°C in a wet breathing air atmosphere.

After the Ti:$LiNbO_3$ waveguides are diffused, the facet edges are polished to optical quality so that there are not additional diffraction losses when butt coupling from the optical fiber into the device. As seen in Fig. 54, even with a 15 μm grit polishing pad there are numerous defects that will promote diffraction. The samples are quickly tested on the LUNA to confirm their insertion losses. Typical Ti:$LiNbO_3$ devices show approximately 1.5 *dB/cm* of insertion loss, with the TM mode showing slightly less loss that the TE mode. In the case of Fig. 54 there was a 5 *dB* increase in optical losses for the sample only polished with the 15 μm pad on one facet edge.

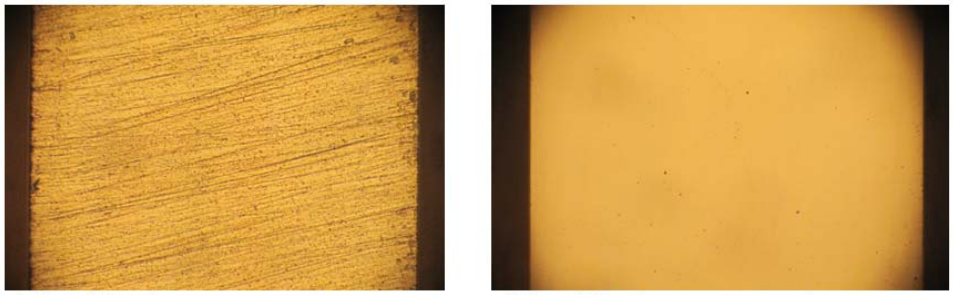

Fig. 54. Sample facet edge quality after polishing. Polishing with (a) 15 µm and (b) 0.5 µm grit pads.

With satisfactory Ti:$LiNbO_3$ bus waveguides, the samples are solvent cleaned again and then loaded into the AJA where a 475 *nm* thick As_2S_3 chalcogenide thin film is deposited on the substrate with a SiO_2+Ti protective layer. Contact photolithography with positive photoresist and plasma etching in an Ar/CHF_3 atmosphere are used once again to form 3.5 μm wide waveguides with 0.8 μm to 1.6 μm coupling tapers to couple the mode out of the Ti:$LiNbO_3$ diffused waveguide. Oxygen plasma ashing and

acetone are used to remove the photoresist, as photoresist stripper is also $(CH_3)_4NOH$ based and would remove the patterned As_2S_3 features. The protective layer is then removed in diluted HF acid, which does not react with the As_2S_3 film layer.

A 138 *nm* thick SiO_2 protective cladding/buffer layer is then deposited on the patterned As_2S_3 devices. This is followed with a 500 *nm* thick Al layer that is patterned by contact lithography and wet etching to form the electrodes. Once the electrodes are formed, the device is complete and ready for electro-optic testing. Complete fabrication details with step-by-step processing instructions can be found in Appendix A.

B. Interferometers

The interferometer is a much more robust device to fabricate when compared to the ring resonator, so it follows that the interferometer would be the best way to initially test the electrode performance. I quickly realized this when I initially went for broke with a lithography mask design that consisted entirely of ring resonators with various design iterations. With no working devices, I included a mix of test structures on the next lithography mask design. On the interferometer structure, electrodes were placed in the path length of the interferometer. The overall device structure for the interferometer can be seen in Fig. 55.

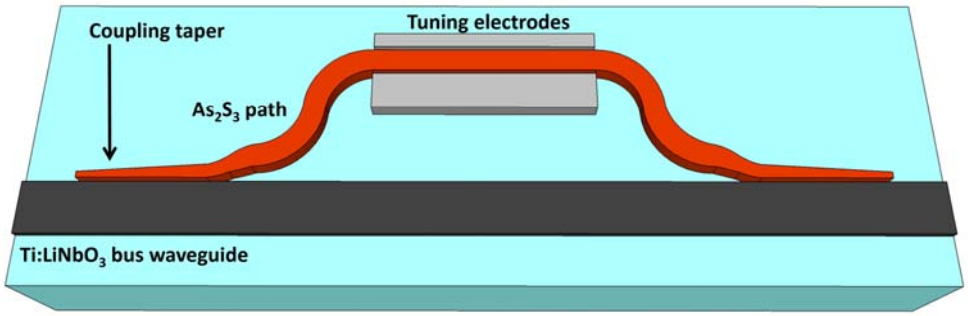

Fig. 55. Overall device structure of electro-optically tunable MZI with As_2S_3 rib waveguide side coupled to $Ti:LiNbO_3$ diffused waveguide.

Recall it was mentioned that overlap of the electrodes with the As_2S_3 waveguide will cause optical mode absorption. Due to the use of contact lithography, several samples were fabricated where misalignment caused there to be slight overlap between the edge of the Al electrodes and As_2S_3 waveguide. This can easily be seen with an interferometer, where the optical mode from each branch can be isolated and looked at separately as in Fig. 56.

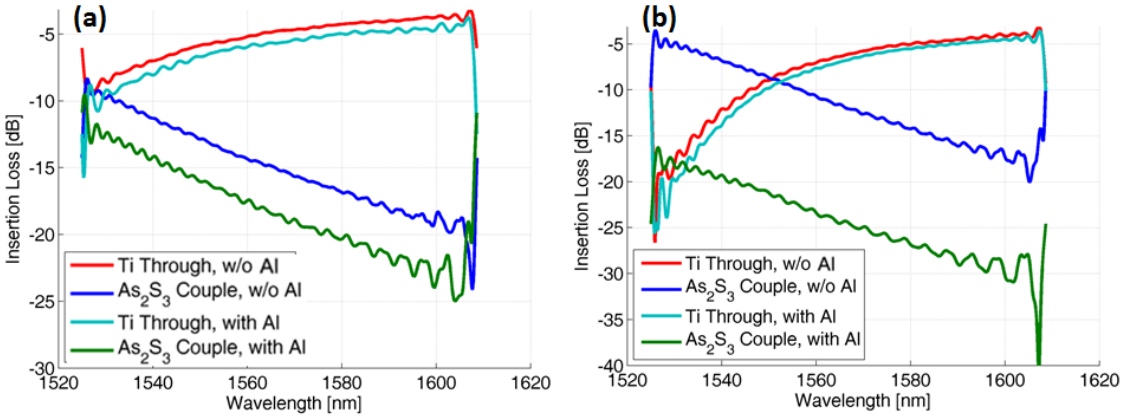

Fig. 56. Comparison of insertion losses for each branch of interferometer for (a) 0.2 µm and (b) 0.8 µm electrode overlap.

These samples did have a 150 *nm* SiO_2 buffer layer, but it can be seen this is not enough to prevent mode absorption. As more of the waveguide is overlapped, there is an increase in optical losses due to mode absorption. Recall that the As_2S_3 waveguide is 3.5 μm wide, so the 0.8 μm overlap in Fig. 56(b) does not even come close to covering the entire waveguide. Complete overlap of the As_2S_3 waveguide would be required for TM polarization tuning with r_{33}, and was observed to result in 100% mode absorption.

To test tuning of the coupling region, an s-bend structure was utilized as seen in Fig. 57. The tapers are identical to those used in the interferometer, with the only difference being that after propagating through the As_2S_3 path length the light is coupled into a second Ti:$LiNbO_3$ waveguide, not the same Ti:$LiNbO_3$ waveguide. This results in there being no interference pattern observed at the output, but it does allow for the through and cross ports to be analyzed separately.

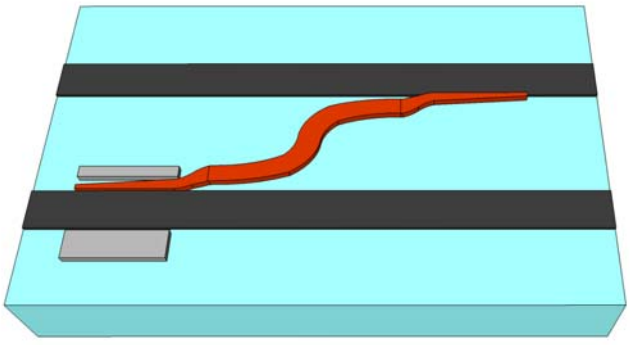

Fig. 57. Overall device structure for coupling region tuning with an s-bend.

B.1. Path Length Tuning

Recall from Chapter II that electrodes placed in the As_2S_3 path will change the optical path length of the interferometer, resulting in a change in the interference pattern at the output. Specifically, it will show a spectral shift in the response. Results will be shown for two interferometers, one with a 7 μm gap and the other with a 5.4 μm gap. Based on the desired gap to width ratio, the signal electrodes are 4 μm and 3 μm wide, respectively. The ground electrode was made 80 μm in all cases. All electrodes had 275 x 275 μm contact pads, and were 7,000 μm in length.

Once fabricated, the magnitude response of the tunable interferometer was measured using the LUNA OVA and DC electrode probes. The electro-optically shifted response for the 7 μm electrode gap can be seen in Fig. 58.

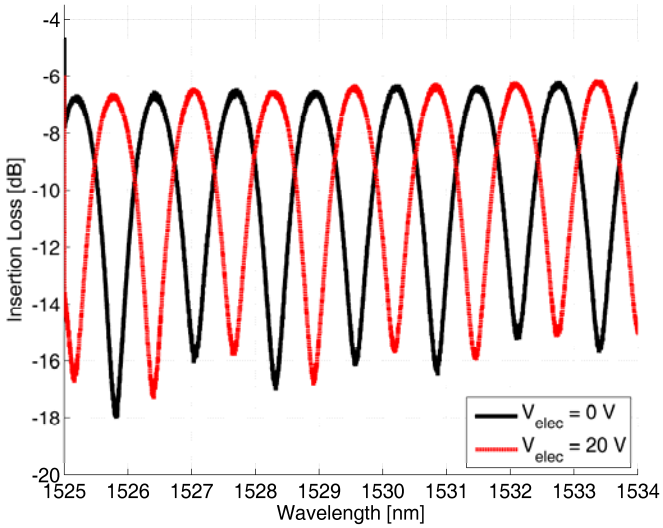

Fig. 58. Wavelength response for MZI as DC voltage is applied to electrodes.

The FSR of this interferometer response is measured to be 1.3 *nm*. Recall from (53) that the electro-optically induced index change causes a phase shift to be observed at the MZI output. The V_π voltage is the required voltage to obtain a π phase shift, or to shift the FSR by half of its width. For 1530 *nm* operation, a 0.77 μm change in the As_2S_3 optical path length is required to obtain this phase shift.

To determine the V_π voltage, the DC voltage was swept and the FSR shift recorded. The measured data, with a linear fit, can be seen in Fig. 59. The data was fit with a linear trend line having $R^2 = 0.989$ and showed a tuning rate of 0.028 *nm/V* at 1530 *nm*. From this it follows that V_π is 22.7 *V* at 1530 *nm*. Because the V_π voltage depends on the electrode length, a useful figure of merit is actually the voltage-length product. With 7 *mm* long electrodes, the voltage-length product at 1530 *nm* is 15.9 *V-cm*.

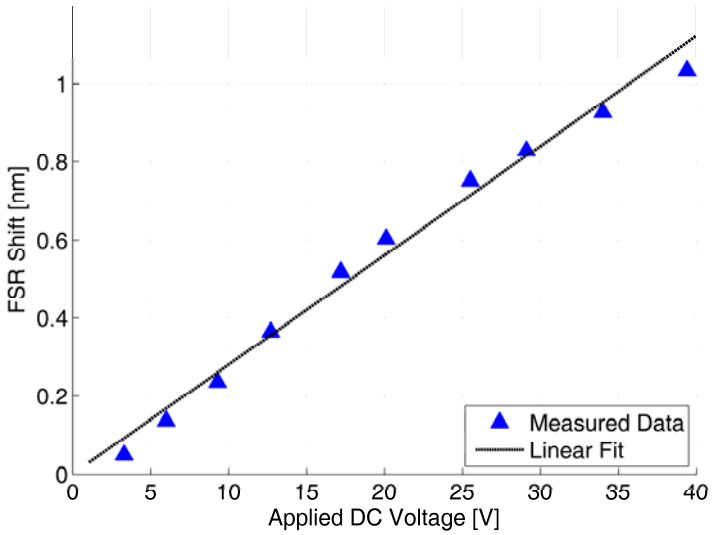

Fig. 59. Measured interferometer FSR shift with sweep of electrode DC voltage.

Looking at (68), the voltage required for tuning can be reduced by either increasing the field overlap or increasing the electric field strength. The electric field strength can be increased by reducing the electrode gap. The same testing procedure was carried out on the device with the electrode gap of 5.4 μm, and a comparison of the results can be seen in Table 8.

Table 8. Interferometer path length tuning.

Electrode Gap	Tuning Rate	V_π	$V_\pi L$
7 μm	0.028 nm/V	22.7 V	15.9 V-cm
5.4 μm	0.032 nm/V	20.3 V	14.2 V-cm

By using (68) the overlap factor between the approximate optical and electrical field can be determined. This is an approximation since the strength of the electrical field is only roughly calculated by the ACPS gap spacing and applied voltage. Note that because this is not the ideal tuning case, with the TM polarization being utilized on an x-cut substrate with r_{13} instead of r_{33}, the equation becomes

$$\Gamma_o \approx \frac{\lambda g}{\left(V_\pi \ell_t\right) n_o^3 r_{13}}. \tag{74}$$

For the cases in Table 8, the overlap factor is calculated and shown in Table 9.

Table 9. Approximate electrical/optical field overlap (Γ_o)

Electrode Gap	$V_\pi L$	Γ_o
7 μm	15.9 V-cm	63.4%
5.4 μm	14.2 V-cm	54.8%

While these overlap factors are low when compared to electro-optically tunable diffused Ti:$LiNbO_3$ waveguides, recall that the optical mode has ~ 50% mode confinement in the As_2S_3 rib waveguide (Fig. 18) which does not have electro-optic tuning capabilities. Any overlap between the electric and optical fields is going to take place in the substrate. Hence, there is significant overlap between the electrical field and the optical mode that "leaks" into the $LiNbO_3$ substrate. This is due to the mode in the $LiNbO_3$ is close to the surface, and the thin film electrodes having a shallow electric field that also lies close to the surface.

B.2. Coupling Region Tuning

With electrodes in the coupling region, tuning of the coupling percentage was not observed on the s-bend structure. Coupling tapers were made both as a normal taper, and with a 1000 μm length of 0.8 μm wide As_2S_3 added to the front of the taper to mimic the phase shifting region between the tapers of the ring resonator. However, unlike in the ring case which will be shown in the next section, there was no coupling region tuning observed.

This is believed to be due to the lack of feedback in an interferometer, thus resulting in the tapers not being back to back. As shown in Fig. 24, coupling tuning is

believed to occur due to a phase shift created between the back to back tapers. There is no such phase shifting region in an interferometer.

B.3. Electrode Modulation

While DC measurements show that there is electro-optic tuning with a change in refractive index, for switch and waveform generation applications modulation is required. The tuning path electrodes of the interferometer were tested with the modulated electrode setup described earlier. The frequency of the RF function generator was swept, and the peak-to-peak amplitude of the photodetector signal was recorded off of the oscilloscope. The normalized peak-to-peak amplitudes versus frequency can be seen in Fig. 60.

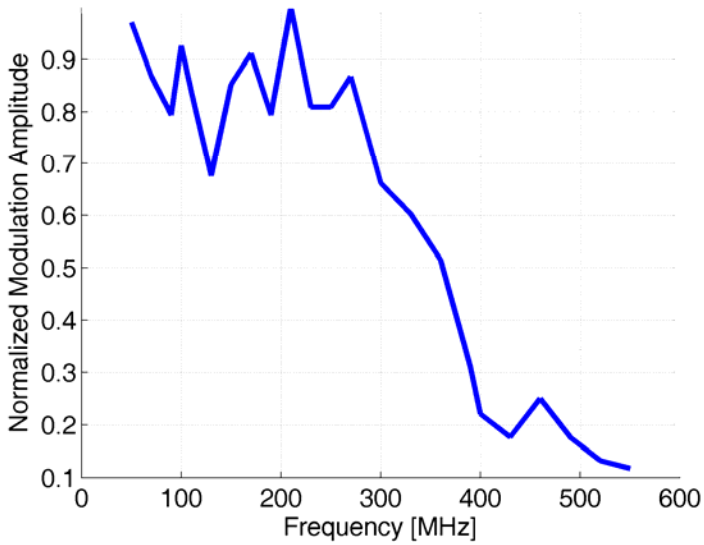

Fig. 60. Modulated electrode electro-optic tuning results.

The maximum modulation rate is determined by the 3 *dB* point, or the frequency at which the amplitude swing is reduced by half. While there was noise present in the measurement setup, there was a clear reduction in amplitude swing around 300 – 400 *MHz*, with the 3 *dB* point occurring around 350 *MHz*. This is smaller than the *GHz* performance that we were hoping to be able to achieve, but gives the 100 *MHz* modulation that has been previously show for frequency chirped waveform generation.

The low modulation frequency can be attributed to several factors. For starters, the electrodes were only designed for impedance matching, not velocity matching. Thin film electrodes were used rather than thick film electrodes. Also, without annealing of the SiO_2 buffer layer, recall that there is a weak, but measurable, leakage current. While improvements in all three of these aspects would help achieve GHz modulation rates, 100 *MHz* modulation is enough to achieve waveform generation of interest [58].

C. Ring Resonators

While interferometers are the more robust structure to fabricate, ring resonators provide desired functionality and are the more interesting test structure. However, several samples were fabricated over the course of this work where the interferometers on the device showed excellent results and the ring resonators were sub-par. Coupling into the ring resonator is more sensitive to changes in the refractive index, as observed by tuning of the coupling region.

For a 5 *GHz* ring, the physical path length of the ring needs to be 27 *mm*. To minimize bending losses, a bending radius of 400 μm is used. With this radius, it leaves

a remaining 24.5 *mm* to be split between the top and bottom of the ring, i.e. 12.25 *mm* for each. This means that the top tuning path of the ring can be 12,000 μm long while there is also 12,000 μm of length for the coupling region. With 2,500 μm long tapers, this leaves a gap of 7,250 μm between the two tapers that can either be connected with a thin As_2S_3 strip or left gapped.

Recall from (55) that the ring resonator response is a function of both the coupling percentage and the round trip loss. We have developed Matlab code in our group that performs curve fitting on the measured insertion loss (magnitude) and group delay (phase) information from the ring response and extracts both the coupling percentage and the round trip loss, as seen in Fig. 61.

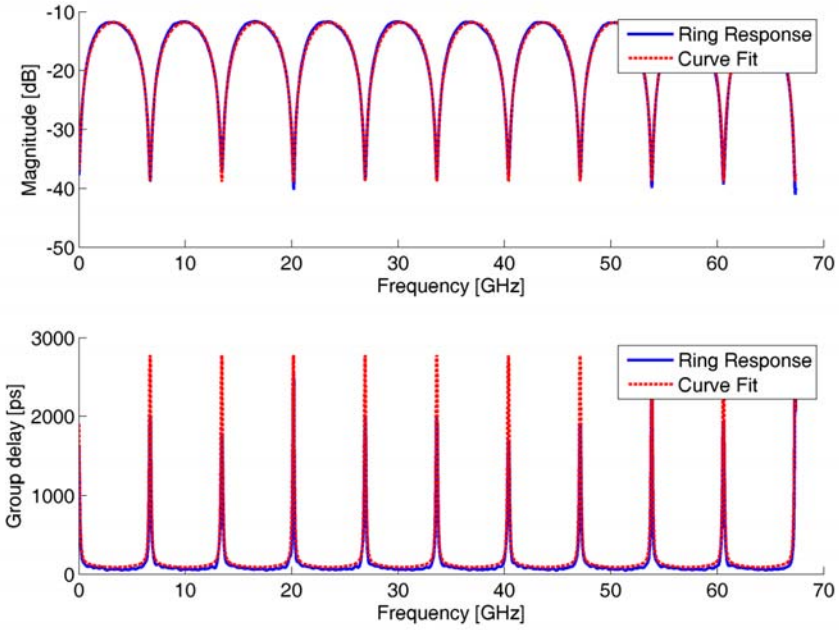

Fig. 61. Curve fitting to extract coupling and round trip loss. Shown is RC740, Ring 5, at 1540 nm (κ = 91.9%, αL = 10.27 dB).

Over the course of device fabrication in our academic setting, especially with contact lithography, odds are that no two devices will be identical. As a result, devices will be observed with a wide range of ring parameters. A collection of some of the rings encountered over the course of this work can be seen in Table 10.

Table 10. Ring parameters for fabricated devices.

Device	Coupling	Round Trip Loss
Published Lowest Loss Device [47]	41%	1.2 dB/cm
RC505, Ring 4	56%	1.6 dB/cm
RC728, Ring 10	58%	3.8 dB/cm
RC697, Ring 9	73%	2.0 dB/cm
RC506, Ring 2	73%	2.7 dB/cm
RC740, Ring 15	74%	2.4 dB/cm
RC697, Ring 10	77%	2.8 dB/cm
RC740, Ring 5	92%	4.2 dB/cm

It can be seen from Table 10 that for a few exceptions, there is a general trend between coupling percentage and round trip loss; as the coupling percentage increases, the round trip loss also increases. This is believed to be due to the Ti:$LiNbO_3$ diffused waveguides, and the surface bump that is created by diffusion. For diffusion in a wet atmosphere, where the lowest optical losses and smoothest waveguide surfaces are observed, the post-diffusion bump can be up to twice the deposited film thickness. An AFM image showing this bump in seen in Fig. 62 [21].

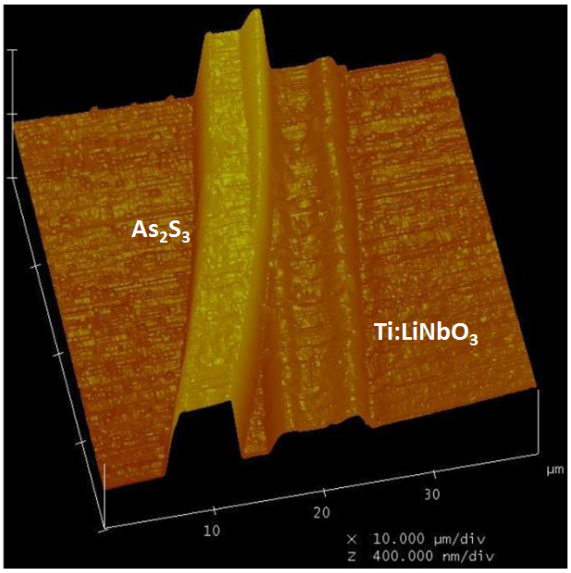

Fig. 62. AFM image showing impact of diffusion surface bump on As_2S_3 waveguide. Taken from [21].

The strongest coupling is going to be observed when the As_2S_3 tapers are closer to the $Ti:LiNbO_3$ diffused waveguide, and/or with longer taper lengths. When overlap begins to occur, while this helps the coupling, the waveguide defect will increase the optical mode losses. The longer tapers also increase the interaction length with the surface bump.

For ring resonator devices, electrodes were placed both in the path length and the coupling region, as shown in Fig. 25. Actual fabricated electrodes in these two regions can be seen below in Fig. 63. Note that the coupling region electrodes have a larger gap, because overlap is avoided both with the As_2S_3 waveguide and the $Ti:LiNbO_3$ waveguide.

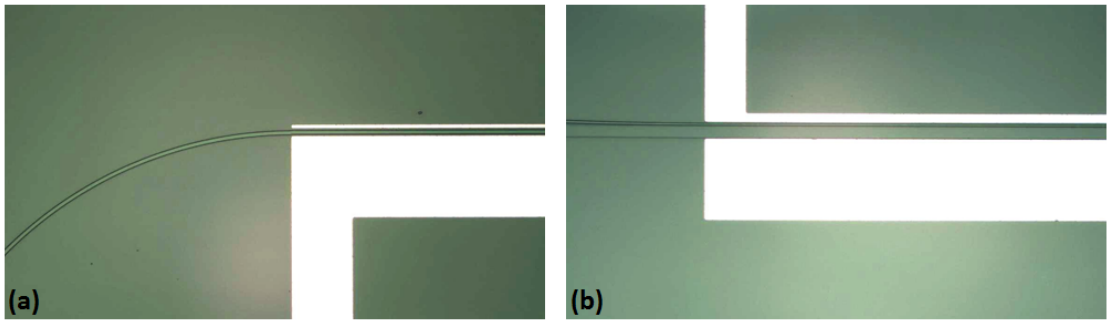

Fig. 63. Tuning electrodes in the (a) ring path and (b) coupling region.

C.1. Path Length Tuning

Path length tuning is identical between the interferometer and the ring. The 3.5 μm wide As_2S_3 waveguide is centered between the ACPS electrodes. Once again, the LUNA OVA with DC electrode probes was used to apply a voltage to the electrodes and the FSR shift was observed. For a 5 *GHz* ring resonator, the FSR is measured to be 0.04 nm. We require a 0.35 μm change in the optical path length is for a π phase shift, which is less than the optical path length shift required for the interferometer due to the ring resonance. The spectral shift can be seen in Fig. 64, while the measured FSR shift for a swept voltage can be seen in Fig. 65.

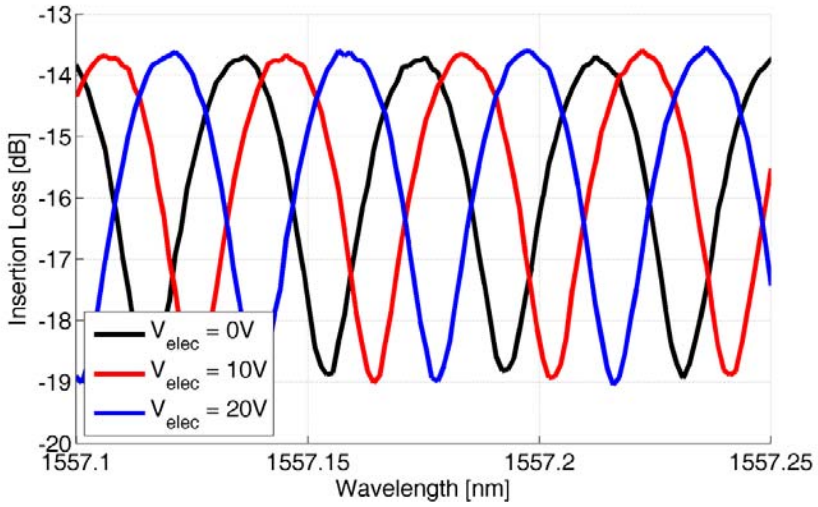

Fig. 64. Wavelength response for ring resonator as DC voltage is applied to electrodes.

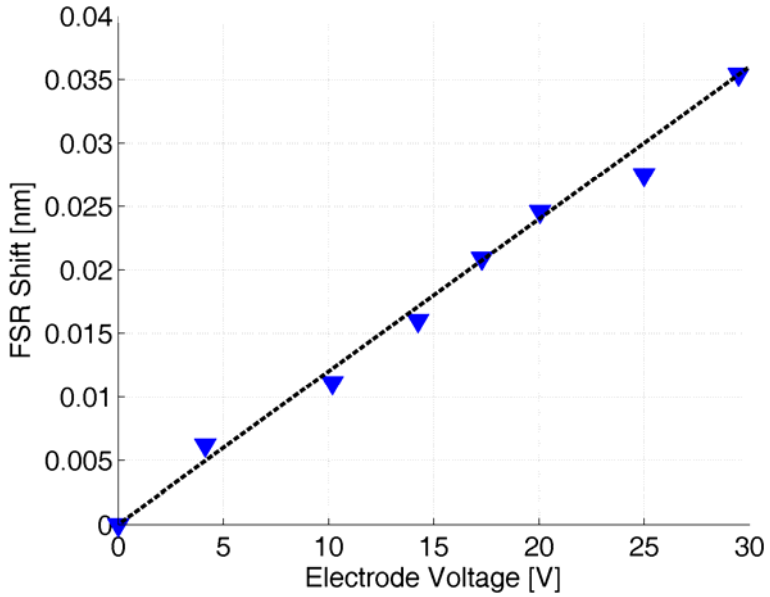

Fig. 65. Measured ring resonator FSR shift with sweep of electrode DC voltage.

The data was fit with a linear trend line having $R^2 = 0.991$ and showed a tuning rate of 0.001 *nm/V* at 1528 *nm*. From this it follows that V_π is 17.3 *V* at 1528 *nm*. With 12 *mm* long electrodes, the voltage-length product at 1528 *nm* is 20.8 *V-cm*. This is larger than the previously mentioned interferometer tuning voltage, which is believed to be due in part to differences in device fabrication since this measurement was taken on a different sample. This sample also showed slightly larger tuning voltages on the interferometers, suggesting a difference in the SiO_2 film quality and/or Al film quality.

Along with measuring the FSR shift, curve fitting was carried out on each response to extract the coupling and round trip loss, which can be seen in Table 11. As expected, while there is a shift in the FSR, there is no significant change in the coupling or round trip loss. The small variations observed are believed to be curve fitting errors.

Table 11. Electro-optic tuning of ring path length.

Voltage	FSR Shift (%)	Coupling (%)	Round Trip Loss (dB)
0 V	--	57.84%	9.71 dB
10 V	29.4%	58.30%	9.77 dB
20 V	58.7%	57.92%	9.68 dB
30 V	88.2%	58.77%	9.80 dB

C.2. Coupling Region Tuning

Unlike in the interferometer case, coupling region tuning has also been observed with the ring resonator. Similar to the path length tuning where a phase shift is generated along the path length, for coupling region tuning a phase shift is generated

between the back to back tapers. A similar ACPS electrode structure is used, but it is wider to accommodate the Ti:$LiNbO_3$ diffused waveguide that is in the coupling region.

Recall the two different design considerations mentioned for As_2S_3 ring resonators, following from the fact that the two As_2S_3 tapers could either be gapped or connected by a thin As_2S_3 strip. The addition of this thin As_2S_3 strip establishes a larger tuning difference between the two supermodes as seen in Fig. 26, giving improved coupling tuning capabilities. Table 12 shows the tuning performance of two 5 GHz ring resonators. The coupling percentage and round trip loss were extracted from curve fitting the insertion loss and group delay at 1.9369×10^5 GHz and 1.9468×10^5 GHz for the connected and gapped tapers, respectively. The magnitude response (insertion loss) can also be seen for the connected and gapped tapers in Fig. 66 and Fig. 67, respectively. For both fabricated devices, these were the wavelengths that showed the best ring response.

Table 12. Electro-optic tuning of ring resonator coupling region.

	Connected As_2S_3 Tapers		Gapped As_2S_3 Tapers	
Voltage	Coupling (%)	Round Trip Loss (dB)	Coupling (%)	Round Trip Loss (dB)
0 V	74.07%	6.06 dB	92.43%	10.53 dB
7 V	75.02%	5.92 dB	91.63%	10.14 dB
14 V	79.80%	5.94 dB	91.70%	10.36 dB
21 V	87.61%	5.75 dB	90.52%	10.06 dB
28 V	85.84%	5.84 dB	89.48%	10.14 dB
42 V	82.79%	6.18 dB	88.30%	10.12 dB

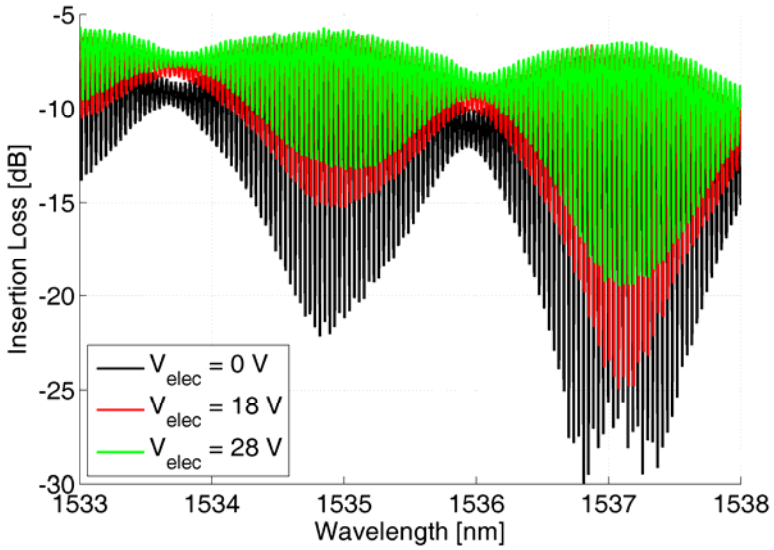

Fig. 66. Coupling tuning response for connected tapers.

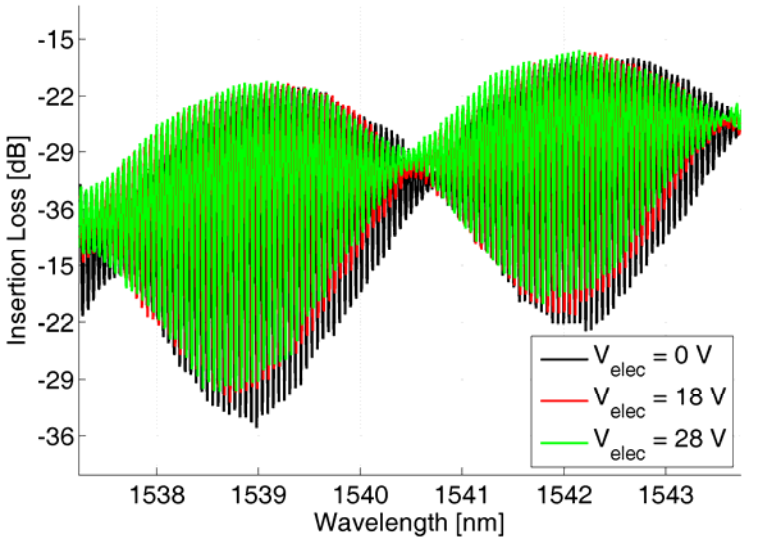

Fig. 67. Coupling tuning response for gapped tapers.

As expected, the connected tapers show improved coupling tuning when compared to the gapped tapers. This is due to the tuning strength difference created between the supermodes. Upon closer inspection of Fig. 66, which is seen in Fig. 68, there appears to be a slight shift of the FSR. This is because the coupling region tapers do include a small portion of the optical path length for the ring resonator. Recall from Fig. 14 that the mode is confined in the As_2S_3 waveguide before the end of the taper is reached, which means that portion of the taper is part of the As_2S_3 path length. This FSR shift could be eliminated by restricting the ACPS electrodes to only the 0.8 μm wide strip portion that connects the tapers, instead of the entire coupling region.

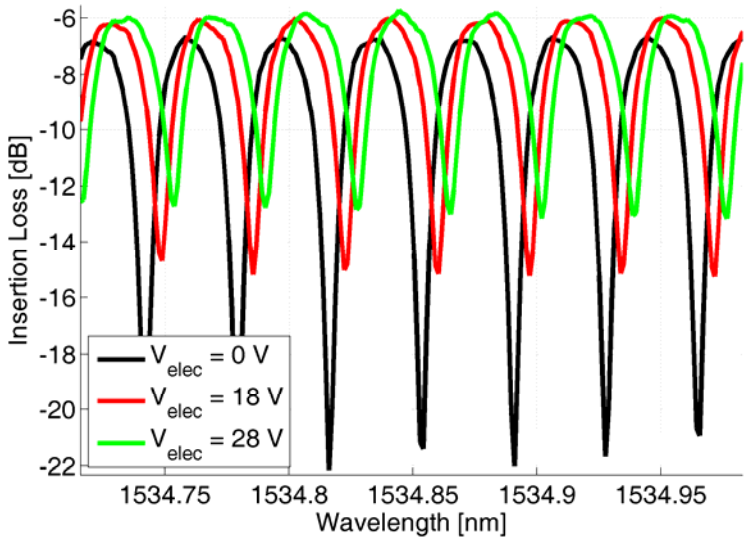

Fig. 68. Coupling region tuning with connected taper, zoomed in to see slight FSR shift.

With tuning of both the coupling region and path length, an electro-optically tunable microring resonator has been demonstrated. Since contact lithography results in

deviations between fabricated devices that changes the power coupling ratio, tuning of the coupling region allows for possibly achieving the desired coupling ratio despite these fabrication difficulties. It is noted that only a ~ 15% change in the coupling ratio is achievable, so fabrication still limits the range of achievable coupling percentages.

Matlab simulations can be carried out based on the above device parameters to get an idea of the frequency chirps that could be generated with such a device. Recall that an 83% coupling coefficient is desired, but also with low optical losses. Since the optical losses of these waveguides increase with coupling, a higher coupling coefficient will produce better results. Fig. 69 looks at a ring resonator with 88% coupling and 5.8 dB of round trip loss, which was an observed ring resonator with connected tapers as seen in Table 12. The gapped tapers have optical losses that are too large. The comparison with the hyperbolic tangent function can be seen in Fig. 70.

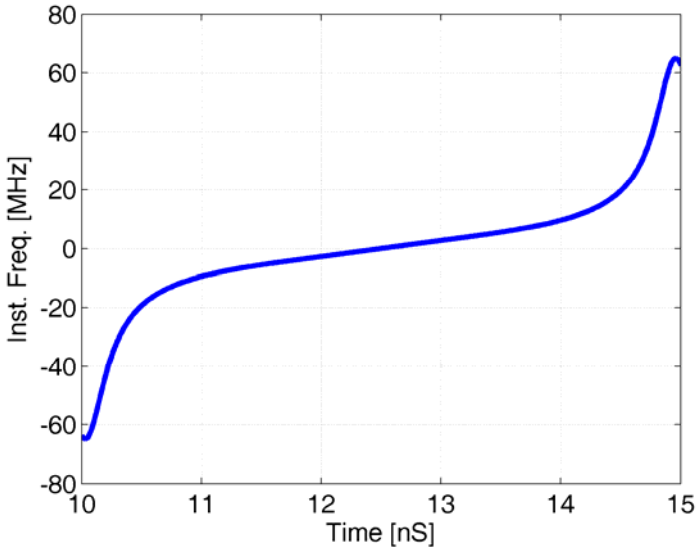

Fig. 69. Simulated frequency chirp for fabricated device.

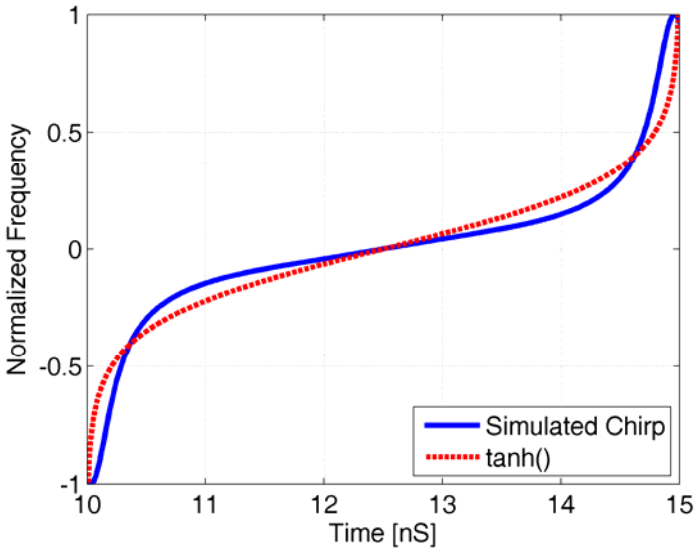

Fig. 70. Simulated frequency chirp for fabricated device, compared to hyperbolic tangent.

CHAPTER V

CONCLUSIONS

In this work, electro-optic tuning of an optical mode guided by an As_2S_3 rib waveguide was realized. While As_2S_3 itself does not exhibit electro-optic properties, through the rib waveguide design we are able to limit mode confinement so that a portion of the mode is present in the electro-optically tunable $LiNbO_3$ substrate. This allows for electro-optic tuning of the mode as in a substrate mode case, at the expense of a larger tuning voltage.

Tuning was shown for both an interferometer and a ring resonator. While both are two-path devices, the ring resonator takes advantage of a feedback path. Feedback systems are commonly used in electronics, and even in optics feedback provides more device functionality. Coupling region tuning is caused by a relative phase shift between two couplers, which the interferometer lacks but the feedback in the ring resonator provides.

Tuning voltages for the ring resonator path length, which is used to shift the FSR, were measured to be 20.8 *V-cm*. While this is a large voltage when compared to commercial $LiNbO_3$ linear modulators, it is a 42% improvement over tuning voltages for other attempts at a tunable $LiNbO_3$ microring resonator.

For waveform generation applications, the coupling region would typically be left at a fixed coupling strength. Since fabrication defects can cause variations in the coupling percentage, coupling region tuning gives the ability to overcome fabrication

tolerances to achieve the desired coupling percentage. Modulation of the optical path length through the ring path electrodes generates frequency chirps. While this device is limited to a few hundred MHz modulation rates, the maximum chirp that can be generated is in the GHz range when there is the right balance between coupling percentage and round trip loss.

The one main drawback of the devices shown in this work is that they take advantage of the r_{13} electro-optic tuning coefficient, not the stronger r_{33} coefficient which is commonly used. This fact, along with only a portion of the optical mode seeing the electro-optically tunable $LiNbO_3$ substrate, results in a tuning voltage three to four times larger than the 5 *V-cm* typically desired and seen with interferometric modulators. While a switch to the TE polarization would allow for the stronger r_{33} to be utilized under the same device architecture, it is more challenging to fabricate the necessary mode coupling tapers under the feature resolution constraints of contact lithography. A change in systems to stepper or e-beam lithography would give the resolution improvement that could help realize TE mode coupling, and the alignment improvements would also allow for smaller electrode gaps to be fabricated while still avoiding overlap.

A. Further Work

While a ring resonator with a high coupling percentage is desired, it comes at the expense of higher round trip losses. This is believed to be due to the Ti:$LiNbO_3$ surface bump after diffusion. Recall that two common waveguide methods were mentioned for

$LiNbO_3$ substrate, titanium diffusion and proton exchange. Not only are proton exchange waveguides quicker to fabricate since they do not require a 10 hour diffusion and an additional 8 hours to cool down to room temperature, but they also do not show the large surface bumps in the waveguiding region. Hence, annealed proton exchange (APE) waveguides may provide a route to realizing high coupling ring resonators with low losses.

APE waveguides also support TE polarization for x-cut $LiNbO_3$ substrate, so they would allow for electro-optic tuning with r_{33} while utilizing a very similar electrode design. From the increase in tuning coefficient strength it could be expected to see a 3x reduction in the tuning voltage, which would get the tuning voltages down to more competitive levels.

In order to truly realize an all-pass filter structure, gain needs to be added to the ring optical path length. While erbium doping can be used to achieve gain with a pump wavelength, it is crucial to reduce the round trip losses as the amount of gain is limited. Our group has briefly experimented with Er-doped waveguides which could provide gain in the same waveguide configuration.

REFERENCES

[1] AT&T (2012, Accessed 2012, April 25), "Milestones in AT&T History." [Online]. Available: http://www.corp.att.com/history/milestones.html

[2] Hibernia Atlantic (2009, Accessed 2012, April 25), "Hibernia Offers Cross-Atlantic 40G." [Online]. Available: http://www.lightreading.com/document.asp?doc_id=180473

[3] A. Hutchinson, *Big Ideas: 100 Modern Inventions That Have Transformed Our World.* New York: Sterling Publishing Company, 2009.

[4] I. P. Kaminow, V. Ramaswamy, R. V. Schmidt, and E. H. Turner, "Lithium niobate ridge waveguide modulator," *Applied Physics Letters*, vol. 24, no. 12, pp. 622-624, Jun. 1974.

[5] A. Yariv, "The beginning of optoelectronic integrated circuits – A personal perspective," *IEEE Journal of Lightwave Technology*, vol. 26, no. 9, pp. 1172-1175, May 2008.

[6] L. Tsybeskov, D. Lockwood, and M. Ichikawa, "Silicon photonics: CMOS going optical," *Proceedings of the IEEE*, vol. 97, no. 7, pp. 1161-1165, Jul. 2009.

[7] *40 GHz Phase and Intensity Modulators Data Sheet*, Thorlabs Inc., Newton, NJ, 2012.

[8] R. C. Alferness, "Titanium-diffused lithium niobate waveguide devices," *1986 Sixth IEEE International Symposium on Applications of Ferroelectronics*, pp. 1-3, 1986.

[9] M. Garcia-Granda, H. Hu, J. Rodriguez-Garcia, and W. Sohler, "Design and fabrication of novel ridge guide modulators in lithium niobate," *IEEE Journal of Lightwave Technology*, vol. 27, no. 24, pp. 5690-5697, Dec. 2009.

[10] M. Marris-Morini, L. Vivien, G. Rasigade, J. M. Fedeli, E. Cassan, et al., "Recent progress in high-speed silicon-based optical modulators," *Proceedings of the IEEE*, vol. 97, no. 7, pp. 1199-1215, Jul. 2009.

[11] R. V. Schmidt, I. P. Kaminow, "Metal-diffused optical waveguides in LiNbO3," *Applied Physics Letters*, vol. 25, no. 8, pp. 458-460, Oct. 1974.

[12] J. L. Jackel, C. E. Rice, and J. J. Veselka, "Proton exchange for high-index waveguides in LiNbO3," *Applied Physics Letters*, vol. 41, no. 7, pp. 607-608, Oct. 1982.

[13] J. M. M. M. de Almeida, "Design methodology of annealed H+ waveguides in ferroelectric LiNbO3," *Optical Engineering*, vol. 46, no. 6, pp. 1-13, May 2007, paper 064601.

[14] K. J. Vahala, "Optical microcavities," *Nature*, vol. 424, pp. 839-846, Aug. 2003.

[15] L. Chen, N. Sherwood-Droz, and M. Lipson, "Compact bandwidth tunable microring resonators," *Optics Letters*, vol. 32, no. 22, pp. 3361-3363, Nov. 2007.

[16] Q. Xu, B. Schmidt, S. Pradhan, and M. Lipson, "Micrometer scale silicon electro-optic modulator," *Nature*, vol 435, no. 19, pp. 325-327, May 2005.

[17] D. Dai, L. Yang, and S. He, "Ultrasmall thermally tunable microring resonator with a submicrometer heater on Si nanowires," *IEEE Journal of Lightwave Technology*, vol. 26, no. 6, pp. 704-709, Mar. 2008.

[18] L. Liao, D. Samara-Rubio, M. Morse, A. Liu, D. Hodge, et al., "High speed silicon Mach-Zehnder interferometer," *Optics Express*, vol. 13, no. 8, pp. 3129-3135, Aug. 2005.

[19] A. Guarino, G. Poberaj, D. Rezzonico, R. Degl'Innocenti, and P. Guenter, "Electro-optically tunable microring resonators in lithium niobate," *Nature Photonics*, vol. 1, no. 7, pp. 407-410, Jul. 2007.

[20] T. J. Wang, C. H. Chu, and C. Y. Lin, "Electro-optically tunable microring resonators on lithium niobate," *Optics Letters*, vol. 32, no. 19, pp. 2777-2779, Oct. 2007.

[21] M. E. Solmaz, "Integration of arsenic trisulfide and titanium diffused lithium niobate waveguides," Ph.D. dissertation, Dept. Electrical Engineering, Texas A&M University, College Station, TX, 2010.

[22] O. Mikami, J. Noda, S. Zembutsu, and S. Fukunishi, "Phase tuning in optical directional coupler by photostructural effect of chalcogenide glass film," *Applied Physics Letters*, vol. 31, no. 6, pp. 376-378, Sep. 1977.

[23] M. E. Solmaz, D. B. Adams, W. C. Tan, W. T. Snider, and C. K . Madsen, "Vertically integrated As2S3 ring resonator on LiNbO3," *Optics Letters*, vol. 43, no. 11, pp. 1735-1737, Jun. 2009.

[24] D. K. Cheng, *Fundamentals of Engineering Electromagnetics*. Upple Saddle River, New Jersey: Prentice Hall, 1993.

[25] E. Rosencher and B. Vinter, *Optoelectronics*. United Kingdom: Cambridge University Press, 1998.

[26] *Handbook of Optics, Volume IV – Optical Properties of Materials, Nonlinear Optics, Quantum Optics,* 3rd ed, M. Bass, Ed.. New York: McGraw-Hill, 2012.

[27] D. E. Zelmon and D. L. Small, "Infrared corrected Sellmeier coefficients for congruently grown lithium niobate and 5 mol. % magnesium oxide-doped lithium niobate," *Journal of the Optical Society of America B*, vol. 14, no. 12, pp. 3319-3322, Dec. 1997.

[28] W. S. Rodney, I. H. Malitson, and T. A. King, "Refractive index of arsenic trisulfide," *Journal of the Optical Society of America*, vol. 48, no. 9, pp. 633-636, Sep. 1958.

[29] E. A. J. Marcatili, "Dielectric rectangular waveguide and directional coupler for integrated optics," *Bell Systems Technology Journal*, vol. 48, no. 21, pp. 2071-2102, Sep. 1969.

[30] R. M. Knox and P. P. Toulios, "Integrated circuits for the millimeter through optical frequency range," presented at the Symposium on Submillimeter Waves, Polytechnic Institute of Brooklyn, 1970.

[31] A. S. Sudbo, "Film mode matching method: A versatile numerical method for vector mode field calculations in dielectric waveguides," *Pure and Applied Optics: Journal of the European Optical Society Part A*, vol. 2, no. 3, pp. 211-233, May 1993.

[32] *FimmWave User Manual*, *Version 5.2*, Photon Design, Oxford, United Kingdom, 1997.

[33] G. B. Hocker and W. K. Burns, "Mode dispersion in diffused channel waveguides by the effective index method," *Applied Optics*, vol. 16, no. 1, pp. 113-118, Jan. 1977.

[34] L. McCaughan and E. Bergmann, "Index distribution of optical waveguides from their mode profile," *IEEE Journal of Lightwave Technology*, vol. 1, no. 1, pp. 241-244, Mar. 1983.

[35] J. Helms, J. Schmidtchen, B. Schuppert, and K. Petermann, "Error analysis for refractive index profile determination from near-field measurements," *IEEE Journal of Lightwave Technology*, vol. 8, no. 5, pp. 625-633, May 1990.

[36] T. O'Haver (2012, Accessed 2011, November 13), "An Introduction to Signal Processing in Chemical Analysis." [Online]. Available: http://terpconnect.umd.edu/~toh/spectrum/TOC.html

[37] S. J. Orfanidis, *Introduction to Signal Processing*. Englewood Cliffs: Prentice Hall, 1996.

[38] I. Fatadin, D. Ives, and M. Wicks, "Accurate magnified near-field measurements of optical waveguides using a calibrated CCD camera," *IEEE Journal of Lightwave Technology*, vol. 24, no. 12, pp. 5067-5074, Dec. 2006.

[39] F. L. Pedrotti, L. S. Pedrotti, and L. M. Pedrotti, *Introduction to Optics,* 3rd ed. San Francisco: Pearson Education, 2007.

[40] B. Moslehi, J. W. Goodman, M. Tur, and H. J. Shaw, "Fiber-optic lattice signal processing," *Proceedings of the IEEE*, vol. 72, no. 7, pp. 909-930, Jul. 1984.

[41] C. K. Madsen and J. H. Zhao, *Optical Filter Design and Analysis: A Signal Processing Approach*. New York: John Wiley and Sons, 1999.

[42] M. E. Solmaz, Y. Zhou, and C. K. Madsen, "Modeling asymmetric resonances using an optical filter approach," *IEEE Journal of Lightwave Technology*, vol. 28, no. 20, pp. 2951-2955, Oct. 2010.

[43] H. Nishihara, M. Haruna, and T. Suhara, *Optical Integrated Circuits*. New York: McGraw-Hill, 1985.

[44] V. M. Menon, X. Fengnian, and S. R. Forrest, "Photonic integration using asymmetric twin-waveguide (ATG) technology: Part II-devices," *IEEE Journal of Selected Topics in Quantum Electronics*, vol. 11, no. 1, pp. 30-42, Jan. 2005.

[45] I. Moerman, P. P. VanDaele, and P. M. Demeester, "A review on fabrication technologies for the monolithic integration of tapers with III-V semiconductor devices," *IEEE Journal of Selected Topics in Quantum Electronics*, vol. 3, no. 6, pp. 1308-1320, Dec. 1998.

[46] J. Haes, J. Willems, and R. Baets, "Design of adiabatic tapers for high-contrast step index waveguides," *Proceedings of the SPIE*, vol. 2212, pp. 685-693, Aug. 1994.

[47] Y. Zhou, X. Xia, W. T. Snider, J. Kim, Q. Chen, et al, "Two-stage taper enhanced ultra-high Q As2S3 ring resonator on LiNbO3," *IEEE Photonics Technology Letters*, vol. 23, no. 17, pp. 1195-1197, Sep. 2011.

[48] N. Courjal, N. P. Bernal, J. Hauden, J. Amet, M. Roussey, et al., "Some new trends on lithium niobate modulators," *Proceedings of the SPIE*, vol. 6123, pp. 80-94, Mar. 2006.

[49] M. M. Howerton and W. K. Burns, "Broadband traveling wave modulators in LiNbO3," *RF Photonic Technology in Optical Fiber Links.* West Nyack, NY: Cambridge University Press, pp. 133-164, 2002.

[50] A. Dutta, N. Dutta, and M. Fujiwara, *WDM technologies: Active optical components*. San Diego: Academic Press, 2002.

[51] M. Minikata, "Recent progress of 40-GHz high-speed LiNbO3 optical modulator," *Proceedings of the SPIE*, vol. 4532, pp. 16-27, Aug. 2001.

[52] D. W. Dolfi and T. R. Ranganath, "50 GHz velocity matched broad wavelength LiNbO3 modulator with multimode active section," *Electronics Letters*, vol. 28, no. 13, pp. 1197-1198, Jun. 1992.

[53] R. C. Alferness, "Waveguide electrooptic modulators," *IEEE Transactions on Microwave Theory and Techniques*, vol. 30, no. 8, pp. 1121-1137, Aug. 1982.

[54] T. Kitoh and K. Kawano, "Modeling and design of Ti:LiNbO3 optical modulator electrodes with a buffer layer," *IEICI Transactions*, vol. 76, no. 6, pp. 422-429, Jun. 1992.

[55] D. Marcuse, "Optimal electrode design for integrated optics modulators," *IEEE Journal of Quantum Electronics*, vol. 18, no. 3, pp. 393-398, Mar. 1982.

[56] X. Xia, Y. Zhou, and C. K. Madsen, "Analysis of As2S3-Ti:LiNbO3 taper couplers using supermode theory," *IEEE Journal of Lightwave Technology*, submitted for publication.

[57] D. B. Adams, W. T. Snider, and C. K. Madsen, "NLFM waveform generation using tunable integrated optical ring resonators: Simulation and proof of concept experiment," *Optics Express*, vol. 18, no. 12, pp. 12537-12542, Jun. 2010.

[58] D. G. Youmans, "Waveform comparison for coherent ladar imaging using a helicopter facet model target," *Proceedings of the SPIE*, vol. 7323, pp. 1-12, May 2009, paper 732304.

[59] D. B. Adams, W. T. Snider, and C. K. Madsen, "A novel NLFM waveform generator using tunable integrated optical ring resonators: Simulation and proof of concept," *Proceedings of the SPIE*, vol. 7684, pp. 1-12, Apr. 2010, paper 76841A.

[60] R. Keil and F. Auracher, "Coupling of single mode Ti-diffused LiNbO3 waveguides to single-mode fibers," *Optics Communications*, vol. 30, no. 1, pp. 23-28, Jul. 1979.

[61] M. E. Schoff, "Sputter target erosion and its effects on long duration DC magnetron sputter coating," M.S. thesis, Dept. Mechanical Engineering, University of California, San Diego, CA, 2009.

[62] *Stiletto & CT-X Series Magnetron Sputtering Sources: Installation & Operation Manual*, AJA International Inc., North Scituate, MA, 2004.

[63] *Lesker Tech, Volume 7*, Kurt J. Lesker Company, Pittsburgh, PA, 2010.

[64] M. K. Bahl, R. O. Woodall, R. L. Watson, K. J. Irgolic, "Relaxation during photoemission and LMM auger decay in arsenic and some of its compounds," *Journal of Chemical Physics*, vol. 64, no. 3, pp. 1210-1218, Feb. 1976.

[65] D. Y. Choi, S. Madden, A. Rode, R. Wang, and B. Luther-Davies, "Dry etching characteristics of amorphous As2S3 film in CHF3 plasma," *Journal of Applied Physics*, vol. 104, no. 11, pp. 1-6, Dec. 2008, paper 113305.

[66] *AZ 5200-E Photoresist Data Package*, AZ Electronic Materials, Branchburg, NJ, 2008.

APPENDIX A

STEP-BY-STEP FABRICATION PROCESS

Titanium Layer

- Deposition
  - Clean $LiNbO_3$ substrate with soapy water and solvents, using a q-tip
  - Final solvent rinse with IPA, blow sample dry with N_2 gun
  - Deposit Titanium in AJA system
  - Aim for **950 nm** thick film
- Lithography
  - Solvent rinse with IPA, blow samples dry with N_2 gun
  - Spin coat AZ-5214 photoresist, **4000 RPM** (40 second spin, 5 second ramp)
  - Soft bake on hot plate, 125°C, 1 minute
  - Expose on MA6 contact mask aligner, dose of **65 mJ/cm^2**
  - Develop in MF-312 (Dilute 312:H_2O, 1:1.2)
  - Hard bake in oven, 135°C, 8 minutes
- Etching
  - Etch with RIE
  - Remove photoresist with heated AZ-300T photoresist stripper
    - Heat above 90°C, let soak for ~ 15 minutes
    - Let cool to room temperature before cleaning in water and solvents
    - Final solvent rinse with IPA, blow dry with N_2 gun
- Diffusion
  - Center samples in alumina boat, and place alumina boat in center of furnace
  - Diffuse at 1035°C
    - Gas flow, heated wet breathing air (35 sccm, 70°C)
    - Diffusion time 11 hr 15 min (1 hr 15 min warm up, 10 hr diffusion)
  - Allow samples to cool down to room temperature before removing from furnace

- Polishing
    - Dice off 0.75 mm from each facet edge of the sample to remove edge bead
    - Polish each facet edge to optical quality
        - 15 μm polishing pad, 2 min, 133 RPM (Speed Setting 8)
        - 3 μm polishing pad, 1 min 30 sec, 86 RPM (Speed Setting 6)
        - 0.5 μm polishing pad, 1 min 30 sec, 54 RPM (Speed Setting 4)
    - Clean substrate with soapy water and solvents, using a q-tip
    - Final solvent rinse in IPA, blow dry with N_2 gun

Arsenic Trisulfide Layer

- Deposition
    - Deposit As_2S_3 in AJA system
    - Aim for **475 nm** thick film
    - Deposit SiO_2+Ti protective layer in AJA system
- Lithography
    - Solvent rinse with IPA, blow samples dry with N_2 gun
    - Spin coat AZ-5214 photoresist, **7000 RPM** (40 second spin, 5 second ramp)
    - Soft bake on hot plate, 125°C, 1 minute
    - Expose on MA6 contact mask aligner, dose of **95 mJ/cm^2**
    - Develop in MF-312 (Dilute 312:H_2O, 1:1.3)
    - Hard bake in oven, 135°C, **30 minutes**
- Etching
    - Etch with RIE
    - Oxygen plasma ashing for photoresist removal
        - O_2: 100 sccm
        - 40 mT, 25°C, 100 W RF
        - Ash for 12 minutes

- Protective layer removal
    - Use HF (Dilute HF:H_2O, 1:30) to remove protective layer, 2 minutes
        - Make sure you use a Nalgene/plastic beaker
    - Clean samples with a solvent rinse
    - Solvent rinse with IPA, blow samples dry with N_2 gun

Aluminum Electrode Layer

- Buffer layer deposition
    - Deposit SiO_2 in AJA system
    - Aim for **138 nm** thick film
- Aluminum deposition
    - Deposit Al in AJA system
    - Cover facet edges with Kapton tape, so Al does not deposit on facet edge
    - Aim for **500 nm** thick film
- Lithography
    - Solvent rinse with IPA, blow samples dry with N_2 gun
    - Spin coat AZ-5214 photoresist, **4000 RPM** (40 second spin, 5 second ramp)
    - Soft bake on hot plate, 125°C, 1 minute
    - Expose on MA6 contact mask aligner, dose of **65 mJ/cm^2**
    - Develop in MF-312 (Dilute 312:H_2O, 1:1.2)
    - Hard bake in oven, 135°C, 8 minutes
- Etching
    - Use Aluminum Etch, no dilution, room temperature
        - Make sure you use a Nalgene/plastic beaker
        - Will not initially look like it is etching, takes ~ 10 min
        - Every 3 minutes remove sample and rinse under H_2O, then return to Aluminum etch
    - Remove photoresist with acetone
        - Should easily come off, soak in acetone for ~ 10 minutes
    - Solvent rinse with IPA, blow samples dry with N_2 gun

APPENDIX B

AJA DC/RF MAGNETRON SPUTTERING OPERATING INSTRUCTIONS

Loading Sample(s) Into The AJA System

1. Turn on the water chiller.

2. Tape samples to the bottom of the substrate holder. **Be sure to also include a Si dummy sample for measuring film thickness.** If film is a metal (or thickness cannot be measured by spectral reflectance), be sure to put Sharpie® marks on the dummy using an Ultra Fine Tip Sharpie®.

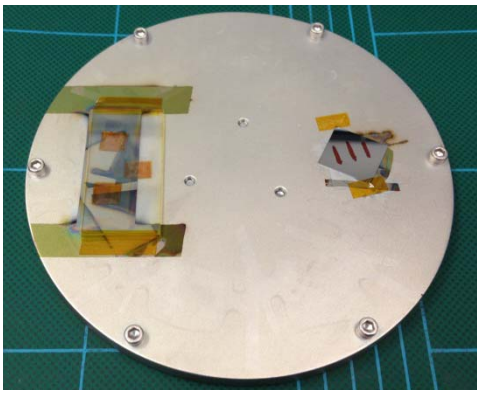

3. Place substrate holder in the load-lock. Orient the substrate holder as shown below, with the motor fin slot oriented along the transfer arm axis.

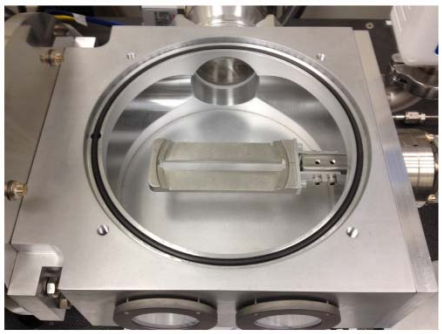

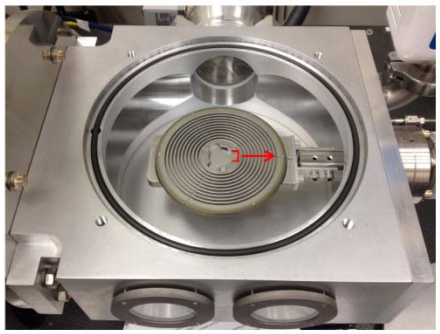

4. Turn on load-lock roughing pump. **Wait until pressure reaches 10^{-5} torr range.**

5. **Make sure that motor arm is raised in the main chamber to 28 mm,** so that the transfer arm will not make contact with it when pushed into the chamber.

6. When the load-lock pressure is in the 10^{-5} torr range, open the gate valve between the load-lock and main chamber and slowly push transfer arm into the chamber.

7. Orient the motor arm so that it is ready to pick up sample. This position is marked with a 'U', and the arrow should be pointing to the screw head. Once in position, slowly lower arm until there is approximately a 2 mm gap between the motor arm and the substrate holder. When the motor arm is in the substrate holder, slowly spin the motor arm **clockwise** until you feel it stop. At this point, the position is roughly marked with a 'L'.

8. **Raise motor arm back to height of 28 mm,** then slowly pull transfer arm back into load-lock. Close the gate valve between the load-lock and main chamber.

Film Deposition

9. Position motor arm at height specified in the film recipe (working distance). Make sure you get down at eye level with the needle, to ensure it is pointing at the right height.

10. Open up the gas cylinders (Ar and O_2) as necessary for the film recipe.

11. Turn on the computer, and open the program **PHASEIIJ**. Authorized users know the password.

12. On the System Configuration screen that comes up, do not change anything; just click **Config Save/Close**.

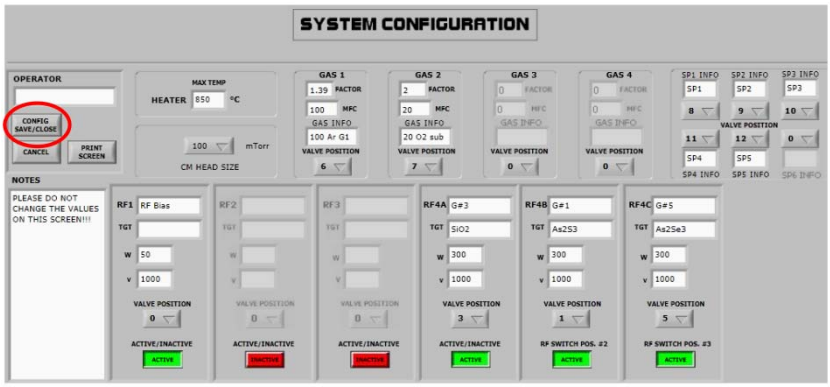

13. **Ensure that gas flow rates are approximately zero (0 ± 0.3).** If they are not, then adjust the calibration screws on the back of the flow meters. For this it helps to have two people; one person adjusting the screw, and the second person watching the flow rate on the computer.

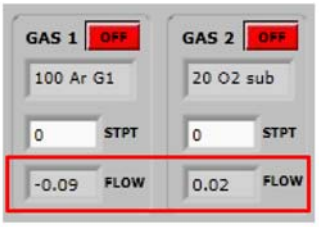

14. In AJA Computer Control, turn on **ROTATION** and **GAS** Flow. Then type in the gas flow rate, and press enter.

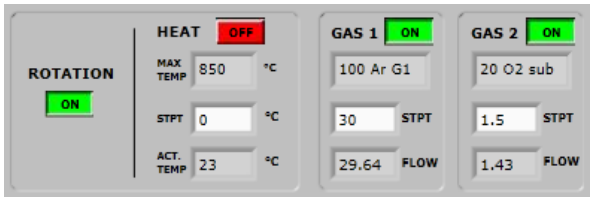

15. **Put APC in Remote Mode,** by pressing and holding **REMOTE** until it lights up.

16. In AJA Computer Control, click on **PRESSURE**, type in desired run pressure, then press enter. The APC will adjust the hi-vac valve accordingly for the desired chamber pressure.

    Note that for the APC position (hi-vac valve), 0 = Fully Closed, 100 = Fully Open, and any number in between means the hi-vac valve is partially open.

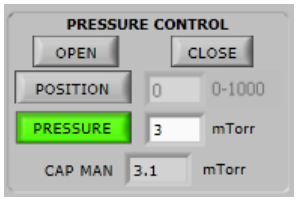

17. In AJA Computer Control, find the desired film for deposition and turn on the sputtering gun. **Do not believe the little light that indicates when there is a plasma.** We disabled that control to get our low power plasmas to work.

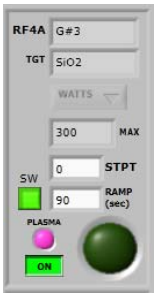

18. **This step is very important, the order you type things in matters!** Type a power ramp time first (do not exceed 3 W/sec) in **RAMP**, then type in the desired power in **STPT** and press enter. The power supply will automatically start ramping the power.

    a. For **DC plasma**, wait until the ramp time is completed.

    b. For **RF plasma**, they will not strike at low pressure. When power begins to ramp, close the hi-vac valve by clicking on **CLOSE** in the Pressure Control. For every film except SiO_2, look in the chamber and wait until a plasma is seen. When there is plasma, return to **PRESSURE** mode and wait for ramp time.

       For SiO_2, you cannot see the sputtering gun through the view port, so after you **CLOSE** the hi-vac valve wait until you see a DC bias (**DCV**) on the RF power supply, then return to **PRESSURE** mode and wait for ramp time.

19. After the power has ramped up to full power, allow the target to pre-sputter with the shutter still closed. **Typical pre-sputtering time is 3 minutes.**

20. When pre-sputtering is completed, **ensure that the shield for the viewing port is closed,** and open the shutter by clicking the big green button in AJA Computer Control. Keep shutter open for desired sputtering time.

21. **Fill out the log book. Record APC hi-vac valve position and power supply parameters in the log book after the shutter is opened.**

22. When desired film sputtering time is reached, close the shutter.

23. **This step is very important, the order you type things in matters!** Type a power ramp time first (do not exceed 3 W/sec) in **RAMP**, then type in 0 for the desired power in **STPT** and press enter. The power supply will ramp down and extinguish the plasma. Wait until the ramp time is completed, then turn off the gun.

24. In AJA Computer Control return the Pressure Control to **OPEN**, turn off the **GAS**, and turn off the **ROTATION**.

Unloading Sample(s)

25. **Raise the motor arm back to height of 28 mm** so that transfer arm will not contact it. Open the gate valve between the load-lock and main chamber, and slowly push in transfer arm.

26. Orient substrate holder so that it will drop down into the transfer arm, and slowly lower.

27. Once in transfer arm, slowly spin the motor arm **counterclockwise** until you feel it stop.

28. **Raise motor arm back to height of 28 mm,** and substrate holder should remain in transfer arm.

29. Return transfer arm to load-lock, and close gate valve between load-lock and main chamber.

30. Open nitrogen valve, and turn off load-lock roughing pump. Load-lock will automatically begin to vent. When it reaches atmosphere, remove substrate holder. **Leave load-lock at atmosphere.**

31. Put the APC back into local mode (press and hold), and ensure that the valve position is **OPEN**. If it is not open, then press the **OPEN** button on the front panel.

32. Close the PHASEIIJ program, and shut down the computer.

33. **Wait until at least 10 minutes have passed after extinguishing plasmas before turning off the water chiller.**

APPENDIX C

MATLAB CODE FOR FREQUENCY CHIRP SIMULATION

```
% W. Tim Snider
% Ring Chirp Response
% 19 August 2011

clear all
close all

%% Wavelength Sweep and Ring Information
wl_ctr = 1531;                  % center wavelength [nm]
FSR = 5e9;                      % ring FSR [Hz]
n_eff = 2.23;                   % effective index for ring

loss = 2.0;                     % round trip loss for ring [dB]
k = 0.50;                       % power coupling coefficient

wl_start = wl_ctr-0.25;         % starting wavelength [nm]
wl_end = wl_ctr+0.25;           % ending wavelength [nm]
wl_nm = wl_start:0.00005:wl_end;
wl = wl_nm.*1e-9;               % right units for calculations

L = (FSR.*2.45./3e8)^(-1);      % physical path length of ring
beta = 2.*pi.*n_eff./wl;        % propagation constant


%% APF Transfer Function
c = sqrt(1-k);
z = exp((i.*beta.*L));
gamma = 10^(-1.*loss./20);

H = (c-gamma.*(z.^-1))./(1-c.*gamma.*(z.^-1));
H_amp = 10*log(abs(H).^2);
H_phase = angle(H);
H_phase_unwrap = unwrap(angle(H))./pi;


%% Plot Magnitude and Phase Information
figure(111)
subplot(2,1,1)                  % magnitude
set(gca,'FontSize',16)
hold on
plot(wl_nm,H_amp,'-r','LineWidth',2,'DisplayName','\kappa = 80%')
xlabel('Wavelength [nm]')
ylabel('Intensity [dB]')
```

```
title(sprintf('Amplitude and Phase Response for %0.0f GHz
Ring',FSR/1e9),'FontSize',16,'FontWeight','demi')
grid on

subplot(2,1,2)                  % phase
set(gca,'FontSize',16)
plot(wl_nm,H_phase,'-b','LineWidth',2)
xlabel('Wavelength [nm]')
ylabel('Phase [rad]')
grid on


% Select data points to zoom in on one FSR
dummy = input('Select two points (p1 and p2) that bound FSR region to
zoom in on');

figure(2)
hold on
subplot(2,1,1)                  % magnitude, one FSR
set(gca,'FontSize',16)
plot(wl_nm,H_amp,'-b','LineWidth',2)
xlabel('Wavelength [nm]')
ylabel('Intensity [dB]')
xlim([p1.Position(1) p2.Position(1)])
title(sprintf('Amplitude and Phase Response for %0.0f GHz
Ring',FSR/1e9),'FontSize',16,'FontWeight','demi')
grid on

subplot(2,1,2)                  % unwrapped phase, one FSR
set(gca,'FontSize',16)
plot(wl_nm,H_phase_unwrap,'-b','LineWidth',2)
xlabel('Wavelength [nm]')
ylabel('Phase [rad /\pi]')
xlim([p1.Position(1) p2.Position(1)])
maxy = max([H_phase_unwrap(p1.DataIndex)
H_phase_unwrap(p2.DataIndex)]);
miny = min([H_phase_unwrap(p1.DataIndex)
H_phase_unwrap(p2.DataIndex)]);
ylim([miny-0.5 maxy+0.5])
grid on


%% Sinusoidal Ring Phase Modulation
% Phase shifter electrodes change refractive index

%wl_ctr = (p1.Position(1)+p2.Position(1))/2;
wl_ctr = 1531.0199;             % max
wl = wl_ctr.*1e-9;

mod_freq = 100e6;               % modulation frequency
t = 0:1/(mod_freq*1e3):50e-9;
x = -4*pi:0.00001:4*pi;         % couple periods of modulation
```

```
y = sin(2.*pi.*mod_freq.*t)+1;

dn = 0.0000312;          % refractive index change for pi phase shift
M = 2;                   % desired total phase shift, M*pi

n_t_eff = n_eff+((M/2).*dn.*y); % time varying effective index for ring
beta_t = 2.*pi.*n_t_eff./wl;

% Ring Transfer Function
c_t = sqrt(1-k);
z_t = exp((i.*beta_t.*L));
gamma_t = 10^(-1.*loss./20);
H_t = (c_t-gamma_t.*(z_t.^-1))./(1-c_t.*gamma_t.*(z_t.^-1));
H_t_amp = 10*log(abs(H_t).^2);
H_t_phase = angle(H_t);
H_t_phase_unwrap = unwrap(angle(H_t))./pi;

% Plot Response
figure(3)
subplot(3,1,1)                  % magnitude, one FSR
set(gca,'FontSize',14)
plot(t./1e-9,H_t_amp,'-b','LineWidth',2)
xlabel('Time [nS]')
ylabel('Amplitude')
title(sprintf('Ring Chirp: \\kappa = %0.2f, \\alphaL = %0.1f dB, Phase
Mod = %0.1e Hz',k,loss,mod_freq),'FontSize',16,'FontWeight','demi')
grid on

subplot(3,1,2)                  % unwrapped phase, one FSR
set(gca,'FontSize',14)
plot(t./1e-9,H_t_phase_unwrap,'-b','LineWidth',2)
ylabel('Phase [rad /\pi]')
maxy = max(H_t_phase_unwrap);
miny = min(H_t_phase_unwrap);
ylim([miny-0.5 maxy+0.5])
grid on

% Instantaneous Frequency
ChirpPeriod = H_t_phase_unwrap.*pi;
chirp = diff(ChirpPeriod)./1e-9;

subplot(3,1,3)
set(gca,'FontSize',14)
plot(t(1:length(t)-1)./1e-9,chirp./1e6,'-b','LineWidth',2)
xlabel('Time [nS]')
ylabel('Inst. Freq. [MHz]')
grid on

% Plot Chirp
figure(4)
set(gca,'FontSize',14)
plot(t(1:length(t)-1)./1e-9,chirp./1e6,'-b','LineWidth',3)
```

```
%plot(t(1:length(t)-1)./1e-9,chirp./max(chirp),'-b','LineWidth',3)
%normalized
hold on
xlim([10 15])
xlabel('Time [nS]')
ylabel('Inst. Freq. [MHz]')
%ylabel('Normalized Frequency')
title(sprintf('Ring Chirp\n\\kappa = %0.2f, \\alphaL = %0.1f dB, Phase
Mod = %0.1e Hz',k,loss,mod_freq),'FontSize',16,'FontWeight','demi')
grid on
```

VITA

William Timothy Snider received his Bachelor of Science degree in electrical engineering from Texas A&M University – College Station in 2008. He then continued at Texas A&M for graduate school and graduated in August 2012 with his Ph.D. degree. His research interests include device fabrication and optical sensors and systems. He has accepted a technical staff position at Sandia National Laboratories.

Mr. Snider may be reached by email at wtsnider@gmail.com or at Texas A&M University, Department of Electrical and Computer Engineering, C/O Dr. Christi Madsen, 214 Zachry Engineering Center, TAMU 3128, College Station, TX, 77843-3128.